

# University of Southampton Research Repository

Copyright © and Moral Rights for this thesis and, where applicable, any accompanying data are retained by the author and/or other copyright owners. A copy can be downloaded for personal non-commercial research or study, without prior permission or charge. This thesis and the accompanying data cannot be reproduced or quoted extensively from without first obtaining permission in writing from the copyright holder/s. The content of the thesis and accompanying research data (where applicable) must not be changed in any way or sold commercially in any format or medium without the formal permission of the copyright holder/s.

When referring to this thesis and any accompanying data, full bibliographic details must be given, e.g.

Thesis: Author (Year of Submission) "Full thesis title", University of Southampton, name of the University Faculty or School or Department, PhD Thesis, pagination.

Data: Author (Year) Title. URI [dataset]

### University of Southampton

Faculty of Physics School of Physics and Astronomy

# Single-Photon-Level Atomic Frequency Comb Quantum Memory in Warm Rubidium Vapour

by

**Zakary Schofield** 

**MPhys** 

ORCiD: 0009-0006-9527-0450

A thesis for the degree of Doctor of Philosophy

June 2025

#### University of Southampton

#### **Abstract**

Faculty of Physics School of Physics and Astronomy

Doctor of Philosophy

### Single-Photon-Level Atomic Frequency Comb Quantum Memory in Warm Rubidium Vapour

by Zakary Schofield

Quantum memories are devices that allow for the on-demand storage and retrieval of photonic quantum information. They are crucial devices in the realisation of quantum communication networks and are also used for synchronising qubit inputs for photonic quantum computers. This thesis reviews the current state of the field of quantum memories, including an assessment of the current platforms and protocols used before critiquing the current state-of-the-art research within the quantum memory community. The main research undertaken for this thesis revolves around the Atomic Frequency Comb (AFC) memory protocol within warm Rubidium 87 vapour. The thesis then explores the theory behind this protocol, describes how this protocol is implemented experimentally, and presents the results, which demonstrate the storage of short pulses of light with high intensity and also at the single-photon level. The limits of the AFC protocol are also investigated. The limits include (a) the dependence of the protocol on different pumping preparation regimes, (b) the optical depth of the atoms, and (c) the single photon limit. The compatibility of this memory with polarisation and time-bin qubits is also demonstrated, providing the groundworks for this quantum memory to store true single-photon qubits.

This thesis lays the groundwork for integrating this protocol with a quantum dot single-photon source to allow for fidelity measurements.

# **Contents**

Li	st of	Figures	i	ix
D	eclara	ition of	Authorship	xi
A	cknov	wledge	ments	xiii
D	efinit	ions an	d Abbreviations	xvii
1	Intr	oductio	on	1
	1.1	Quant	tum Technologies	. 1
		1.1.1	Quantum Networks	. 2
		1.1.2	Quantum Metrology	4
		1.1.3	Quantum Computers	. 5
		1.1.4	Photonic Qubits	. 7
			1.1.4.1 Time-bin	. 7
			1.1.4.2 Frequency	. 7
			1.1.4.3 Polarisation	. 8
		1.1.5	Single Photon Sources	. 9
			1.1.5.1 Spontaneous Parametric Down Conversion	. 10
			1.1.5.2 Silicon Nitride Ring Resonators	. 12
			1.1.5.3 Quantum Dot	12
	1.2	Quant	tum Memory	14
		1.2.1	Applications	14
	1.3	Figure	es of merit	15
		1.3.1	Efficiency	15
		1.3.2	Storage time	16
		1.3.3	Bandwidth	16
		1.3.4	Noise and fidelity	16
		1.3.5	Wavelength	17
		1.3.6	Multi modality	. 17
		1.3.7	Scalability	18
	1.4	Platfo	rms for quantum memories	18
		1.4.1	Rare-Earth Ion-Doped Solids	18
		1.4.2	Warm vapours	. 19
	1.5	Optica	ally controlled memories	19
	1.6	Re-ph	asing memories	22
	1.7	Summ	nary	23
	1 Q	Thoric	Outlook	23

vi CONTENTS

2	Ato	mic Fred	quency Comb Memory	25
	2.1	Introdu	uction	25
			Bloch sphere representation	27
	2.2		ted efficiency	27
			Storage Time Derivation	30
			Theoretical Efficiency Plots	31
	2.3		f the art	32
	2.4		sion	35
3	War	m Vano	ur Implementations of AFC	37
	3.1	_	rgy levels	37
	3.2		mental details	39
	0.2	-	Reference cell	43
			Fabry-Perot interferometer	43
			Pulse creation	44
				45
			Beam Mode	
			Telescope	47
	2.2		Transmission efficiency	48
	3.3		y selective pumping	48
			Velocity selective optical pumping theory	49
			VSP experimental results	50
			Power broadening	50
	3.4		ations of VSP	54
			Introduction	55
			Experimental setup	56
		3.4.3	Results	57
		3.4.4	Conclusion	58
	3.5	Summa	ary	58
4			ur AFC Experiment	61
	4.1	CW Re	esults	61
		4.1.1	Temperature dependence	64
			4.1.1.1 Temperature dependence results	66
		4.1.2	Detuning dependence	66
		4.1.3	Pump-back power dependence	70
	4.2	Pulsed	AFC	71
			Pump sequencing	74
			Pulsed results	74
			AFC diffusion lifetime	75
	4.3	Summa	ary	78
5	War	m Vapo	ur AFC: Single-Photon Level Experiments	81
_	5.1	_	photon AFC measurements	82
	٠.1		Signal to Noise ratio	84
	5.2		Vidth Characterisation	85
	5.3		photon number characterisation	88
	5.4		g Storage Time	89
	<b>∵. T</b>	A OUT A THE	G CHOINGE IIIIE	00

*CONTENTS* vii

	5.5 5.6	AFC in F = 1 ground state	95 96
6	War	m Vapour AFC: Qubit Compatibility Experiments	99
	6.1	Polarisation Dependence	99
		6.1.1 Experimental setup	100
		6.1.2 Results	101
	6.2	Temporal Multi-modality	102
		6.2.1 Results	103
	6.3	Summary	105
7	Con	clusions	107
	7.1	Summary	107
	7.2	Continuation of research	108
Αŗ	pend	lix A AppendixA	109
	App	endix A.1 Hybrid Quantum Networks Lab	109
		Appendix A.1.1 Founding of HQNL	109
		Appendix A.1.2 COVID-19	110
		Appendix A.1.3 Moving to the Opto-Electronics Research Centre	112
	App	endix A.2 One Laser AFC	112
		Appendix A.2.1 New Experimental Setup	112
		Appendix A.2.2 Results	114
		Appendix A.2.3 Summary	115
	App	endix A.3 Publications and contributions	115
		Appendix A.3.1 Publications	115
		Appendix A.3.1.1 Future publications	116
		Appendix A.3.2 Conference contributions	116
Re	feren	ices	117

# **List of Figures**

1.1	Quantum Repeater	3
1.2	Unbalanced Mach-Zehnder Interferometer	8
1.3	Linear and Circular polarisation	9
1.4	Poincaré sphere	10
1.5	Spontaneous Parametric Down Conversion	11
1.6	Spontaneous four-wave mixing energy level diagram	12
1.7	Quantum dot emission process	13
1.8	3 level atomic configurations	20
1.9	Dressed EIT states	20
2.1	Bloch Sphere of AFC protocol	28
2.2	AFC Criteria with labelled parameters	29
2.3	AFC Efficiency Simulations	33
3.1	Energy level diagram for AFC in <sup>87</sup> Rb with labelled AFC preparation and input signal lasers	39
3.2	Cross section of Rb cell with laser modes	40
3.3	Complete Experimental Setup	40
3.4	Saturation absorption spectroscopy of natural abundance Rb	44
3.5	Varying EOM Widths	45
3.6	EOM saturation	46
3.7	Beam Modes of the different lasers used in the experiment	47
3.8	VSP Sequencing	48
3.9	VSP with labelled transitions	51
3.10	vsp power broadening demonstration	52
	Pump-back power dependence	53
	VSP Dephasing Time	54
	Illustration of the ORCA storage and retrieval process	55
	Telecom ORCA level diagram and experimental setup	57
3.15	ORCA Results	57
4.1	Simplified CW Experimental Diagram	62
4.2	CW AFC Spectrum	63
4.3	CW AFC Storage	64
4.4	Cell heating voltage dependence	67
4.5	Atom Number Temperature vs Total Efficiency	68
4.6	AFC memory comparison of different signal detuning	69
4.7	Efficiency vs detuning for cw AFC	70

x LIST OF FIGURES

4.8	Pump-back Power Dependence
4.9	Pulsed AFC Experimental Diagram
4.10	AOM Response time
	Pulsed regime pumping order
	Efficiency vs detuning for pulsed AFC
	Diffusion lifetime
4.14	Diffusion lifetime - read-in efficiency
5.1	Single photon level output AFC Experimental Setup
5.2	Single-photon level AFC demonstration
5.3	SNR calculation regions
5.4	Pulse Width Investigation
5.5	Comparison of different input pulse widths
5.6	PPG width vs recall pulse width
5.7	Single Photon Limit Investigation
5.8	Comparison of different $\mu$
5.9	AFC structures for different pump-back laser modulation 93
5.10	Storage Time vs Total Efficiency
	AFC spectrum in $F = 1$ ground state
5.12	AFC storage in $F = 1$ ground state
6.1	Simplified experimental setup for polarisation dependence 101
6.2	Polarisation state vs total Efficiency
6.3	Multi-modality demonstration
	endix A.1 Lab 2020, Dated October 2020
	endix A.2 Lab 2024, Dated October 2024
	endix A.3 Frequency modulation for one laser AFC
App	endix A.4 RF mixing setup
App	endix A.5 One laser vs two laser AFC spectra comparison 114
App	endix A.6 One laser AFC storage

### **Declaration of Authorship**

I declare that this thesis and the work presented in it is my own and has been generated by me as the result of my own original research.

#### I confirm that:

- 1. This work was done wholly or mainly while in candidature for a research degree at this University;
- 2. Where any part of this thesis has previously been submitted for a degree or any other qualification at this University or any other institution, this has been clearly stated;
- 3. Where I have consulted the published work of others, this is always clearly attributed;
- 4. Where I have quoted from the work of others, the source is always given. With the exception of such quotations, this thesis is entirely my own work;
- 5. I have acknowledged all main sources of help;
- 6. Where the thesis is based on work done by myself jointly with others, I have made clear exactly what was done by others and what I have contributed myself;
- 7. Parts of this work have been published as: S.E. Thomas, S. Sagona-Stophel, Z. Schofield, I.A. Walmsley, and P.M. Ledingham. Single-photon-compatible telecommunications-band quantum memory in a hot atomic gas. *Phys. Rev. Appl.*, 19:L031005, Mar 2023

Signed:	Date:

# Acknowledgements

Completing this PhD has been one of the hardest tasks of my life, it has claimed my sanity and almost claimed my enjoyment of the subject. I would not have made it this far without the help from a strong group of family, friends and colleagues.

I had the pleasure of being a part of the Hybrid Quantum Networks Lab research group, all of whom I owe this thesis to. Firstly, my supervisor Patrick, your continued support and faith in my abilities is what has led me this far and I greatly appreciate all the help and advice that you have given me over the years. Next is Ori who has always been there whenever I have had troubles with the experiment or with my own self-confidence, our friendship means a lot to me and I look forward to many more years of it. Also many thanks to Vanderli who has always greeted me with a smile on his face and tons of enthusiasm for my many experiments, you have taught me how to proud of the work that I do. And finally Nick, thanks for all the times that you have helped to de-stress me either over a pint or a conversation about our shared taste in fantasy literature (journey before destination!) I wish you all the best of luck with your academic careers and I hope we will see lots of each other in the future.

Next I wish to thank the various housemates that I had while living in Southampton; Owen, Daniel, Hugo and Matt. You guys made every horrible day much more bearable and every fun day even better! I will miss the times we would drink and play games in our living room. All those DnD sessions really helped me escape my sometimes overwhelming reality, long live the Iron Cru. Thank you to Lakksan who was always there to gass me up whenever I was doubting myself. And to my close friends Michael and Niamh, thanks for always hosting me in Edinburgh, my bi-yearly trips always gave me something to look forward to and I will continue to look forward to all of my future trips.

I also owe a lot to Southampton University Canoe Club (SUCC) for providing me with a lot of much needed weekend and evening de-stressing, especially Jacob, Jack, Fil and Ted for always be there for me when I needed you most - a quick mention of my PhD support group (The League of Tiberious) while we only met a couple of times you have been incredibly useful. I can't mention crucial weekends without acknowledging Matthew, thank you for all those weekends spent playing Smash, drinking and

cooking amazing food in BOA or Bath. You have always been available for me whenever I needed you most and I will never forget that.

I owe lots of thanks to my wonderful girlfriend Lydia, your unwavering faith in me has been my rock through the final year of my PhD and I wouldn't have finished writing my thesis without you.

And finally my family, thanks to my sister Eleanore for being a fantastic role model and always being there when I need you, my twin Louis who always checked on me and who is always there when I need distractions. And finally my parents, your complete faith in my abilities and eternal support for which ever direction I chose to take my life is what has gotten me this far. I owe this accomplishment to you.

To the ones that matter.

# **Definitions and Abbreviations**

AFC Atomic Frequency Comb

AOM Acoustic Optical Modulator

APD Avalanche Photodiode

ATS Aulter-Townes Splitting

AWG Arbitrary Waveform Generator

BSM Bell State Measurement

CRIB Controlled Reversible Inhomogeneous Broadening

Cs Caesium

CW Continous Wave

DBR Distributed Bragg Reflector DFB Distributed Feedback Diode

DM Dichroic Mirror

EIT Electromagnetically Induced Transparency

EOM Electro-Optic Modulator

F Finesse

FLAME Fast Ladder Memory
GEM Gradient Echo Memory

HWP Half Wave Plate

HQNL Hybrid Quantum Networks Lab

ICL Imperial College London

LIGO Laser Interferometer Gravitational-Wave Observatory

ND Neutral Density Filter

OD Optical Depth

ORCA Off-Resonant Cascaded Absorption

PBS Polarising Beam Splitter QC Quantum Computing

QD Quantum Dot

QKD Quantum Key Distribution

QM Quantum Memory QWP Quarter Wave Plate

Rb Rudibium

REIDS Rare-Earth Ion-Doped Solids

RF Radio Frequency
SNR Signal to Noise Ratio
SPD Single Photon Detector

SPDC Spontaneous Parametric Down Conversion UMZI Unbalanced Mach-Zehnder Interferometer

USA United States of AmericaVSP Velocity Selective Pumping

 $\Gamma$  AFC Bandwidth  $\gamma$  AFC Tooth Width  $\Delta$  AFC Tooth separation

 $\delta$  Detuning  $\eta$  Efficiency  $\lambda$  Wavelength  $\lambda/2$  Half-Wave Plate  $\lambda/4$  Quarter-Wave Plate

 $\mu$  Average Photon Number  $\rho$  Density Matrix

au Storage Time  $\psi$  Wavefunction  $\omega$  Frequency  $|e\rangle$  Excited State

 $|g\rangle$  Ground State  $|s\rangle$  Storage State

 $\hbar$  Planck's constant /  $2\pi$ 

# Chapter 1

## Introduction

### 1.1 Quantum Technologies

The aim of quantum technologies is to utilise quantum mechanical resources, such as entanglement and superposition, to outperform their current state-of-the-art classical counterparts. These resources are: (1) superposition, where a quantum system is described as a complex linear combination of basis states, and (2) entanglement, where a composite system (comprising of two or more subsystems) exhibits strong non-classical correlations such that the overall quantum state cannot be decomposed into the independent states of the parts, even when these subsystems are spatially separated. While still in development, these technologies will revolutionise the fields of computing [2] and telecommunications [3]. Quantum technologies are seeking to develop the fields of: simulation [4], sensing [5], secure communication [6], drug development [7], supply chain optimisation [8], cryptography (Shor's algorithm [9]) and metrology [10] and beyond. These technologies have practical applications in defence (secure communication, accelerometers on nuclear submarines), advanced computing (quantum computing) and, quantum internet protocols.

Quantum technologies are a significant avenue for academic and industrial research, requiring billions of pounds of investment. In 2023, the UK government announced its National Quantum Strategy, where it committed to investing £2.5 billion over the next ten years [11].

In this chapter, I will outline key quantum technologies that currently are, or could be, enhanced through the use of quantum memories.

#### 1.1.1 Quantum Networks

Quantum networks - based on the principle of sending information encoded on single photons - allow entanglement distribution over considerable distances, facilitating cloud quantum computing and secure quantum communication via schemes like Quantum Key Distribution (QKD).

QKD is a secure communication method via quantum networks. This method works by communicating an encrypted message classically between two parties, Alice and Bob, but they send the decryption key via a quantum channel. This scheme (the BB84 protocol) was first proposed by Charles H. Bennett and Gilles Brassard in 1984 [12].

Alice choses a random basis to prepare entangled photons, by choosing one of two polarisers: Horizontal  $(\rightarrow)$  / Vertical  $(\uparrow)$  and Diagonal  $(\nearrow)$  / Anti-diagonal  $(\nwarrow)$ . Bob then randomly sets his polariser to measure either the  $\rightarrow/\uparrow$  or to measure  $\nearrow/\nwarrow$ resulting in a correct basis measurement 50% of the time. After the transmission, Alice and Bob will compare notes; if their settings are incompatible, they discard the corresponding measurements and keep the relevant data, with the remaining measurement used for error correction. The photons with matching measured basis states will be used for the key to decipher the classical message. If there is an eavesdropper (Eve), they will not know Bob's random settings and will match basis states half of the time. Once Eve measures the photon on their particular basis, Eve will then produce a photon in a given basis state determined by this outcome. Therefore, when Alice and Bob compare their results, there will be more errors (25% of the time their basis states will match compared to 50% from before, informing them of the presence of Eve. Needless to say, the ability to know without question if your information has been "eavesdropped" would be of invaluable use in the fields of government, business, or espionage.

Quantum mechanics follows the no-cloning theorem [13], which states that an arbitrary quantum state cannot be copied. Therefore, when building quantum networks, one cannot use optical amplifiers to boost the likelihood of a single-photon qubit propagating through a quantum network with a significant loss as the amplified signal will not possess the quantum properties of the initial photon. Classical long-distance telecommunications are reliant on the ability to amplify the signal to reach its destination, and therefore quantum telecommunications must instead look for different solutions to this challenge.

A solution to this challenge is to use a quantum repeater [14] to overcome the loss associated with using optical fibres to transmit encoded photons at long distances (Fig 1.1). The use of repeaters means that the total transmission distance is broken into shorter links such that the loss per link is lower than the risk of loss across the total span of transmission distance.

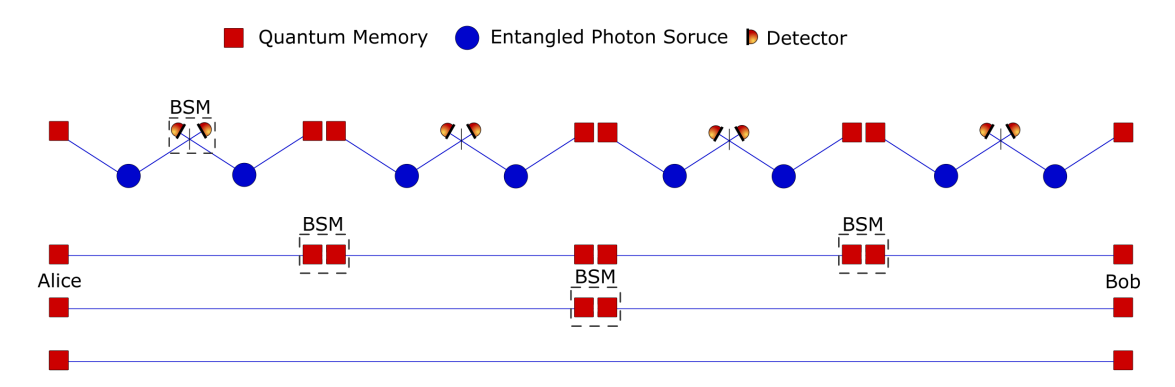


FIGURE 1.1: Quantum Repeater protocol allowing for entanglement swapping between Alice and Bob via a series of bell states measurements (BSM) and single photon detectors (SPD)

The quantum repeater is based on entanglement generation and the subsequent swapping of pairs of entangled photons. Entangled photon pair sources are placed along the network along with quantum memories so that one photon from the source goes into a memory and the other to a Bell State Measurement (BSM); comprised of a 50:50 beamsplitter with two single-photon detectors (SPD). Two entangled photon sources (blue dots in Fig 1.1) placed between two quantum memories will each randomly produce a pair of photons, one will go into a memory (red squares) and the other will go to an SPD. Entanglement is created when only one of the sources emits a photon, but it is unknown which produced it. As the detection of a photon heralds the entanglement, if the SPDs measure zero or two photons the process is repeated until a reading of one is given. Extending this process over the entire network will allow Alice and Bob to be entangled. A key ingredient in this process are the quantum memories, which allow for the entangled photons to be stored while a neighbouring pair is created. To realise a quantum network without memories will require the entanglement swapping and generation to be successful simultaneously, which is a highly improbable case. This process swaps the entanglement network to Alice and Bob.

This can be done in fibre [15] or in free space [16]; and has even been proposed via satellites [17]. Unlike the fibre-based protocol, the primary loss of the satellite quantum repeater protocol is through the absorption or the scattering of the photons as they travel through the atmosphere; while the satellites are in space, they need to communicate with the ground at some point, hence the loss via the atmosphere, there is also loss by diffraction of light changing the path of entangled photons.

A recent paper [18] has proposed the idea of using large-scale vacuum tubes to transport single photons qubits across the United States of America (USA); this idea originates from the vacuum tubes used in the Laser Interferometer Gravitational-Wave Observatory (LIGO) experiment for detecting gravitational waves [19]. This method reduces a network's loss due to fibre propagation and replaces it

with lenses with orders of magnitude lower loss for the 1550nm telecom wavelength. This is a theoretical proposition, as building a network of this scale would require a large financial investment and the experimental challenge of maintaining a vacuum over hundreds of kilometres.

The largest experimental demonstration of a quantum network by the number of nodes is by QuTech and Kavli Institute of Nanoscience [20] in 2021 and another network with memories was also demonstrated in 2024 [21] with 3 links separated by around 10km.

#### 1.1.2 Quantum Metrology

Metrology is the study of measurement and its application. Using Quantum Mechanical principles, one can improve the sensitivity and accuracy of measurements [22]. Quantum Metrology has applications in Biology, Sensing, and Gravitational wave detection. It is used in biology and chemistry to measure the dynamics and structure of photon-sensitive biological molecules [23]. Squeezed states are quantum states described by two non-commuting observables (e.g. phase and amplitude) where ones uncertainty is reduced below the standard quantum limit at the cost of increased uncertainty in its conjugate variable, due to the Heisenberg uncertainty principle [24]. When applying a squeezed state to biological samples, the squeezed light is fed into an interferometer which probes a sample in one of the arms of the interferometer. Phase-squeezed states reduce the noise in the phase quadrature, enhancing the interferometer's ability to detect small phase shifts of the sample caused by changes in the refractive index or molecular binding [25]. This improves the singal-to-noise ratio of these measurements beyond classical capabilities. Additionally, using these quantum photonic states reduces the effect of photodamage and photobleaching on these senstive biological samples.

Quantum Metrology sensors for gravitational wave detection work off the principle of interference, where a 50/50 beam splitter splits a laser and travels down to orthogonal paths to be reflected through the beam splitter towards a photodiode; this is more commonly known as a Michelson Interferometer [26]. Suppose a gravitational wave passes through the interferometer. In this case, the path length of one of the orthogonal paths is changed, causing destructive interference between the reflected paths on the photodiode and reducing the optical power detected. A gravitational wave of frequency  $\omega$  can be inferred as a power modulation with the same frequency [27]. This led to the Nobel Prize in Physics in 2017 for the research carried out by the LIGO/VIRGO Collaboration for the first detection of gravitational waves.

Quantum metrology is an avenue of quantum applications that is of interest in the military, as quantum metrology allows for a long, coherent source of geolocation. It

has a use in nuclear submarines [28] using quantum accelerometers (QA). These devices measure the trajectory of atoms within a vacuum with respect to a reference mirror [29]; with sensitivities between from 1 - 10 ng (where  $g = 9.81ms^{-1}$ ) over an 11-hour integration time [30]. This offers a unique solution for nuclear submarines, as they have to resurface to re-calibrate their GPS. Still, a submarine equipped with QAs can remain underwater for much longer, keeping them from being observed via satellites. These devices have been demonstrated to work but are not currently being used on active military submarines.

#### 1.1.3 Quantum Computers

Classical computers rely on bits, which are inputs of either 1 or 0, and execute code sequentially. Quantum computers use qubits instead of bits to perform their calculations, but unlike bits, qubits can exist in a superposition of two states (1 and 0), each with a different probability amplitude. Particular algorithms are applied where qubits can be choreographed in such a way that the paths leading to the wrong answer destructively interfere and the paths leading to the right answer constructively interfere [31].

Many researchers within the quantum computing field aim to build a "Universal Quantum Computer", combining a classical computer with a quantum computer that can simulate advanced physics and quantum mechanics. To fully realise a quantum computer, it must meet the following criteria (as proposed by IBMs Di Vincenzo [32]):

- 1) Well-characterized and scalable qubits known physical parameters, good coupling with other qubits and easy manipulation of the qubit states.
- 2) Qubit initialisation the ability to create a qubit set must be straightforward and well-understood.
- 3) Long decoherence times—The qubit's decoherence times must be longer than the gate operation time.
- 4) A "universal" set of quantum gates—to perform arbitrary operations on a qubit, single and two-qubit gates are required.
- 5) Qubit-specific measurement capability—The ability to measure individual qubits is needed to determine the result of a computation.

Quantum computers can be built on various platforms, such as trapped ions, neutral atoms, superconductors, and photons [33]. Trapped ion QCs use charged atoms (ions) as qubits whose qubit states are defined by the energy levels of the ions. These are trapped using linear ion traps to secure the atoms in a stationary 3D location; as they

are suspended in space, they are relatively immune to environmental noise, allowing for high-fidelity performance. The main issue with trapped ions is scalability; as longer chains of ions are made, reading out a specific ion with high accuracy becomes more challenging because the laser precision needed exceeds current laser technologies. Also, larger ion chains have shorter coherence times, limiting the size of a trapped ion QC [34]. Companies such as IonQ [35] are committed to building a trapped ion QC with large qubit numbers.

Neutral atom QCs are based on a large number of trapped atoms (commonly Rb Rydberg atoms) with a neutral charge. Rydberg atoms are excited atoms with a high principle quantum number n; leading to significant electric dipole moments that can facilitate strong interactions with weak electromagnetic fields [36]. Lasers are used to create qubit states within these atoms as several excited states can be used as the  $|0\rangle$  or  $|1\rangle$  levels for a qubit. Optical tweezers suppress the movement of these atoms, cooling them down to near absolute zero. At these low temperatures, the energy levels used for qubit operations are easy to resolve, and the lack of momentum in these atoms leads to long coherence times (nearly 1 second [37]). Companies such as QuEra [38] are currently investing in neutral atom QCs.

A popular platform (and arguably the most famous) for QC is superconducting qubits. Much like an atomic qubit, the superconducting qubit needs to have two distant states ( $|0\rangle$  and  $|1\rangle$ ), and are predominately one of three different qubit archetypes, according to the different degrees of freedom; charge qubits, flux qubits, and phase qubits [39]. These qubit platforms have the advantage of being easy to control as they rely on commercial microwave devices with a high level of design-ability. However, to implement this platform dilution refrigerators are required to remove the thermal background of the photons at the relevant qubit frequencies. Currently these technologies are not capable of storing the requisite number of qubits for a full fault-tolerant quantum computer, alternatively, microwave to optical conversion can be used to interconnect and entangle multiple dilution fridges.

In 2019, Google announced they had reached quantum supremacy with their Sycamore computer consisting of 53 qubits [40], and more recently with their 105 qubit device [41]. Other companies pursuing superconducting QCs include IBM [42], Intel [43], IMEC [44] to name a few, it is clear that this is an avenue for QCs with a sizeable financial investment.

Photonic QCs use photons as qubits and linear optical elements to perform quantum operations. Photonic QCs fit the Di Vincenzo [32] criteria reasonably well, but as single photons don't interact with each other, two-qubit gates are challenging. The other issue with these QCs is that photons tend to scatter or get absorbed in optical components, compromising computational circuits [45]. Two-qubit gates are implemented using the interference between two different optical paths to form a

CNOT gate within QCs. These computers are built with linear optics; such as beam splitters, phase shifters and photo-detectors. Companies such as ORCA Computing [46] and PsiQuantum [47] are working towards building a full-stack photonic QC.

#### 1.1.4 Photonic Qubits

Photons make ideal candidates for qubits due to their robustness to decoherence at ambient temperatures, high capacity for encoding information, and non-interaction with each other [48]. Therefore, a large number of photons can be used for quantum operations. As classical communication techniques like the Internet are based on light, an extensive framework exists for incorporating photonic qubits into existing infrastructure [49].

Encoding techniques include time-bin, frequency and polarization. This thesis discusses these methods and describes their implementations.

#### 1.1.4.1 Time-bin

A time-bin encoded qubit can be created using an Unbalanced Mach-Zehnder Interferometer (UMZI) [50]; this interferometer consists of two paths of different lengths created using 50/50 beam splitters to split and recombine these paths as can be seen in Fig 1.2. An input photon is, therefore, equally likely to take the short path and arrive early ( $|E\rangle$ ) or the long path and arrive late ( $|L\rangle$ ). This creates a photon that has a superposition of Early and Late paths, represented by the normalised wave function in Eq 1.1 [51], where  $\phi$  is the phase created by taking this longer path, this allows interference measurements to be performed.

$$|\psi\rangle = \frac{1}{\sqrt{2}}(|E\rangle + e^{i\phi}|L\rangle)$$
 (1.1)

The requirement for this generation is for the time difference between the two potential paths of the UMZI to be greater than the temporal length of the photon [52].

Time-bin qubits have been proposed to be used in quantum communications protocols such as the BB84 quantum key distribution protocol [53] and for distributed quantum computing [54].

#### 1.1.4.2 Frequency

Like time-bin qubit encoding, one can encode a qubit state that is a superposition between two different single-photon states of different frequencies. One approach to

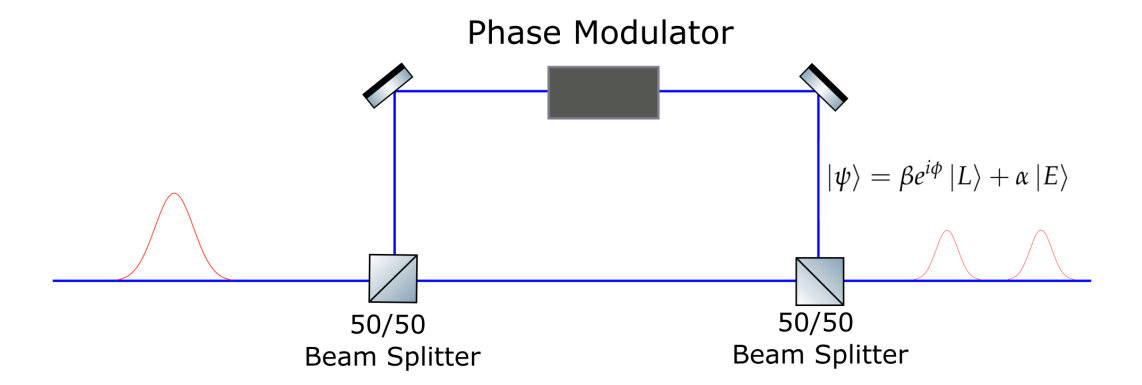


FIGURE 1.2: Unbalanced Mach-Zehnder Interferometer for producing time-bin qubits with single photons. A photon enters on the left and can take one of two paths of different lengths to create a time-bin qubit exiting on the right. The phase modulator creates a  $\phi$  on the Late path to perform interference measurements between the paths.

creating this frequency qubit is to use a frequency beam splitter to split input light into one of two frequency modes of equal probability - an example based on a four-wave mixing process in a photonic crystal can be found in [55]. Another approach uses Electro-Optic modulation and Fourier-transform pulse shaping to create frequency-bin qubits across the entire c-band [56]. This implementation functions as a frequency domain analogue of the Hadamard gate, which transforms a qubit from a definite basis state into an equal superposition of basis states. To perform this Hadamard operation, a numerically optimised phase pattern is applied via a pulse shaper which effectively splits the input photon coherently into two frequency bins with equal amplitude probability. This method does not rely on spatial/polarisation modes to encode the qubit and achieves near-unitary fidelity, with a reported value of  $F = 0.99998 \pm 0.00003$ .

#### 1.1.4.3 Polarisation

A superposition between two polarisation states creates polarisation encoding. These can be linear polarisations (horizontal/vertical or diagonal or anti-diagonal) or circular polarisations (left-hand or right-hand). Fig 1.3 shows how the electric field propagates for these cases. An example of a normalised wavefunction for a qubit polarised in the Horizontal and Vertical plane is represented by the following:

$$|\Psi\rangle = \frac{1}{\sqrt{2}}(|H\rangle + |V\rangle)$$
 (1.2)

In this case, the two different polarisation states are Horizontal ( $|H\rangle$ ) and Vertical ( $|V\rangle$ ) polarisation. The allowed polarisation states can be represented on a Poincaré sphere, Fig 1.4, a method for visualising polarisation states to calculate polarising

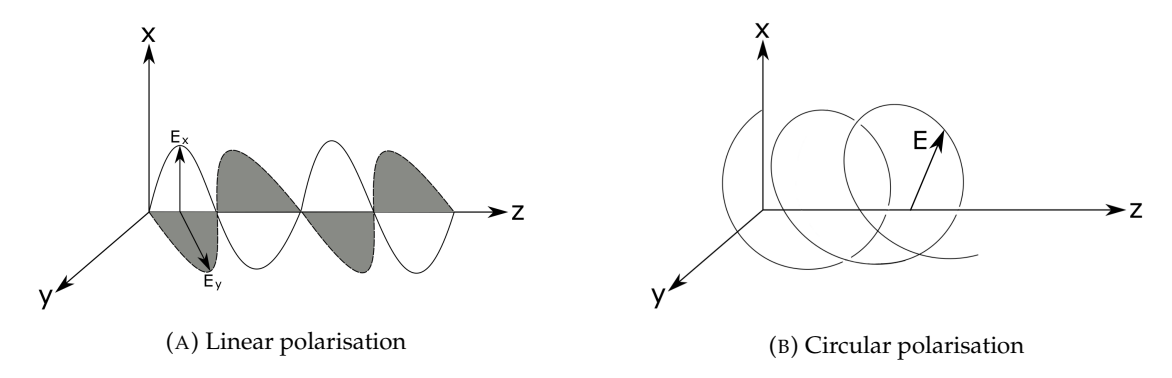


FIGURE 1.3: Linear and Circular polarisation. Linear polarisation: the electric field vector is confined to one plane along the direction of propagation. Circular polarisation: the electric field vector rotates in the plane normal to the direction of propagation.

components' effects. The points of the equator correspond to linear polarisations of light (Horizontal -  $|H\rangle$ , Vertical -  $|V\rangle$  and Diagonal -  $|D\rangle$ , Anti-diagonal -  $|A\rangle$ ) and the poles represent circular polarisations of light (Left-hand -  $|L\rangle$ , Right-hand  $|R\rangle$ ).  $S_1, S_2, S_3$  are the stokes parameters, of the polarisation state which correspond to the states Cartesian coordinates. Where  $S_1 = cos(2\epsilon)cos(2\alpha)$ ,  $S_2 = cos(2\epsilon)sin(2\alpha)$  and  $S_3 = sin(2\epsilon)$ , where  $\alpha$  is the azimuthal angle (green circle (Fig 1.4)) ranging from  $\pm \pi/2$  and  $\epsilon$  is the elliptical angle (blue circle) ranging from  $\pm \pi/4$ . A radius of 1 corresponds to the sphere's surface and is for completely polarised light. Orthogonal polarisation states are opposite on the Poincaré sphere.

#### 1.1.5 Single Photon Sources

To use photons as qubits, one first needs a true single-photon source, which produces an individual photon per emission cycle. This can be represented by the second-order autocorrelation function  $g^{(2)}(\tau)$  [57], which is a comparison of the intensity of light at different times. This is defined by Eq 1.3, where n is the number of counts at a given detector i (where i = 1,2), t is the time when the first detection occurs on one of the detectors and  $\tau$  is the detection time on the other one. The numerator represents the probability of detecting counts in both detectors simultaneously and the denominator is the product of the average counts of each detector.

$$g^{(2)}(\tau) = \frac{\langle n_1(t)n_2(t+\tau)\rangle}{\langle n_1(t)\rangle\langle n_2(t+\tau)\rangle}$$
(1.3)

This measurement is performed experimentally with a 50/50 beam splitter and two single-photon detectors. If the source is a true single-photon source, the detectors won't register a single photon simultaneously. Therefore, the second-order autocorrelation function at a time delay  $\tau = 0$  should be equal to zero ( $g^{(2)}(0) = 0$ ), with maximum values when  $\tau = m\tau_r$  where m are integer values and  $\tau_r$  is the repetition rate of the single-photon source.

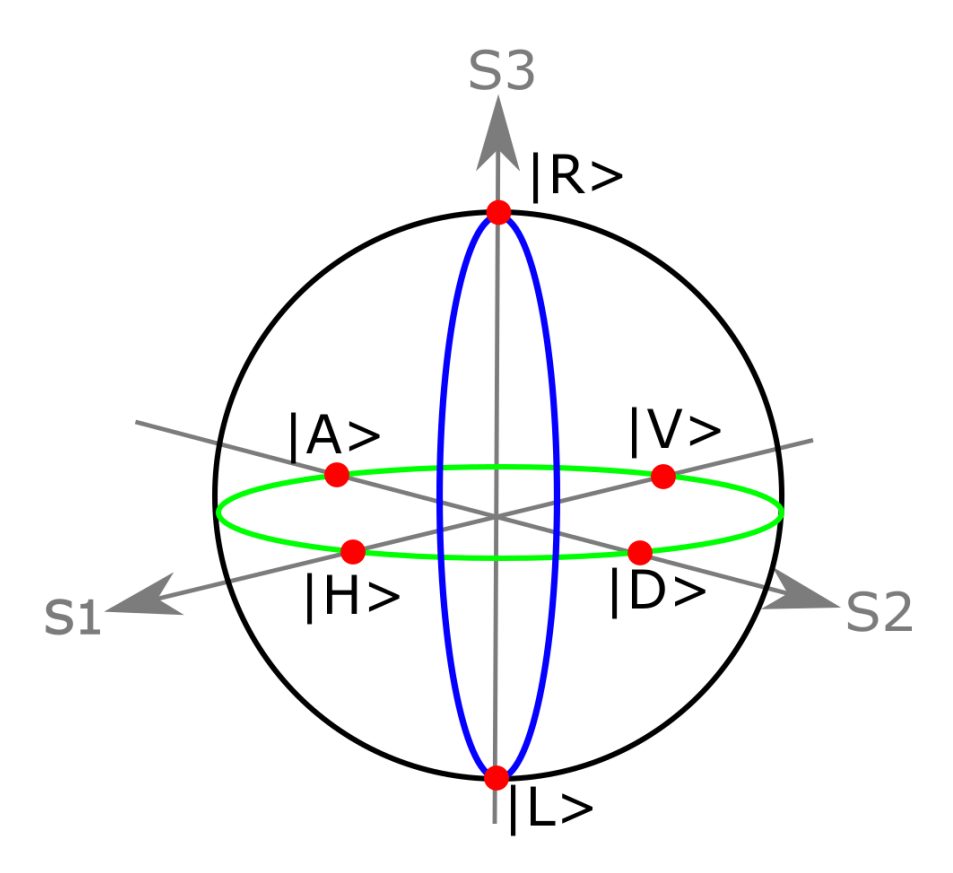


FIGURE 1.4: Poincaré sphere with labelled orthogonal polarisation states and the stoke parameter axes. Where  $|H\rangle$  - Horizontal,  $|V\rangle$ - Vertical,  $|D\rangle$  - Diagonal,  $|A\rangle$  - Antidiagonal,  $|L\rangle$  - Left-hand and  $|R\rangle$ - Right-hand polarisation.

There are many methods of single photon production, each with its own advantages and disadvantages, which, when discussed, demonstrate that no model can consistently produce true single photons.

#### 1.1.5.1 Spontaneous Parametric Down Conversion

Spontaneous Parametric Down Conversion (SPDC) generates a pair of photons from one photon, this can be both degenerate (two photons of the same wavelength [58]) or non-degenerate (two photons of the different wavelengths [59]). It is a non-linear optical process where a photon is split into two other photons of lower energy, whose total energy is equal to the initial photon;  $\hbar\omega_p = \hbar\omega_s + \hbar\omega_i$ , where  $\omega_p$  is the frequency of the pump photon,  $\omega_s$  and  $\omega_i$  are the frequency of the signal and idler photons respectively (see Fig. 1.5a). The momentum of these photons is also conserved (see Fig. 1.5b), making capturing this signal and idler photon simple.

The output state of the SPDC pair is a two-mode squeezed vacuum:

$$|\Psi\rangle_{SI} = \sqrt{1 - \lambda^2} \sum_{n=0}^{\infty} \lambda^n |n\rangle_S |n\rangle_I$$
 (1.4)

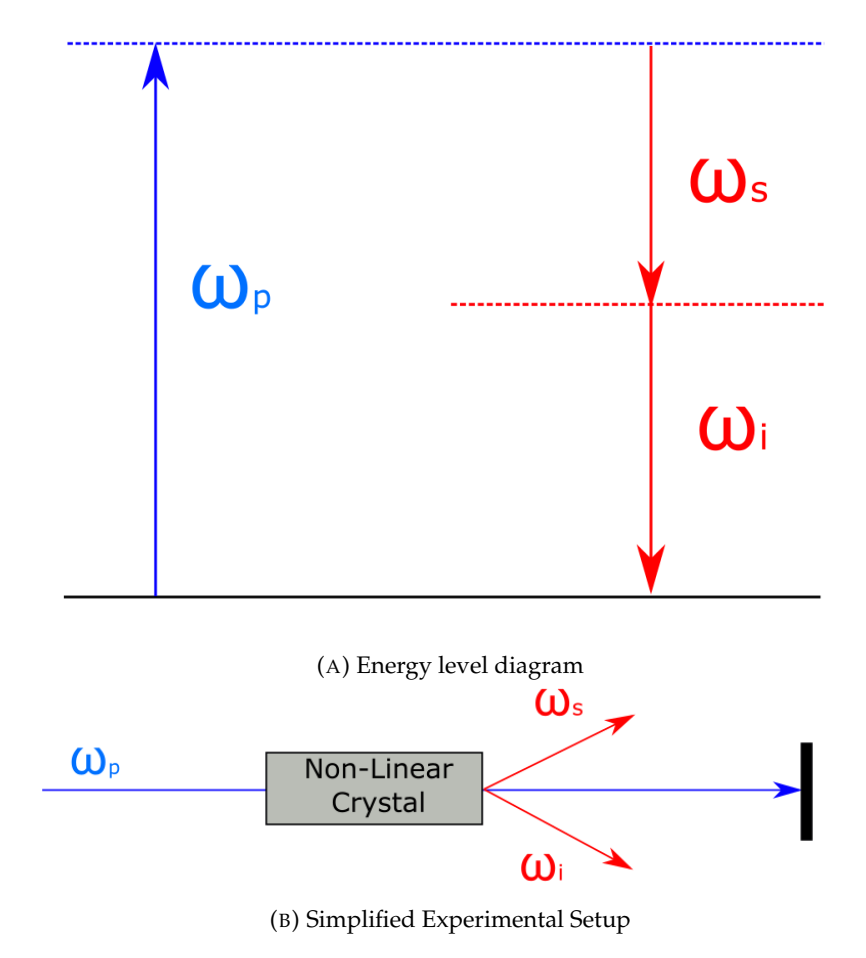


FIGURE 1.5: Spontaneous Parametric Down Conversion. (A) is the energy level diagram for the scheme: a pump photon  $(\omega_p)$  converts into a pair of photons with lower energy  $(\omega_i$  - signal and  $\omega_i$  - idler)

where  $|n\rangle_{S/I}$  is an n-photon Fock state in the Signal/Idler mode, respectively, and  $\lambda$  is the squeezing parameter determined by the non-linear crystal and pump power properties. To increase the production rate of the single photon pairs, one can increase the power of the pump laser, therefore increasing  $\lambda$ ; this also increases the probability of a multi-photon Fock state generation, which increases the  $g^{(2)}(0)$  of the source.

SPDC was first theorised by W. H. Louisell et al. [60] in 1961 and demonstrated experimentally by David C. Burnham and Donald L. Weinberg a few years later [61]. SPDC is commonly achieved with periodically-poled Lithium Niobate (PPLN) [62] and in  $\beta$ -Barium Borate (BBO) [63] crystals. The advantage of this source is that it can be constructed and operated at room temperature but achieving a low  $g^{(2)}(0)$  can be a challenge.

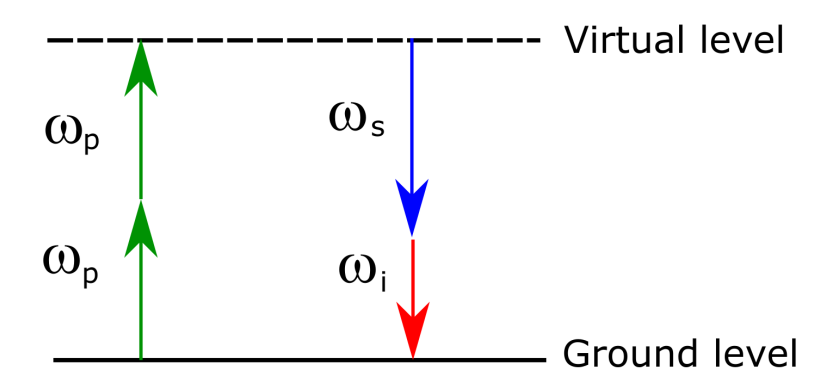


FIGURE 1.6: Spontaneous four-wave mixing energy level diagram. Two pump photons  $(\omega_p)$  create a pair of signal  $(\omega_s)$  and idler  $(\omega_I)$  photons of different frequencies.

#### 1.1.5.2 Silicon Nitride Ring Resonators

Silicon Nitride (SiN) Ring Resonators produce a photon pair based on spontaneous four-wave mixing (SFWM) implemented in an integrated micro-ring resonator in the silicon nitride platform. SFWM is a third-order ( $\chi^{(3)}$ ) nonlinear process in which two photons from a pump field with frequency  $\omega_p$  are annihilated to produce a pair of correlated photons with different frequencies; these are referred to as the signal ( $\omega_s$ ) and idler ( $\omega_i$ ). i.e.  $2\omega_p = \omega_s + \omega_i$  [64]. The SiN platform for implementing SFWM is due to its low intrinsic linear loss and a favourable refractive index for good optical confinement. This platform has demonstrated a high quality of conditional self-correlation  $g_H^{(2)} = 0.008 \pm 0.003$  with a wavelength of 1550nm [65].

This device has also been demonstrated with a wavelength resonant with the <sup>87</sup>Rb D2 transition with a wavelength of 780nm [66]. It can also be used as a source of a frequency comb generation [67], or as a sensing element for an optical gyroscope [68].

#### 1.1.5.3 Quantum Dot

Quantum dots (QD) are formed within semiconductor nano-crystals usually grown epitaxially; two crystals with a mismatch of lattice constant are grown on top of one another, leading to a small structure (roughly 10s of nm [69]) that confines electrons in 3 dimensions forming a semiconductor bandgap such that there are discrete solutions to the Hamiltonian of the system. This results in what is referred to as an 'artificial atom' [70]. This bandgap is made of a lower energy valence band (acting as the ground state of the artificial atom) and a higher energy conduction band (excited state), the initial state can be seen in Fig 1.7a, where the electrons are all in the valence band with associated holes in the conduction band. An excitation laser which is not resonant with the bandgap ( $E_{gap}$ ) can excite the electron to the conduction band; this is

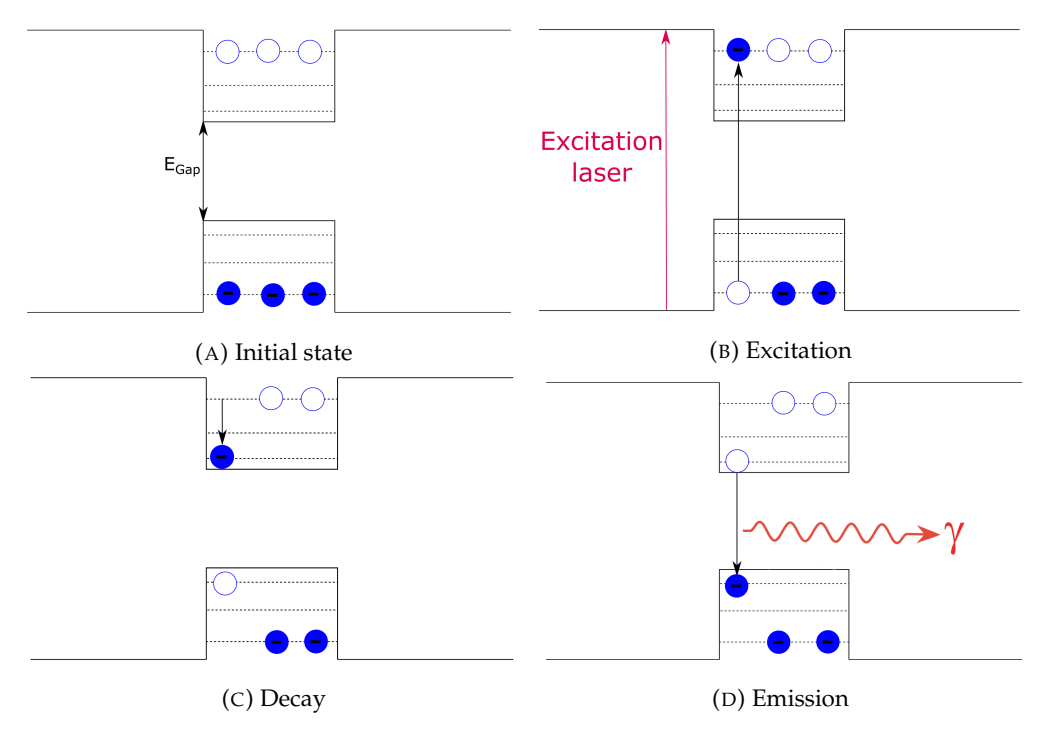


FIGURE 1.7: Quantum dot emission process. (A) is the initial state where all the electrons are in the valence band, (B) an off-resonant excitation laser excites an electron the conduction band leaving an associated hole in the valence band, (C) the electron undergoes phononic decay to a lower energy level of the conduction band, (D) the electron undergoes radiative decay back to the valence band, this emits a photon with wavelength equal to  $E_{gap}$ .

referred to as above-band excitation [71], which leaves a hole in the valence band (Fig. 1.7b). This electron then undergoes phononic decay (a phonon is a vibrational quasiparticle within the crystal [72]) to the lower energy level of the conduction band (Fig 1.7c). This electron then undergoes radiative decay back down to the valence band, which results in a photon being emitted with a wavelength equal to the energy bandgap between the valence and conduction bands. Fig 1.7 shows the entire process described previously; note that the direction of growth of these semiconductor crystals is along the x-axis of this figure, meaning that the emitted photon direction is perpendicular to the plane of the sample. As the wavelength emitted depends on the energy bandgap of the quantum dot, which depends on how the lattice is grown, there is a large variation of potential wavelengths within a quantum dot sample. Therefore, growing identical samples or samples with a precise emission wavelength (for example, one resonant with an atomic transition of a different atom) can be challenging. A seed laser can also be resonant with the band gap of the QDs, meaning that no phononic decay needs to occur before the photon is emitted, but exciting the sample off-resonantly means that wavelength-dependent optics can be used to separate the seed from the emitted photon, making the capture of this photon easier. QDs operate at cryogenic temperatures ranging from 3 - 10 K, as ambient temperatures lead to many vibrations within the crystal that can de-cohere the

sample. The most widely used QD sample uses an Indium Gallium Arsenide (InGaAs) with a Gallium Arsenide (GaAs) layer grown on top [73]; with the mismatch of their lattice constant forming the QDs. There are serval criteria by which the quality of a QD can be determined: purity, indistinguishability, and brightness [74]. Purity means that a true single photon is emitted from the QD, i.e. the  $g^{(2)}(0)$  is close to zero; indistinguishability means that all the photons emitted from the QD have the same wavelength and polarisation - they are identical to each other. Finally, brightness corresponds to the probability of emitting a photon from a given excitation pulse. A recent paper from the University of Science and Technology of China (USTC) has demonstrated a QD with a wavelength of 884.5nm, a  $g^{(2)}(0) = 0.0205$ , purity of 98% and an efficiency of 71.2% which is the first time this source has surpassed the efficiency threshold for scalable photonic quantum computing [75]. QDs have also been used to distribute QKD across a 18km fibre in the Copenhagen metropolitan area [76], this source has a wavelength of 942nm and is frequency converted to 1545nm to transmit through the fibre with low loss, the  $g^{(2)}(0) = 0.47 \pm 0.14\%$ . Overall, QDs are a leading platform for deterministic single-photon generation, which offers a strong single photon source with a range of emission wavelengths, but with an engineering challenge associated with achieving a specific wavelength and the requirement for cryogenic cooling. It was for these benefits that QDs were chosen within our research group, as well as the requirement for cryogenics being met by another experiment.

### 1.2 Quantum Memory

Photonic quantum memories allow for the on-demand storage and retrieval of photonic-based quantum information while preserving the quantum state. They are crucial components in long-distance quantum communication and the synchronisation of optical quantum computers. The ability to store these qubits efficiently and with experimental simplicity is the overall goal of the research carried out within this thesis, as this will allow for optical quantum technologies to be fully realised and constructed, potentially within existing optical infrastructure.

#### 1.2.1 Applications

As mentioned, quantum memories are used to build quantum repeaters, which are crucial to constructing quantum networks. These allow the storage of photons while Bell-state measurements take place to distribute entanglement across a network of large distances. As optical fibres have an associated loss (around 0.15dB/km at 1550nm, which is the low loss c-band of industry standard optical fibres) and a single photon qubit cannot be cloned due to the no-cloning theorem, quantum memories need to be placed along the network to extend the distance that one can distribute a

pair of entangled photons over. The storage time of these quantum memories needs to be greater than the repetition rate of the single photon source and the travel time between a source and the photon detector used for Bell-state measurements (see Fig 1.1).

As stated previously, single-photon sources and qubit encoders can be inefficient or indeterministic; quantum memories are therefore required to synchronise photonic inputs for these quantum computers. If a QC has N photonic input qubits, the waiting time for all of these inputs to produce a photon simultaneously increases exponentially with N. For example, suppose one has N number of heralded single-photon sources and N number of associated quantum memories. In this case, detecting an idler photon will determine the presence of a signal photon within the memory. The quantum computing algorithm can begin once all N memories have stored a photon. Synchronising 12 photon inputs with a photon source rate of 1GHz, and a heralding efficiency of 50%, it would require nearly 30 years to produce a photon simultaneously. If one introduces memories (with an efficiency  $\eta = 75\%$ ) to store a produced photon until all the memories have a photon within them, for a 12-photon source input, this can reduce the wait time to roughly  $100\mu$ s. These calculations were performed by J. Nunn in 2013 [77]. While these assumptions are generous for the real-world implementation of this technique, they still justify the use of quantum memories as synchronisation devices for photonic QC. The bandwidth of these memories needs to match the bandwidth of the single-photon sources used.

### 1.3 Figures of merit

Some criteria judge the performance of a quantum memory, and the requirements for these criteria vary significantly between applications. For example, long storage time is required for quantum repeaters and shorter storage times are sufficient for local storage (QCs). All of these factors discussed have their associated experimental challenges.

A summary of these criteria is as follows:

#### 1.3.1 Efficiency

Efficiency ( $\eta$ ) measures how well a memory stores and retrieves the inputted photon, defined as the input-to-output energy ratio. A high end-to-end experimental efficiency is required to realise a memory protocol fully. The end-to-end efficiency is the combination of the memory efficiency and the transmission efficiency of all the optics within the path of the stored light. The aim is to have as high efficiency as possible.

The efficiency can be calculated with the equation:

$$\eta = \frac{\langle N_{out} \rangle}{\langle N_{in} \rangle} \tag{1.5}$$

Where  $< N_{in} >$  and  $< N_{out} >$  are the average photon number per pulse for the input and output, respectively.

#### 1.3.2 Storage time

The storage time of a memory is how long the memory can hold a photon before it is retrieved or lost, for example, it can be realised from the atoms due to spontaneous emission [78] at an unknown time for the operator of the memory. The required storage time for a given protocol depends on the application of the memory protocol. For example, when using memories for quantum networks, the storage time needs to be long enough to communicate along the length of the network classically. The transmission time through a network is roughly  $5\mu$ s per 1km [79]. For the synchronisation of qubits, the maximum storage time required must be longer than the reciprocal of the repetition rate of the single-photon source; once a photon is heralded inside a memory, it can be stored for as long as it takes for all inputs to the QC to have a photon within them. Fundamentally, the lower limit of the storage time has to be greater than the temporal length of the input photon for the memory to store the photon completely.

#### 1.3.3 Bandwidth

The bandwidth of a QM is defined by the maximum photon bandwidth that the memory can store [80]. Bandwidth matching to a single-photon source is also an important consideration. For example, SPDC sources produce photons with broader bandwidths (THz) than semiconductor quantum dots (GHz). The storage time ideally exceeds the inverse of the input photon bandwidth.

#### 1.3.4 Noise and fidelity

A priority when building a quantum memory is achieving a high signal-to-noise ratio. Sources of noise depend on the type of memory protocol being used. High noise can come from four-wave mixing [81], spontaneous emission [82], inefficient pumping, or leakage of control lasers. Methods of reducing noise include storing in an excited atomic state as these states don't contain atoms inherently; therefore, recalling a stored photon from an excited state will not emit unwanted photons. Unfortunately, this

limits the protocol's storage time to less than the excited state lifetime. Another method of reducing noise is to separate the wavelength of the pump lasers used, this allows for wavelength-dependent filtering - using optics like dichroic mirrors or interference filters. This approach is dependent on the memory protocol and the platform used, as some of these use transitions with close wavelengths. In the case of a protocol where the signal and control are close in wavelength, narrowband cavities are required for enhancement. Such approaches can be used to suppress four-wave mixing [83], as well as inbuilt quantum interference within memories that suppress noise [84].

Fidelity is a measure of how well a quantum state retains its encoded information while being stored inside a memory The fidelity between an input state  $\rho_{in}$  and an output state  $\rho_{out}$  is defined as:

$$F(\rho_{in}, \rho_{out}) = \left(tr\sqrt{\sqrt{\rho_{in}}\rho_{out}\sqrt{\rho_{in}}}\right)^2$$
(1.6)

where  $\rho_{in}$  and  $\rho_{out}$  are the density matrices for the input and output states, respectively [85]. Ideally, one wants a fidelity of F = 1 for any input state, but the classical limit of F > 2/3 needs to be reached when using single photon inputs [86]. The fidelity needs to be greater than the fault-tolerant quantum error correction threshold [87].

#### 1.3.5 Wavelength

A memory's wavelength must be compatible with current quantum and optical technologies. Suppose a memory is used for a quantum network. In that case, it must be capable of storing photons whose wavelength lies within the low-loss telecommunications c-band regime (1530nm—1565nm) [88] to ensure efficient fibre propagation through the network. In contrast, one also requires the memory to be resonant with single-photon sources.

#### 1.3.6 Multi modality

An ideal quantum memory can store multiple input modes at once. These can be temporal modes [89], frequency modes [90], or spatial modes [91]. The more modes a memory can store, the higher its scalability factor and, therefore, the wider the range of applications it can use. If one memory can store N modes, then a quantum repeater protocol can be multiplexed, achieving an N-fold increase in the overall success probability [92]. Different protocols and platforms have a range of multimodal capabilities and limitations on the number of modes that can be stored; these limitations will be discussed in their relevant sections of this chapter.

#### 1.3.7 Scalability

Most of the applications discussed previously require many memories to realise fully; therefore, the memory that one builds must be reproducible and consistent when many are built [93]. For example, platforms constructed with cryogenics may be expensive and experimentally challenging; therefore, integrated or room-temperature devices are favourable, whereas free space systems are susceptible to spatial and frequency drift due to changes in the environment where the experiment is performed. For example, fluctuations in the room temperature of an optics lab can change the thermal properties of a laser source and, therefore, the laser's frequency. Room temperature changes can also change the alignment of room temperature optics. These factors can degrade the performance of a quantum memory over long periods of time.

#### 1.4 Platforms for quantum memories

Quantum memories can be constructed on various platforms. The ones I will discuss in this section are Rare-Earth Ion-Doped solids (REIDs) and warm vapours. The platform affects the experimental complexity of implementing the protocol and can change the effectiveness of some of the criteria discussed previously. The subsections will provide more detail on the common platforms used and discuss the benefits and drawbacks of each protocol. This will justify the platform used in the research covered in this thesis.

#### 1.4.1 Rare-Earth Ion-Doped Solids

Rare-earth ion-doped solids (REIDS) are crystals doped with Rare Earth ions with favourable optical properties - long-lived optical and spin coherences, such as transitions resonant with telecom lasers. As REIDS are a solid-state platform, there is no memory decoherence due to atomic collisions, meaning achieving long storage times becomes easier. REIDS have a partially filled 4f electron shell that is shielded from the environment by the outer filed 5s shell, which gives rise to narrow spectral lines within the 4f-4f transitions. Carefully selecting a host crystal helps to reduce the host interaction within the REIDS. REIDS are used at cryogenic temperatures of around a few Kelvin or in the sub-Kelvin regime, achieved using cryostats and dilution refrigerators; the expense of which adds another layer of experimental difficulty. They must be at this temperature to remove the phononic interaction within the crystal. Phonons are quasiparticles based on vibrations within lattices [94].

#### 1.4.2 Warm vapours

Warm atomic vapours allow for a more significant number of atoms at ambient temperatures. The standard approach to realising this platform is to use vapour cells, which are glass cells that contain vapours of specific atomic elements or molecules [95].

Gas cells can also contain a buffer gas; causing the atoms to move slower and, therefore, stay in the pump lasers for longer. The pumping ease is due to the atoms colliding several million times per second (this rate depends on the pressure of the buffer gas and the specific gas used), thereby changing the Doppler shift. Eventually, an atom will become resonant with the pump laser. This means that a narrow band pump laser can optically pump a broad spectrum of atoms, removing the reliance on power broadening of the pump laser.

Collisions with the cell walls change the ground state of the atoms. To prevent this a paraffin coating is used to reduce the relaxation rate of the atoms [96]. This allows lower optical powers to pump the entire population from a given ground state entirely, and the atoms remain in their pumped ground state for much longer.

Memories can also be built within optical fibres; where an atomic vapour placed inside the fibre to facilitate the storage and retrieval of light. Using fibres can allow for a high interaction between light and atoms within the fibres as there will always be good overlap between the atoms and the light. The main issues with using optical fibres as a platform are the high loss within fibres over more considerable distances.

The first demonstration of a QM in a hollow core optical fibre was by . F. M. Champion et al. [97]; a Raman memory of warm Cs vapour inside the fibre with a total memory efficiency of 27% with a significant signal to noise ratio of 2.6:1. While this protocol requires 200 times less pulse power than a free-space equivalent protocol the lifetime (1/e) of this memory is limited to  $27\pm9$ ns which is the time it takes the Cs atoms to move across the core of the fibre and stick to the walls.

Due to these features of QMs in hollow core fibres it was not used for this thesis, therefore the platform that is used in this was the <sup>87</sup>Rb gas cells without a buffer gas, this was because it is relatively cheap and easy to implement within free space.

# 1.5 Optically controlled memories

These are memories in which optical fields interact with the atoms to facilitate the storage and recall of light. Optically controlled usually utilises a 3-level atomic system. We are interested in three different configurations: ladder, lambda, and Vee

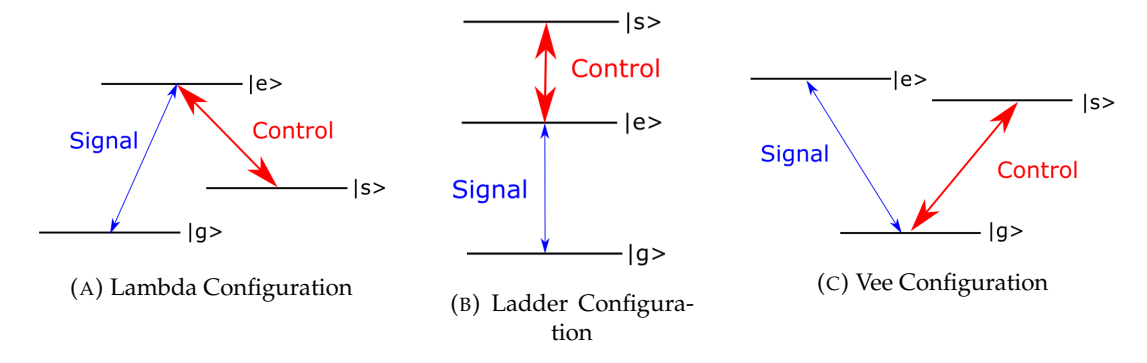


FIGURE 1.8: 3 level atomic configurations with labelled Signal and Control lasers, where;  $|g\rangle$  is the ground state,  $|e\rangle$  is the excited state and  $|s\rangle$  is the storage state.

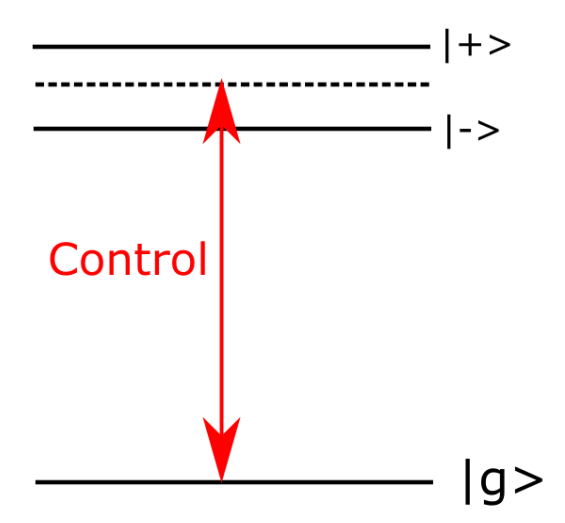


FIGURE 1.9: Dressed EIT states,  $|g\rangle$  is the ground state, the dotted line is the excited state, which has been split into a  $|-\rangle$  and  $|+\rangle$  dressed state by a control laser.

[98]. Diagrams of these configurations can be seen in Fig 1.8, where  $|g\rangle$  is the ground state,  $|e\rangle$  is the excited state, and  $|s\rangle$  is the storage state. The interaction with these levels is achieved with light fields, labelled signal and control that interact with  $|g\rangle$  -  $|e\rangle$  and  $|s\rangle$  -  $|e\rangle$  transitions, respectively.

One of the most commonly utilised optical protocols is Electromagnetic Induced Transparency (EIT); this protocol uses an intense control beam resonant with the  $|s\rangle$  -  $|e\rangle$  transition and a weak probe beam to store our photonic state. It can be performed in any configuration in Fig 1.8. The control beam modifies the light-matter interaction Hamiltonian to dress the bare state  $|e\rangle$  into two dressed states  $|+\rangle$  and  $|-\rangle$  where  $|\pm\rangle=\frac{1}{\sqrt{2}}(|e\rangle\pm|s\rangle)$ . These states are equidistant from the original state  $|e\rangle$  at zero detuning from this state  $(\Delta=0)$  creating the transparency window. These newly dressed states  $|+\rangle$  and  $|-\rangle$  are the eigenstates of this new light-matter interaction Hamiltonian created by the dressing of the control beam. This new dressed system can be seen in Fig 1.9.

The control's Rabi frequency gives this transparency window width and can result in transmission windows that are much narrower than the atom's natural line width. The bandwidth of the encoded photon needs to be within the width of the transparency window so that it is not absorbed. Also, the control pulse that is used to dress the system modifies the light-matter Hamiltonian of the ensemble. This leads to a change in the refractive index of the medium, resulting in a reduced group velocity proportional to the control field - this is known as slow light [99]. The input photons bandwidth must be such that the photon is entirely compressed inside the medium, ramping down the control beam maps the photon into the atomic coherence state. To retrieve this photon, one turns on the control field again to trigger the reverse of this process.

EIT has been demonstrated in cold Cs atoms with an efficiency of 92% [100] with coherent pulses containing roughly 30,000 photons, and in laser-cooled <sup>87</sup>Rb atoms with a storage time of 1.2 $\mu$ s with an efficiency of 7.5% using an attenuated input pulse with a FWHM of 1.5  $\mu$ s [101]. It has also been reported at high efficiencies (78%) in cold atomic mediums [102] and demonstrated with a storage time of up to 1 minute in a Praseodymium doped Yttrium Orthosilicate ( $Pr^3: Y_2SiO_5$ ) crystal [103]. Both of these were done with attenuated coherent pulses and not true single-photons.

EIT is commonly used in protocols favouring long storage times and high efficiencies over the other figures of merit discussed in this chapter. EIT has also been demonstrated as a multi-purpose quantum memory [104] with 1,000 qubit manipulations to perform quantum stack, queue and buffer operations. These are quantum demonstrations of classical computing and signal processing. This memory array consists of 72 spatially separated EIT memories based in  $144^{87}$ Rb atomic ensembles; this protocol has a variable storage time of up to  $500\mu$ s with a 95% fidelity measured using time-bin qubits.

An extension of the EIT process is Autler-Townes Splitting (ATS). ATS happens in the strong-coupling limit of EIT [102], where the strong electromagnetic field can split a transition into a doublet due to the AC stark effect. This was first proposed by Autler and Townes [105]. This memory works by directly absorbing into the dressed  $|-\rangle$  and  $|+\rangle$  states, as these are excited states there is a chance that the photon will undergo spontaneous emission, ultimately limiting the efficiency of the protocol. ATS also experiences a transparency effect but with a much wider transparency window. This means the signal photon does not require a narrow bandwidth, as seen in EIT, making ATS more applicable to broadband operation. ATS also has much better scaling efficiency with optical depth than EIT as the storage mechanism of ATS relies on absorption, therefore, a larger OD ensures that the input pulse fully interacts with the medium before it exits.

The ATS memory protocol has been demonstrated in laser-cooled Rubidium with a storage time of 200ns and an efficiency of 12.5% [106]; other refinements of the ATS protocol has been shown with efficiencies of 23% in cooled Rb ensembles [107].

The Raman memory, first proposed in 2000, is based on a Lambda configuration (Fig 1.8a) where  $|g\rangle$  and  $|s\rangle$  are two long-lived ground states with the entire atomic population in the  $|g\rangle$  state. The signal laser is detuned by  $\Delta$  from the  $|g\rangle - |e\rangle$  transition; therefore, without a control field, the signal propagates through the atoms without absorption. A strong control pulse creates a two-photon transition from  $|g\rangle - |s\rangle$ , creating a spin wave atomic coherence between these two levels. A second control pulse is applied to reverse the process and retrieve this signal. Due to the long-lived storage state, this protocol can store signal pulses for a long time. This protocol's bandwidth is determined by the bandwidth of the control pulse, meaning it can store photons with a bandwidth greater than 1GHz. This protocol has been demonstrated in warm <sup>87</sup>Rb vapour with an efficiency of 87%, and an unconditional fidelity of 98% [108].

Schemes based on the ladder configuration (Fig 1.8b) offer the advantage of having a storage state empty of atoms before the memory protocol is implemented. This allows these protocols to be inherently noise-free. Two protocols based on this idea are the fast-ladder memory (Flame) and the Off-Resonant Cascaded Absorption (ORCA); both of these protocols use a strong control field with a weak signal field to excite an atom to a doubly excited storage state. These two protocols differ because ORCA is far detuned from the intermediate excited state ( $|e\rangle$ ). In contrast, FLAME can be resonant or slightly detuned from this state. The FLAME memory has been demonstrated in Rubidium vapour with an external efficiency of 25%, a 1/e lifetime of 86ns, and  $10^{-4}$  noise photons with an average photon number signal of 0.5 [109]. The ORCA protocol will be discussed in more detail in Chapter 3.

# 1.6 Re-phasing memories

Re-phasing memories, sometimes referred to as photon-echo memories, are protocols based within ensembles of two-level atoms where the transitions have been inhomogeneously broadened. This can arise from different velocity classes in a warm vapour broadening a given transition via the Doppler effect or from local strain in solid-state platforms. External magnetic or electric fields can also facilitate this broadening. As there is a spread of frequencies in these atom ensembles, once a pulse of light is absorbed by this ensemble, creating an atomic coherence phase, it will be accumulated at different rates, leading to dephasing. One can control the rephasing of these coherences to retrieve the signal from this ensemble in a photon echo.

Controlled Reversible Inhomogeneous Broadening (CRIB) quantum memory and extension of the Gradient Echo Memory (GEM), first proposed by N. Sangouard in 2007 [110], is based on the work done in [111] where it was shown that the efficient photon echos could be produced when exploiting the fact that the Doppler shift changes sign if the propagation direction of the light is reversed. This is done by using an external magnetic field to artificially broaden a transition by the Zeeman shift. Once a signal has been absorbed, the broadening causes the atoms to accumulate phase. Reversing the direction of the magnetic field rephases all the atoms to retrieve the signal. The rephase time is the same as when the atoms were allowed to dephase. This has been demonstrated in a cold  $^{87}$ Rb ensemble with a total efficiency of  $80 \pm 2\%$  with a coherence time of  $195\mu s$  [112]

Another protocol, the Atomic Frequency Comb protocol, shapes the inhomogeneously broadened ensemble into a series of equally spaced frequency combs. This protocol is the focus of this thesis, so it will be described in detail in the next chapter.

#### 1.7 Summary

This chapter clarifies that quantum technologies have a place in the future of technological development. They offer unique solutions to several problems and potential problems that current technologies cannot overcome.

While Quantum Memories are a small part of the larger quantum technology landscape, they have many potential applications. They are sometimes necessary to operate certain quantum technologies (such as quantum networks and photonic quantum computers).

The Quantum Memory community is vast, and many avenues of research are being carried out worldwide. This thesis already states that QMs can be made on various platforms, each with its uses, issues, and limitations. The large number of protocols means that the quantum memories used throughout the global QM community vary.

#### 1.8 Thesis Outlook

The outline of the thesis will now be discussed; this is to give the reader a view of the structure of the rest of this thesis and the context of these chapters. This thesis is split into seven chapters, not including the Appendix chapters, with the chapters containing the following topics:

**Chapter 1: Introduction**: This is the current chapter of this thesis. It includes a general literature review to provide the wider context of the thesis. It provides information

about the larger picture of the research, the potential applications of the thesis' work, and the gap in the research this project fills.

Chapter 2: Atomic Frequency Comb Memory. This chapter introduces the protocol used throughout the rest of this thesis; the theory behind the protocol will be discussed along with some simulations and derivations. Finally, the 'state of the art' of the protocol discusses the work completed by other people within the quantum memory community on this protocol.

Chapter 3: Warm Vapour Implementations of AFC. This chapter described applying the AFC protocol to the warm vapour platform. There are several issues with using a warm vapour platform, and this chapter addresses them (using the velocity selective pumping (VSP) technique). Finally, this chapter demonstrates another memory protocol called the ORCA memory and how VSP can be used to improve it; this experiment was carried out in collaboration with Imperial College London (ICL), based on some of the same experimental protocols as the AFC protocol in this thesis.

**Chapter 4: Warm Vapour AFC Experiment.** This chapter contains most of the experiments on the AFC protocol, mainly characterisations of the memory with high-power short pulses of light for storage. This chapter also compares the two pumping preparation regimes - cw and pulsed.

Chapter 5: Warm Vapour AFC: Single-Photon Level Experiments. This chapter is a continuation of the characterisation of the AFC protocol, but this time with single-photon level inputs; operating at the single-photon level allows for a more in-depth understanding of how the memory operates while proving that the protocol is compatible with single-photon level inputs, this is a key step in fully realising this protocol for larger quantum applications.

Chapter 6: Warm Vapour AFC: Qubit Compatibility Experiments. This chapter builds off the previous chapter using single-photon level input to test if the memory can store encoded photons without destroying the encoded information (maintaining fidelity). Two types of qubit compatibilities are tested, polarisation qubits and time-bin qubits, and they are shown to work in the warm vapour AFC protocol.

**Chapter 7: Conclusions.** This chapter revisits the initial goals of the thesis and how effective the experiments were at completing these goals. This chapter also discusses the future of this project and the potential directions a future researcher can take the protocol.

# **Chapter 2**

# **Atomic Frequency Comb Memory**

#### 2.1 Introduction

The Atomic Frequency Comb (AFC) protocol is a photon echo memory based on the spectral shaping of an inhomogeneously broadened transition into a frequency comb with periodic spacing  $\Delta$ [89]. Typically, this protocol is implemented within REIDS due to the spectral hole capability within the crystal field inhomogeneously broadened transitions. In warm vapours, the initial inhomogeneously broadened transition arises from Doppler broadening due to the atoms moving around within the vapour cell. This is a Maxwell-Boltzmann distribution of velocities and, therefore, frequencies. For a room temperature Rubidium ensemble, this width tends to be 500 - 700MHz, depending on the temperature of the ensemble.

A photon with bandwidth less than the total width of the frequency comb can be absorbed into a collective excitation represented by the wave function:

$$|\psi\rangle = \frac{1}{\sqrt{N}} \sum_{j}^{N} e^{i\delta_{j}t} |g_{1}, g_{2}, ..., e_{j}, ..., g_{N-1}, g_{N}\rangle$$
 (2.1)

where N is the number of atoms in the ensemble,  $\delta_j$  is the detuning of a given atom, and  $|g\rangle$ ,  $|e\rangle$  are ground and excited states respectively, at a time t for a given atom j. The wave function is the coherent sum of all the atoms within the ensemble, where one of the atoms absorbs an input photon. Each atom has a phase term once the light is absorbed  $(e^{i\delta_j t})$ . Once the ensemble is shaped into the AFC structure made of sharp peaks, this detuning is approximated by  $\delta_j \approx m_j \Delta$  where  $m_j$  are integers, and the total number of these is the number of AFC peaks M.

At t = 0, the terms in the sum are in phase and, therefore, collective. Given the periodic nature of the AFC structure, the collective state rapidly dephases. At a time t =  $2\pi/\Delta$ ,

the collective atomic state rephases, and the light is remitted in the forward direction. Due to the large number of atoms in the ensemble, this process's efficiency is limited to 54%. If the input light is efficiently stored at the start of the ensemble, then the echo light will also get absorbed before the ensemble's end.

Due to the nature of the AFC protocol, there are inherent multimodal capabilities [113]. For example, one can store photons of different frequencies resonant with different points in the comb as long as each input is resonant with a few AFC teeth. Another method is to create multiple AFCs on different parts of the inhomogeneously broadened line [114]. As the AFC is commonly built of atomic transitions for a warm vapour platform, the optical depth of the AFC teeth is proportional to the strength of the transitions, meaning that achieving an AFC with teeth of equal height can prove challenging.

As the AFC is a photon-echo/rephasing protocol, each photon stored creates its own collective excited state; therefore, multiple photons with different arrival times can be stored within the memory. This memory can thus be used to store time-bin qubits (see Chapter 1 for information on time-bin qubits).

The final multimodal capability of this protocol depends more on the protocol used. The lasers used to create the AFC have a cross-sectional area, meaning multiple spatially distinct regions can be used within the memory. This is useful when using warm vapour platforms over REIDS as the crystals used in REIDS are much smaller (around 4x4mm [115]) compared to vapour cells, which commonly have a diameter on the order of several centimetres [116]. These features give a high potential number of modes that can be stored and recalled efficiently within this memory.

A popular method for extending the storage time of this protocol is to use a strong magnetic field to lift the degeneracy of the ground states so that the collective excitation can be stored into one of these states (labelled as  $|s\rangle$ ) using pumping selection rules - this is referred to as spin-wave storage. This storage is facilitated with a  $\pi$ -pulse resonant with  $|e\rangle - |s\rangle$  before the AFC re-emission occurs. To retrieve the excitation, another  $\pi$ -pulse back to the excited state where it will continue to rephase; the time between these  $\pi$ -pulses is referred to as  $T_{SW}$ ; this extends the total storage time to  $T_{SW} + 1/\Delta$  [117].

To create an AFC in warm vapour, two lasers are required. The first of these lasers is used to empty the ground state in which the AFC will be made. The so called 'pump' laser is a high-power, large-bandwidth laser used to optically pump the entire ground state population to the other ground state. The second laser is a narrow-band, lower-power laser used to return a narrow population into the AFC ground state, referred to as the 'pump-back' laser. This laser is modulated in frequency to create frequency side bands to return atoms of different frequencies into the AFC ground state. This modulation is used to generate the frequency comb, and the value of this

modulation defines the AFC's comb spacing and, therefore, the protocol's storage time.

#### 2.1.1 Bloch sphere representation

The Bloch sphere is a geometric representation of quantum states in 3d space; these states are represented by vectors on the surface of a sphere [118].

The AFC storage and retrieval protocol has been plotted on a Bloch sphere to represent the process of dephasing and rephasing to the reader; see Fig 2.1. For these plots, the ground state ( $|g\rangle$ ) and excited state ( $|e\rangle$ ) are labelled. The red arrow represents the atomic coherence described in Eq 2.1; this figure assumes an input pulse of area  $\pi/2$  to create a 50:50 superposition of  $|g\rangle$  and  $|e\rangle$  used for visual purposes, as a single-photon input would only rotate the Bloch vector toward the north pole by a minuscule amount.

Fig 2.1a shows the initial state of the ensemble where all the atoms are in the ground state. Fig 2.1b is the Bloch sphere once the photon is inputted into the memory; this vector represents the atomic coherence at t=0, which shows that all the frequency components are initially in phase. The ensemble then starts to dephase due to the different frequency components,  $\omega_n = \omega_0 + n \cdot \delta$ , where  $\omega_n$  is the frequency of a given tooth n,  $\omega_0$  is the frequency of the first AFC tooth and n is the tooth number. There is a range in the rate at which they dephase according to the homogeneous broadening of the ensemble represented by the multiple red vector, these vectors appear to fan out on the Bloch sphere. After a time equal to  $2\pi/\Delta$  (the comb spacing of the AFC), all of these vectors realign, the ensemble rephases, and light is emitted from the memory. Once this has happened, all the atoms are returned to the ground state as seen in Fig 2.1e.

## 2.2 Predicted efficiency

The efficiency of the AFC memory in the forward direction (Eq 2.2) and the backward direction (Eq 2.3) can be defined as:

$$\eta_f \approx \tilde{d}^2 e^{-\tilde{d}} e^{-7/F^2} e^{-d_0}$$
(2.2)

$$\eta_b \approx (1 - e^{-\tilde{d}})^2 e^{-7/F^2} e^{-d_0}$$
(2.3)

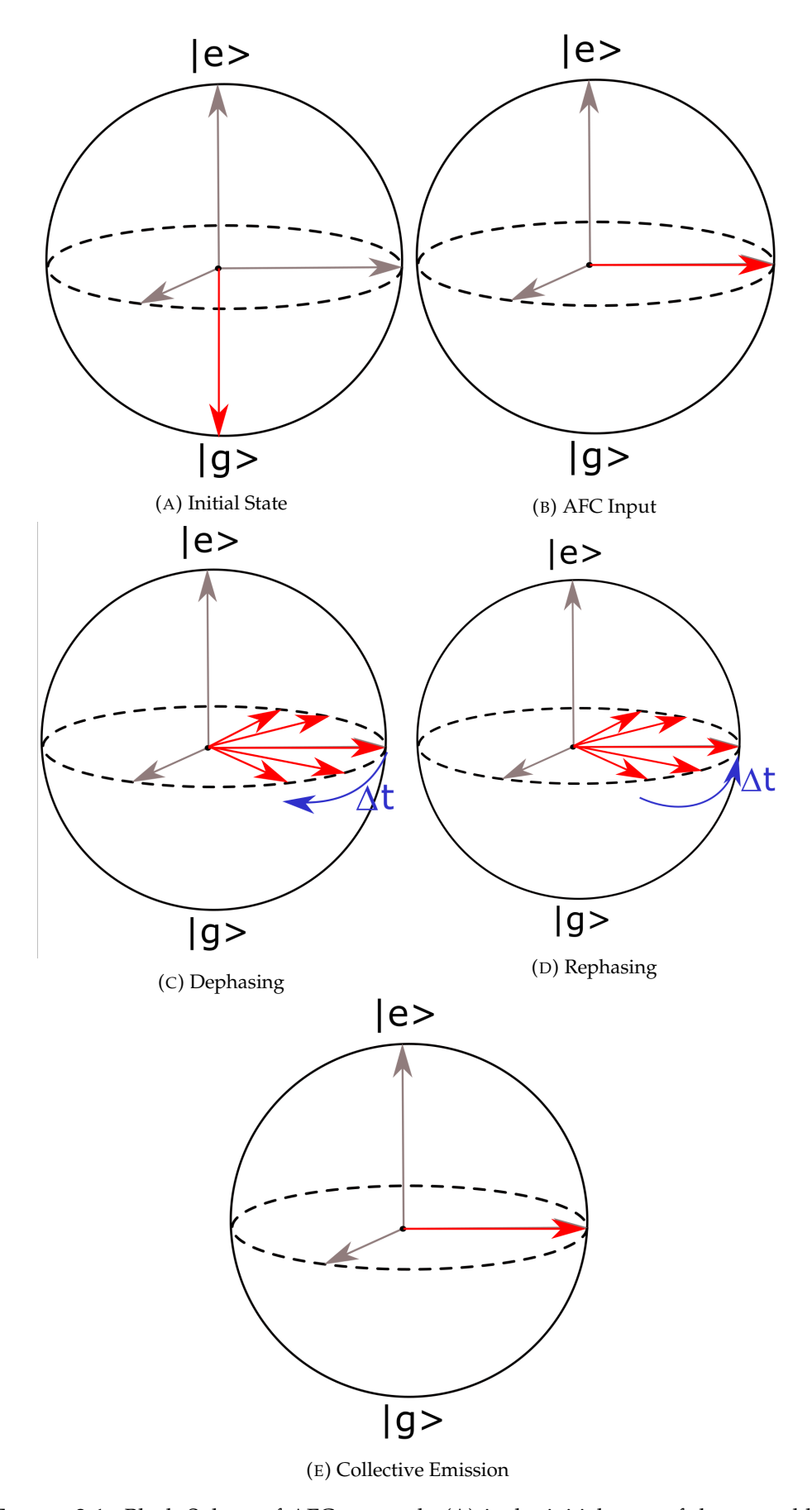


FIGURE 2.1: Bloch Sphere of AFC protocol. (A) is the initial state of the ensemble before the light is stored, (B) is the moment the signal light is absorbed by the AFC, (C) the frequency components of the AFC begin to dephase before rephasing in (D), and at (D) these components are in phase and the light is emitted.

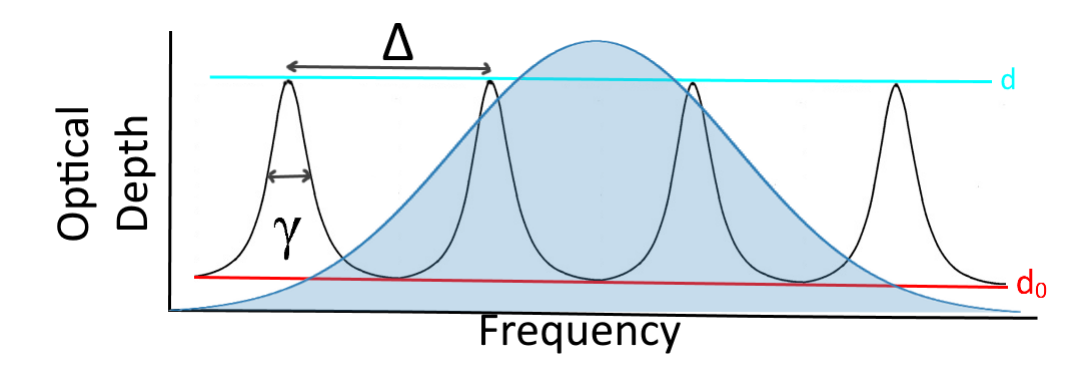


FIGURE 2.2: AFC Criteria with labelled parameters.  $\Delta$  - tooth separation,  $\gamma$  - tooth width, d - optical depth of the teeth and  $d_0$  - background optical depth. The blue region represents the input photon

where  $\tilde{d} = d/F$  and d is the maximum optical depth of the comb, F is the finesse  $F = \Delta/\gamma$  characterised by the comb width  $(\gamma)$  and the comb separation  $(\Delta)$  and  $d_0$  is the background optical depth [119]. These parameters are expressed in Fig 2.2, and the input photon (shaded blue region) is also represented. This equation is based on perfect Gaussian teeth and inputs. This may not be the case, and the efficiency measured will not perfectly match the theoretical value. This equation gives a close enough approximation and can also improve our understanding of how the protocol behaves.

From Eq 2.2, the first term  $(\tilde{d}^2)$  defines how well the AFC can absorb a photon, the second term  $(e^{-\tilde{d}})$  is the dephasing factor due to the width of the teeth. The third term  $(e^{-7/F^2})$  is the loss of the photons through absorption by the rest of the atomic ensemble, and the final term  $(e^{-d_0})$  is the effect of the underlying population underneath the AFC [120].

This means the most efficient AFCs are made with optically deep (large d), narrow peaks (high F) with a low background population. Many AFC teeth are favourable for storing high-bandwidth photons or a more significant number of input modes with different frequencies.

To change these variables experimentally, the  $\Delta$  is defined by the modulation of the pump-back laser (or the separation between different spectral hole burning modes in REIDS),  $\gamma$  is inherently limited by the line width of the transitions used but ultimately limited by the line width of the pump-back/spectral hole laser. For higher-power pump-back lasers, power broadening becomes a significant consideration; this is investigated in Chapter 3. The OD of the AFC (d) is determined by the power of the pump-back laser and the total OD of the ensemble, as a larger initial OD means that more atoms are available to create the AFC. Finally, the background population  $d_0$  is limited by how well the pump laser empties the AFC ground state; any leftover atomic population will not be shaped into the AFC. This value also relies on  $\Delta$  and  $\gamma$  as if the teeth of the comb overlap, then the  $d_0$  increases.

#### 2.2.1 Storage Time Derivation

This derivation makes a certain number of assumptions. The first of these is that the AFC is built off an ensemble of two-level atoms ( $|g\rangle$  and  $|e\rangle$ ), therefore ignoring the atoms in the other ground state. The input light field is also treated as a 1-dimensional light mode. This model describes light mapping into the atoms, atomic evolution, and inhomogeneous dephasing and rephasing in the AFC protocol. It does not describe the population relaxation time ( $T_1$ ) and the decoherence time ( $T_2$ ), as the AFC is based on an inhomogeneously broadened transition, the dephasing time ( $T_2$ ) is much less than the relaxation and decoherence times,  $T_3$  and can therefore be ignored. The width of an individual AFC tooth is limited by the homogeneous line width of the transition used,  $T_1$  and  $T_2$ . The linewidth depends on  $T_2$  due to the time-frequency uncertainty, meaning that these are inversely proportional, therefore a longer excited state liftime the narrower the transitions linewidth.

The atomic spectral distribution  $n(\delta)$  can be defined as [89]:

$$n(\delta) \propto e^{-\delta^2/2\Gamma^2} \sum_{j=-\infty}^{\infty} e^{-(\delta-j\Delta)^2/(2\tilde{\gamma}^2)}$$
 (2.4)

This represents an AFC with Gaussian teeth characterised by a peak separation  $\Delta$ , individual peak width ( $\tilde{\gamma}$ ) and an overall comb width  $\Gamma$ . The Full Width Half-Max (FWHM) of an individual tooth is defined as  $\gamma = \sqrt{8ln2}\tilde{\gamma}$ 

Assume an input photon with a width  $\gamma_p$  that is less than the total AFC width but greater than the comb separation and the width of an individual tooth satisfying the inequality:  $\tilde{\gamma} << \Delta << \gamma_p << \Gamma$ .

Consider a forward propagating light field  $E_f(Z,t)$  going through a gas cell of length L,

$$E_f(L,t) = E_f(0,t)e^{-\tilde{\alpha}L/2} = E_f(0,t)e^{-\tilde{d}/2}$$
(2.5)

where  $\tilde{\alpha} = \frac{\alpha}{F} \sqrt{\frac{\pi}{4ln2}}$ ,  $\alpha$  is the absorption coefficient, and the effective absorption depth is defined as  $\tilde{d} = \tilde{\alpha}L$ . The effective absorption can then be approximated to  $\tilde{d} \approx d/F$  as  $\sqrt{\frac{\pi}{4ln2}} \approx 1$ . As the number of atoms addressed by the input photon  $\gamma_p$  is reduced by the creation of the AFC by a factor of 1/F, the absorption is also reduced by the same factor compared to the natural population of the ground state.

A photon with width  $\gamma_p$  has a Fourier limited temporal resolution of  $1/\gamma_p$ . As  $\gamma_p >> \Delta$ , the photon cannot resolve the features of the AFC and therefore the absorption profile behaves as if there are no dips on optical depth, this leads to

efficient absorption. In addition, if the AFC's optical depth (d) is strong enough, the light can be nearly 100% absorbed.

If we take the Fourier transform of Eq 2.4 we get,

$$\tilde{n}(t) \propto e^{-t\tilde{\gamma}^2/2} \sum_{j=-\infty}^{\infty} e^{-(t-2\pi j/\Delta)^2 \Gamma^2/2}$$
(2.6)

This equation describes a series of peaks in time with a separation of  $2\pi/\Delta$  and a width of  $1/\tilde{\gamma}$ , where the storage time of the protocol is  $2\pi/\Delta$ . This also means that there are higher-order retrieved signals equal to  $4\pi/\Delta$ ,  $6\pi/\Delta$ , etc.

#### 2.2.2 Theoretical Efficiency Plots

If we take Eq 2.2 and plot the variables against one another, we can see the efficiency's limits and behaviour under different AFC structures. This can be seen in Fig 2.3, where one of the values of the equation is changed, and the total efficiency is calculated for each of these new values. Unless stated otherwise, the values of the equation used are as follows:  $d_0 = 0.001$ ,  $\Delta = 133 \mathrm{MHz}$ ,  $\gamma = 30 \mathrm{MHz}$ , giving a value of F = 4.33 with an optical depth ranging from 0 to 150; these values will become clear later as these are the common comb separation and width used to create the AFC for the results section of this thesis. From Eq 2.2, one can determine that the max efficiency (54%) occurs when  $\tilde{d} = 2$ .

Fig 2.3a shows how the efficiency changes with the optical depth (d) of the AFC peaks; as the OD increases, the efficiency peaks and then decreases close to zero for OD greater than 60. The physical interpretation of this effect is that as the optical depth of the AFC increases, there becomes a higher chance of the photon being reabsorbed before it reaches the end of the ensemble. With considerable optical depths, this becomes a guarantee.

Fig 2.3b is a similar plot but is a comparison of the two possible pump-back lasers used in the experiment, which defines the width of the teeth in the AFC; this indicates that the narrower width Toptica DFB laser shall be used over the alternative Butterfly DBR Laser. These linewidths are 32.4 MHz and 80.5 MHz respectively and were measured using a Febry-Perot cavity, more details on this in Chapter 3. Note that the Febry-Perot has limited resolution so is only used here to inidcate that the DBR is narrower. A more appropriate linewidth measurement would be a self-homodyne [121].

Fig 2.3c compares different possible comb separations for making the AFC based on the atomic excited state separations of  $^{87}$ Rb; these will determine the possible storage times of the memory and plotted with a comb width  $\gamma$  =30MHz. There is a higher

potential efficiency for the larger comb separation values as the finesse is larger for larger  $\Delta$ , so the effect of  $e^{-7/F^2}$  is less.

Fig 2.3d varies the  $\gamma$  in intervals of 5MHz, with the typical  $\Delta$  = 133MHz, and plotting the theoretical efficiency. This shows that a lower Gaussian width is preferable for making an AFC memory. A narrower tooth width means a narrower distribution of velocities and higher finesse and, therefore, a shorter dephasing time of the ensemble - the effect of  $e^{-7/F^2}$  is smaller.

Fig 2.3e and Fig 2.3f vary the comb separation  $\Delta$  and tooth width  $\gamma$  of the ensemble to compare the effect these values have on efficiency; this shows that the predicted efficiency plateaus out at roughly 54%.

These plots will be used later in the results chapter of this thesis (Chapter 4) as a theoretical comparison to the AFC experiments performed.

#### 2.3 State of the art

The AFC protocol was first proposed in 2008 by Mikael Afzelius, Christoph Simon, Hugues de Riedmatten, and Nicolas Gisin [89] with the first experimental demonstration later that year by the same group [122] in a Neodymium (Nd $^{3+}$ ) doped into a crystal Nd $^{3+}$ : YVO<sub>4</sub>. This paper demonstrated the multimode capability of the memory at the single-photon level with a storage time ranging from 150ns to 1100ns and an efficiency range of 0.4 % to 0.004%.

AFCs are commonly demonstrated in Rare-Earth Ion-Doped Solids (REIDS) [123; 119; 124] due to their capacity to allow for extended storage times [117]. The longest storage time is set at 1 hour in a europium-doped yttrium orthosilicate ( $^{151}Eu^{3+}: Y_2SiO_5$ ) crystal [125]. This is achieved using a zero-first-order-Zeeman (ZEFOZ) magnetic field and dynamical decoupling (DD) to lift the degeneracy of the ground states and allow for the inputted light to be mapped into a long-lived ground state creating a spin-wave coherence.

The AFC made in this paper has a comb separation  $\Delta$  = 100kHz, giving a raw AFC storage time of 10 $\mu$ s. Once the AFC absorbs the inputted light, a high power (360mW) control pulse is used to map this excitation into one of the Zeeman ground states to create this long coherence time spin-wave state. A DD sequence is then applied to protect this coherence. Finally, a second control pulse maps the spin-coherence back into its initial excited state to resume the rephasing and retrieve the input light. While the total excited state rephasing time is equal to  $10\mu$ s, the long storage time is mainly defined by the time the light spends in this spin-wave coherence.

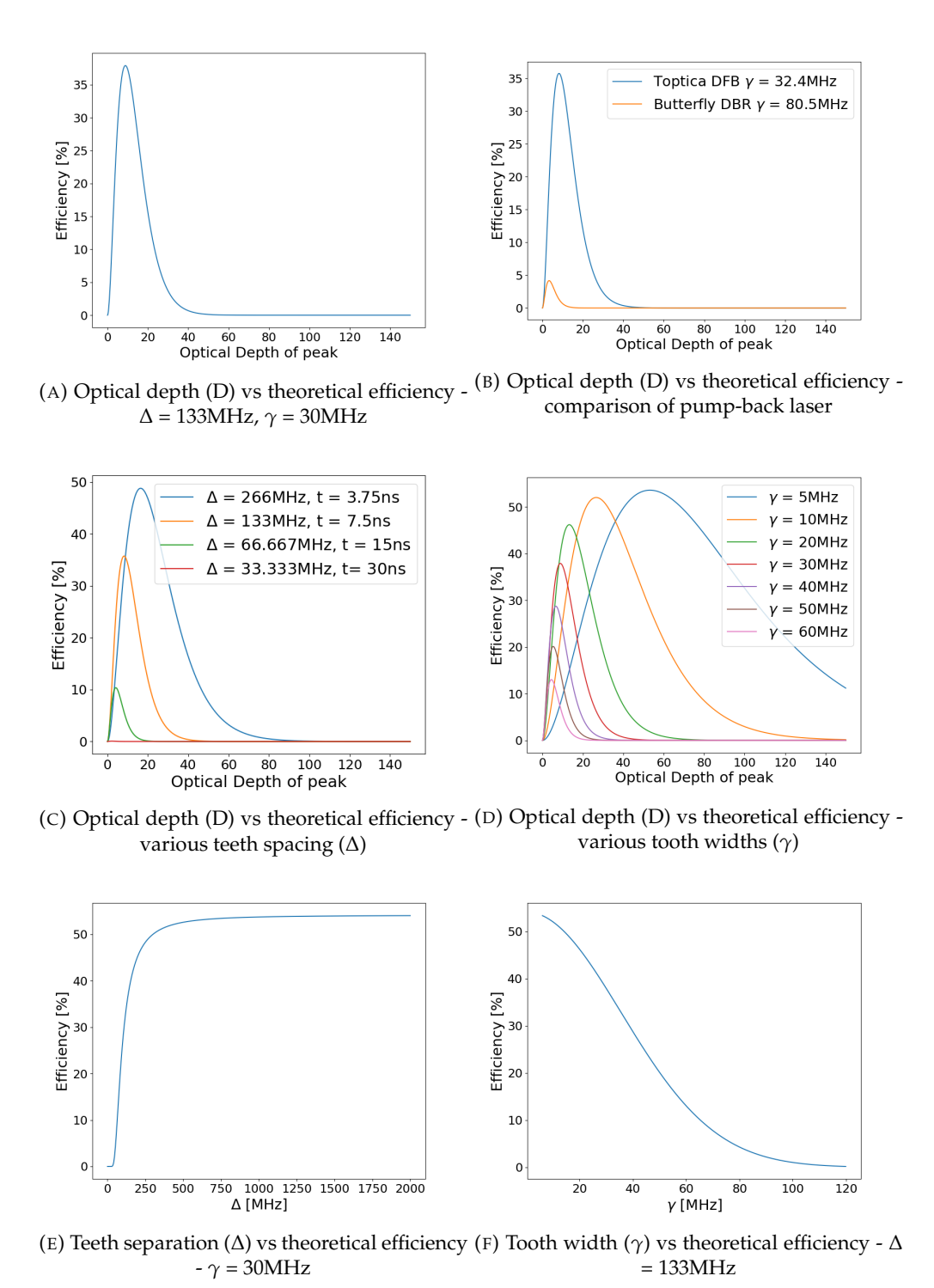


FIGURE 2.3: AFC Efficiency Simulations using Eq 2.2, unless stated otherwise,  $d_0$  = 0.001,  $\Delta$  = 133MHz,  $\gamma$  = 30MHz, giving a value of F = 4.33 with an optical depth ranging from 0 to 150

AFC has also been demonstrated with a resonant cavity-enhanced SPDC. This source converts a 426nm pump laser into two photons: a telecom idler photon at 1436nm and a signal photon at 606nm. The signal is stored via AFC for 47.7 $\mu$ s and for a storage time of 2  $\mu$ s a fidelity of 92% was measured. The longer storage time allows for this pair to be distributed at a distance of up to 10km [126]. A recent paper by the Institute of Photonic Sciences (ICFO) used two spin-wave AFC memory in  $Pr^{3+}: Y_2SiO_5$  crystal and a non-degenerate SPDC heralded source with on-demand and multiplexed sources [127] to create entanglement between these memories. These memories operated with a total storage time of 16.5  $\mu$ s with an internal efficiency of 3.25% and 4.50%. This paper provides a step towards using AFC memories in quantum networks.

The AFC memory platform can be placed inside an optical cavity to enhance the absorption probability; this was demonstrated in an intrinsically low-absorbing  $^{151}Eu^{3+}: Y_2SiO_5$  crystal with a storage time of  $2\mu$ s and  $10\mu$ s with an efficiency of 53% and 28% respectively [128]. This paper also demonstrates this cavity enhancement with the spin-wave AFC storage to achieve a 12-fold increase in efficiency of this protocol (reaching 12%). A cavity-enhanced AFC was also demonstrated in a  $Pr^{3+}: Y_2SiO_5$  at ICFO, this cavity approach over comes the 54% limit of total efficiency with a low finesse cavity in the impedance-matched regime, this allowed ICFO to achieve a total efficiency of 60% for a  $2\mu$ s storage time [129].

As stated previously, the AFC protocol has multimodal capabilities; [130] shows the AFC protocol in a  $^{151}Eu^{3+}$ :  $Y_2SiO_5$  crystal with six temporal modes stored and retrieved with a fidelity F =  $85 \pm 2\%$  for an average photon number of  $\mu = 0.92 \pm 0.04$ . 1250 modes have also been demonstrated in a  $^{171}Yb^{3+}$ :  $Y_2SiO_5$  crystal with a storage time of  $25\mu$ s. One can also introduce multiple frequency modes along a broad AFC, [131] demonstrated this with 26 spectral modes with a fidelity of 97%.

AFC has also been proposed within a single atom within an optical cavity [132] referred to as the IAFC (Intra-Atomic Frequency Comb), which is built upon atomic transitions to create an 'on-chip' quantum memory - this a micro-platform for memories based on one-atom. This approach has a theoretical efficiency of 100% due to only using one atom compared to an ensemble. There is no chance of the ensemble reabsorbing the light. The AFC teeth in the IAFC are created using natural transitions and a strong magnetic field to define the comb separation. This paper discusses using Rubidium and Caesium as platforms for this protocol. Due to only using one atom, Doppler effects can be ignored; therefore, this can be performed at ambient temperatures.

In [133] the AFC protocol was demonstrated with 1650 modes of telecom single photons (produced from an SPDC heralded source) in a 10-m-long cryogenically cooled erbium-doped silica fibre with efficiency ranging from 0.1% - 1%.

AFC has been demonstrated in a warm vapour protocol using a Caesium ensemble by D. Main et al. in 2020 [134]. This paper forms the foundation of the research I carried out during my PhD, as the single photon level performance has not been verified. In contrast, this paper contains a similar experiment; the warm vapour AFC protocol needs to be investigated more thoroughly in this thesis. D. Main demonstrated this protocol with two different storage times of 8ns and 12ns, with an efficiency of 9.3  $\pm$  0.6 % and 3.4  $\pm$  0.3 %, respectively. The AFC was made on the D2 line with a wavelength of 852nm.

#### 2.4 Conclusion

As one can see, the Atomic Frequency Comb protocol has yet to be demonstrated in Warm Rubidium vapour. It has been demonstrated in warm Caesium vapour (as mentioned in the paper by D. Main [134]); therefore, it stands to reason that it can be demonstrated in Rb vapour as well. Both of these atoms are Alkali metals and thus have similar atomic structures, meaning that the same experimental techniques can be used to implement this protocol in Rb. These techniques will be outlined in more detail in future chapters. The next chapter will outline the construction of this AFC memory protocol within the warm <sup>87</sup>Rb platform.

# Chapter 3

# Warm Vapour Implementations of AFC

This chapter is split into 4 sections, the first of these is the energy level structure of <sup>87</sup>Rb and how associated lasers are involved in creating the AFC. Next, the complete experimental setup used in all AFC experiments in this thesis with details on how to realise this protocol on the warm Rubidium vapour platform. Section 3.3 addresses the main issue with this platform - the Doppler decoherence - and a method called velocity selective pumping (VSP) method that is used to overcome this, the experimental method of which is similar to that of creating the AFC structure. The final section is the first demonstration of the ORCA quantum memory using telecom wavelengths for the input light for the <sup>87</sup>Rb platform. The VSP experiment was built and performed by myself with its ultimate goal to use it as the base for the AFC experiment that will be used to characterise the single-photon level compatibility of the memory. The ORCA experiments was built by the collaborators at Imperial College London (ICL), where I was present for the data acquisitions and provided code for the temperature characterisation of the cell.

## 3.1 Rb energy levels

Rubidium (Rb) is an Alkali metal meaning that has one electron in its outermost shell [135], which means that the atomic structure is relatively simple and therefore the atomic transitions and hyperfine splittings are easy to calculate [136]. Rb has 36 isotopes with the most common isotopes being <sup>85</sup>Rb (making up 72.2% of its natural abundance [137]) and, the isotope of interest in this work, <sup>87</sup>Rb (making up 27.7% of the natural abundance). Rb is a popular platform for neutral atom quantum computers [138] offering precise control in large scale quantum computing (large

qubit number) [139]. Rb is also used for atomic clocks [140] and Bose-Einstein condensate experiments [141].

The angular momentum of this electron structure can be calculated using the following equation; J = L + S, where, J is the electron angular momentum, L is the orbital angular momentum, and S is the electron spin momentum. For the ground state of  $^{87}$ Rb; L = 0, S = 1/2 and therefore J = 1/2. For the 1st excited state; L = 1 and J = 1/2 or 3/2. This forms the D line which has two allowed routes;  $D1: 5^2S_{1/2} \rightarrow 5^2P_{1/2}$  and  $D2: 5^2S_{1/2} \rightarrow 5^2P_{3/2}$  with wavelength of 795nm and 780nm respectively, seen in Fig 3.1. Here, the number 5 is the principal quantum number S0 which tells us that the outermost single electron is in the 5th shell, the superscript 2 is defined by S1 - for an unpaired electron S3 = S2 thus the superscript is 2, S3 corresponds to S3 and finally the subscript represents the total angular momentum S1.

The total Atomic angular momentum is defined by F = J + I, where I is the nuclear spin. For the <sup>87</sup>Rb ground state, J = 1/2, and I = 3/2 therefore the two ground states are F = 1,2 as  $|J - I| \le F \le J + I$ . For the excited state; D1 (5<sup>2</sup>S<sub>1/2</sub>), F = 1,2 and D2 (5<sup>2</sup>S<sub>1/2</sub>) F = 0,1,2,3.

Fig 3.1 shows the pump and pump-back labelled on the energy level diagram of Rubidium 87, this diagram is drawn from the information provided by Daniel A. Steck [142]. The lasers required to create the AFC in the F = 2 ground state (the pump and pump-back lasers) are also labelled on this energy level diagram as well as the transition that the input signal is resonant with, the colours picked for these lasers are consistent with the lasers in the experimental diagrams (Fig 3.3, 4.1, 4.9, 5.1).

The line width of these transitions is 6MHz [142], this is the lower limit for the width of an individual AFC tooth ( $\gamma$ ). The next limiting factor of the variable  $\gamma$  is the line width of the laser which pumps back all atoms in its frequency range.

Not labelled on this Figure are the higher order telecom transitions from the  $5P_{3/2}$  excited state to the  $4D_{5/2}$  and  $4D_{3/2}$ , the wavelength of these transitions are 1529.4nm and 1529.3nm respectively [143]. These transitions lie just outside the low loss telecom c-band (1530nm - 1565nm [88]) but still have low propagation loss. This means that these transitions can be used to implement a quantum memory for telecommunication networks over large distances.

Fig 3.2 shows the cross section of the Rb cell with labelled laser modes, the grey represents the ensemble of Rb atoms within the cylindrical gas cell, the blue represents the pump laser, the green is for the pump-back and the signal is red. The pump and pump-back lasers have a large cross-section in order to efficiently pump the atoms that the signal will address. In this figure the pump has a larger cross sectional area compared to the pump-back because this configuration prepares a larger number of atoms compared to the number of atoms used for the memory, thus atoms moving

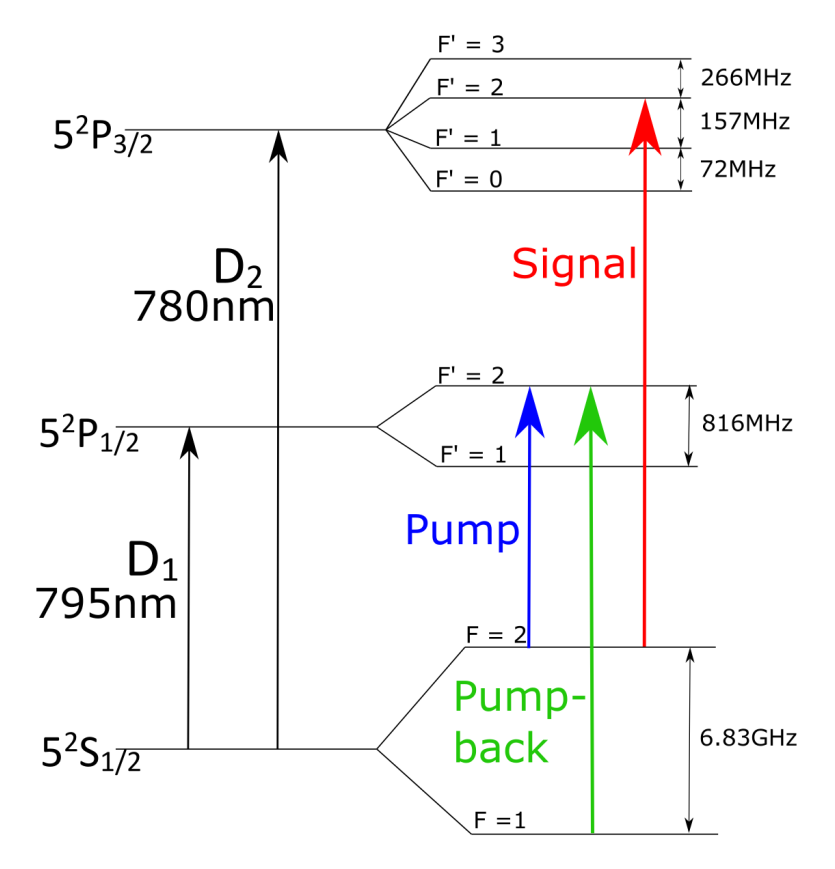


FIGURE 3.1: Energy level diagram for AFC in <sup>87</sup>Rb with labelled AFC preparation and input signal lasers

into the signals path are also prepared as an AFC. This ensures that the pump-back addresses a subspace that has experienced the near uniform pumping efficiency and the signal covers an area that has been addressed by both.

# 3.2 Experimental details

The complete experimental diagram is shown in Fig 3.3.

As described earlier, the signal is on the D2 (780nm) <sup>87</sup>Rb line, and the pump and pump-back are on the D1 (795nm) line. These pump and pump-back lasers are counter-propagating in free space to the signal laser; this reduces the 795nm light from leaking through the experiment. The difference in wavelength also allows wavelength-dependent optics to be used; for example, the dichroic mirror (LPD02-785RU-25) sends the 780nm signal light down towards the detectors while transmitting the 795nm light towards the cell with the extinction ratio of these mirrors rated at about 200:1. Wavelength filters (FBH780-10, Semrock LL01-780-25 F1) are also used near the start of the signals path (the end of the pump and pump-back path) to stop the pump and pump-back light from coupling into the signals fibre. These filters are at a slight angle so that the reflected light does not pass back through the cell. The

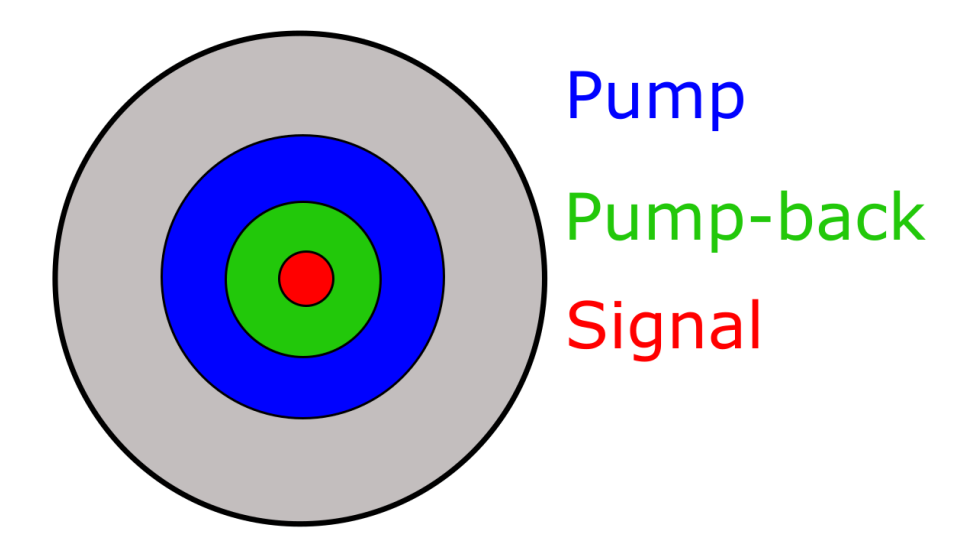


FIGURE 3.2: Cross section of Rb cell with laser modes. The grey area is the atomic gas cell, the blue region is the cross section of the pump laser, the green region is the pump-back laser and the red region is the signal laser.

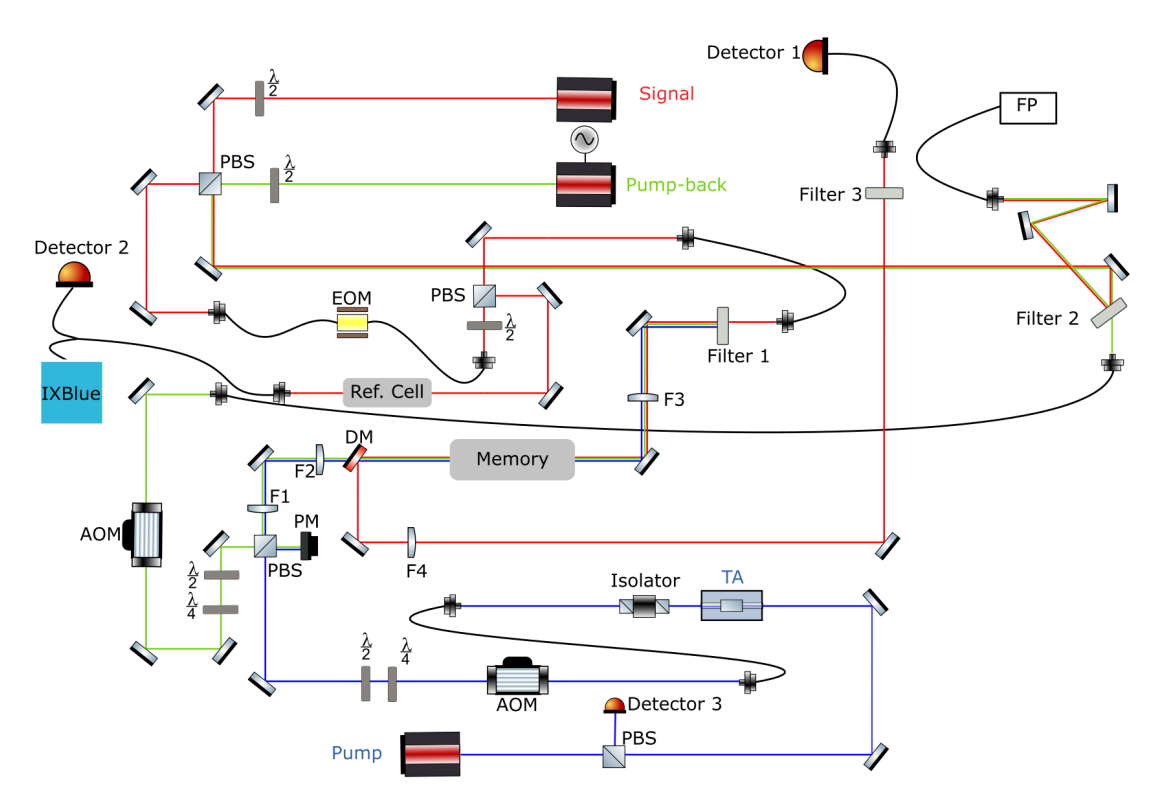


FIGURE 3.3: Complete Experimental Setup. Key: AOM - Acoustic-Optical Modulator, DM - Dichroic Mirror, EOM - Electro-Optic Modulator, F1,2,3,4 - Lenses (focal length; 1=40mm, 2=100mm, 3=150mm, 4=150mm), FP - Fabry-Perot, PBS - Polarising Beam Splitter, PM - Power Meter, TA - Tapered Amplifier

fibres used in this experiment are mainly P3-780A-FC-1 (single-mode patch cables for 780 - 970 nm light); these have a propagation loss of less than 3.5 dB/km for 780nm light [144].

To efficiently pump the population of a ground state, the pump laser (Butterfly DBR Laser - DBR795PN) needs to be optically amplified. Therefore, this laser goes through a Tapered Amplifier (TA) to boost its power from 20mW to roughly 1.5W, which ends up at about 100mW at the cell due to loss throughout the experiment and the AOM. The TA is a Toptica tapered amplifier in a home-built housing that uses aspheric lenses to focus the light onto the TA chip and collimate the output, followed by some correction optics to fix the shape of the output light. The loss of the amplified light through the experiment is mainly due to two factors; the first of these is that the TAs output is coupled into a fibre to correct its mode shape further and to transport the light to a different point of the optical table, the coupling into this fibre has an efficiency of 33%, this coupling efficiency is low due to the asymmetric mode shape of the TA output. After the fibre, this light goes through an AOM with a 1st spatial mode efficiency of 30%.

To avoid damaging the TA, a seed laser needs to be on the chip at all times; thus, the seed lasers are monitored with a detector (Detector 3 on Fig 3.3), which is placed after the reflected port of a PBS. The signal from the detector is fed to a relay, and its output is connected to the interlock input of the TA current driver; this prevents damage to the TA if the seed laser is accidentally turned off by turning off the current input to the TA. This PBS also allows for a least 10mW of seed laser coupled into the TA (the minimum power required to function without causing damage); the typical seed power used is 20mW.

The output also goes through a Faraday isolator to stop reflections from the fibre from coupling back into the TA. This isolater also reduces the power of the TA output and has a transmission efficiency of 80%.

The pump-back laser is a Toptica Distributed Feedback Diode (DFB) Pro laser whose AC modulation is driven by an Arbitrary Waveform Generator (AWG) to generate frequency-modulated sidebands at the driving frequency. This laser enters one port of a PBS (top left PBS) via a half-wave plate, while the other input port has the signal laser via another half-wave plate. One output port of this PBS was coupled to the fibre-based EOM; the waveplates are such that the maximal(minimal) signal(pump-back) laser couples to the EOM which is used to create the input pulses of light towards the memory. The other output port of the PBS has a minimal amount of signal laser power and a maximal amount of pump-back laser power, and they are overlapped. A FELH0800 long-pass filter (F2) was used to reflect the signal laser, and a minimal amount of the pump-back laser was coupled to a scanning Fabry-Perot cavity (FP) for laser frequency characterisation. This characterisation was done by

hand by taking a trace of the frequency at the start of the experiment and adjusting the pump-back frequency on the lasers controller model whenever it drifts. Finally, the transmitted part of the filter was coupled to a fibre for the memory experiment.

Most of the pump-back laser's optical power is coupled into a fibre (with a coupling efficiency of 25%, giving around 20mW on the fibre's output).

The pump and pump-back lasers are combined on a PBS to overlap the modes going through the cell. Both of these lasers go through a Quarter ( $\lambda/4$ ) and Half ( $\lambda/2$ ) waveplate used to change the amount of power in each channel on the PBS (bottom left PBS in Fig 3.3). The pump has maximal power transmitting through the PBS, and the pump-back can be varied to create the optimal AFC structure. A power meter (PM) on the remaining channel of the PBS is used to monitor the dumped power from both of these lasers. These overlapped lasers go through an f=40mm and then an f=100mm lens to get a 2.5x increase in beam size to match Fig 3.2r.

There are two irises on either side of the memory cell (not labelled on Fig 3.3), which are used to align all lasers propagating through the cell; this guarantees the overlap of the laser modes.

The signal laser is a Thorlabs Distributed Bragg reflector (DBR) laser (DBR780PN). The modulation input of the current driver of this laser (Thorlabs LM14S2—Universal 14-Pin Butterfly Laser Diode Mount) is driven with an AWG typically at 25Hz with an amplitude of 150mVpp for scanning the signal laser's frequency in order to perform spectroscopic measurements. The AWG is set to DC mode when a fixed frequency is required for memory experiments and is changed by varying the DC offset of the AWG.

After the EOM, the signal power is split using an HWP so that some of the lasers can scan a reference cell while the rest goes into another fibre to be sent to the memory. Coupling the laser into another fibre serves two purposes: (1) it allows the inclusion of neutral density (ND) filters to lower the input photon number to the single photon level before the fibre without disturbing the alignment to the memory; (2) this allows for the flexibility to change the memory input with a single photon source with ease.

The signal passes through a set of lenses (F3 and F4), both with a focal length of f=150mm, to focus the light in the middle of the cell. This ensures that the input light is much smaller than the pump and pump-back modes so that the input sees a more uniform preparation of the atoms. Focusing the signal also increases the interaction of the light with the atoms; the light-matter interaction is defined as  $\mathbf{D} \cdot \mathbf{E}$  where  $\mathbf{D}$  is the transition dipole moment of the atom and  $\mathbf{E}$  is the electric field. The electric field is proportional to the square root of intensity, which is inversely proportional to the area of the spatial mode. i.e. for a given power, the more you focus, the higher the intensity and, therefore, the light-matter interaction.

The memory's output is coupled into another fibre to change the type of detector used to measure this signal. One of these detectors is Thorlabs APD430A used when the signal laser is scanned to measure the spectra of the atoms, another detector is a Menlo APD210 fast detector used to measure the input and recalled pulses in the AFC and finally a single-photon detector (PerkinElmer spcm-aq4c) is used for single-photon level inputs, which is investigated in Chapters 5 and 6. Finally, another set of filters (FBH780-10, Semrock LL01-780-25), F3, is placed before this detection fibre to block any pump or pump-back light from leaking onto the detectors.

Fig 3.3 also includes AOMs within the setup, which are always on during the CW experiments and will be used as intended for the pulsed regime investigations. They are included in the CW experiment (while not being labelled in the future simplified experimental setups) to keep consistent power when changing to the pulsed regime.

#### 3.2.1 Reference cell

As seen in Fig 3.3, there is a second vapour cell within the experiment; this cell contains the natural abundance of Rubidium containing both  $^{87}$ Rb and  $^{85}$ Rb isotopes. This cell is used to calibrate the frequency axis of the Rb spectrum on the oscilloscope using the known ground state separation of the two isotopes [142; 145] and using Python to detect these peaks to find the frequency of the AFC structures made later in chapter 4 to find  $\Gamma$ ,  $\gamma$  and  $\Delta$ .

This cell is also scanned via saturation absorption spectroscopy to see the allowed transitions of <sup>87</sup>Rb and <sup>85</sup>Rb; see Fig 3.4. In this figure, the orange trace is the ground state population for the two Rb isotopes, and the blue trace is the Doppler-free spectrum of the same isotopes. This data was taken with the cell at room temperature.

#### 3.2.2 Fabry-Perot interferometer

The Fabry-Perot interferometer (SA200-5B - Scanning Fabry Perot Interferometer, 535-820 nm, 1.5 GHz FSR), as seen in Fig 3.3, is used to track the drift of the signal and pump-back lasers. A Fabry-Perot interferometer consists of a cavity composed of two mirrors with a variable distance between the two mirrors and a diode at one end. When the laser impinges the cavity, the light will pass through if it is resonant with the length of the cavity. Therefore, if the length of the cavity is varied, then the Fabry-Perot can be used to determine the relative frequency of the laser inside by detecting the light on the diode when the cavity length is resonant with the light. The output of the Fabry-Perot is plotted on an oscilloscope triggered by the scanning rate of the cavity, and this is used to view the drift of the frequency of the laser within the cavity as one can see it 'move' along the x-axis of the oscilloscope as this drift occurs. Therefore, one

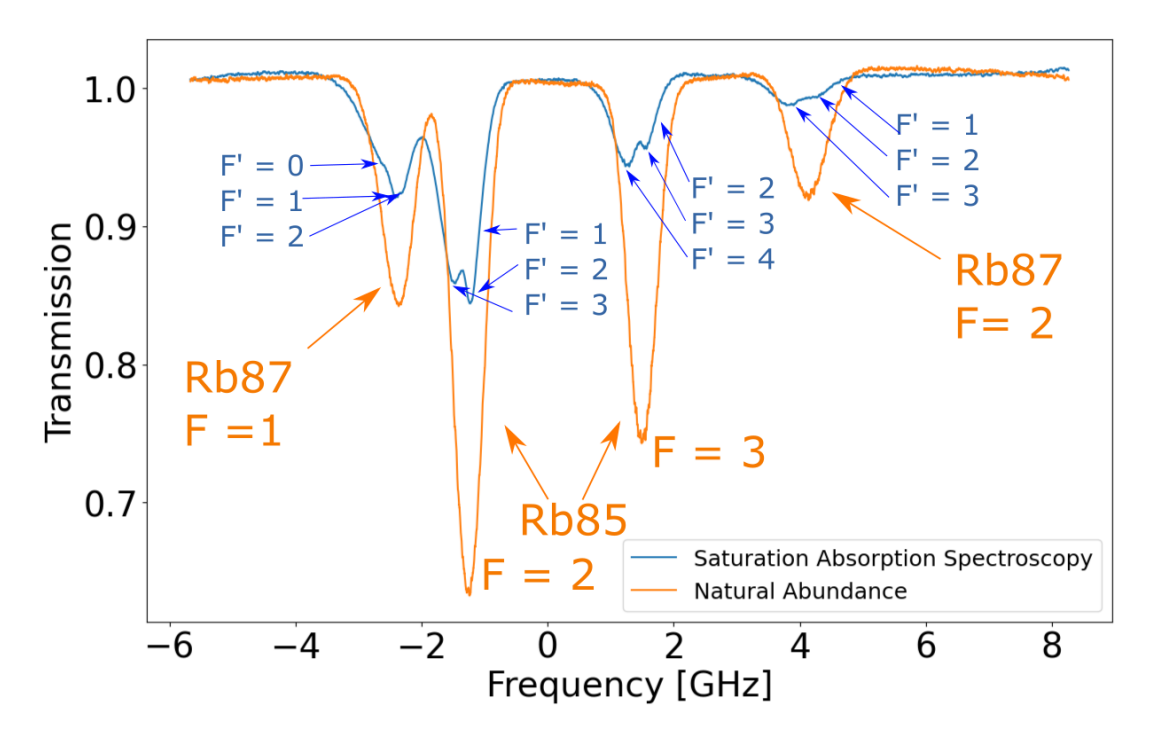


FIGURE 3.4: Saturation absorption spectroscopy of natural abundance Rb. The orange plot is the unpumped spectra with labelled ground states, and the blue plot is the saturation absorption spectroscopy with the labelled transitions

can account for this drift in real-time by taking a reference trace on the oscilloscope and correcting the driving current of the laser when it drifts away from this point.

The laser's current is adjusted to correct for the drifts. For the Toptica laser, this can be done using the computer interface. Typically, adjustments on the order of 0.01mA are needed on a timescale of 1 minute.

#### 3.2.3 Pulse creation

The Electro-Optic Modulator (EOM) creates the input pulses for the memory. This EOM is the NIR-MX800-LN-10-00-P-P-FA-FA iXBlue modulator. The lockbox adjusts the DC bias of this crystal to minimise or maximise the output light. These pulses are created using a programmable pulse generator (ppg) that sends a list of  $512 \times 256$  values, thus this resolution does not allow for perfect curves to be made. Each value corresponds to a 200ps bin, allowing for the pulse shapes to be programmed. This ppg is the ppg512 from PicoQuant.

The signal laser is monitored using the same fibre that contains the output of the reference cell. In order to create these pulses, the fibre is physically moved from the detector used for calibrating the frequency axis of the oscilloscope to the IXBlue,

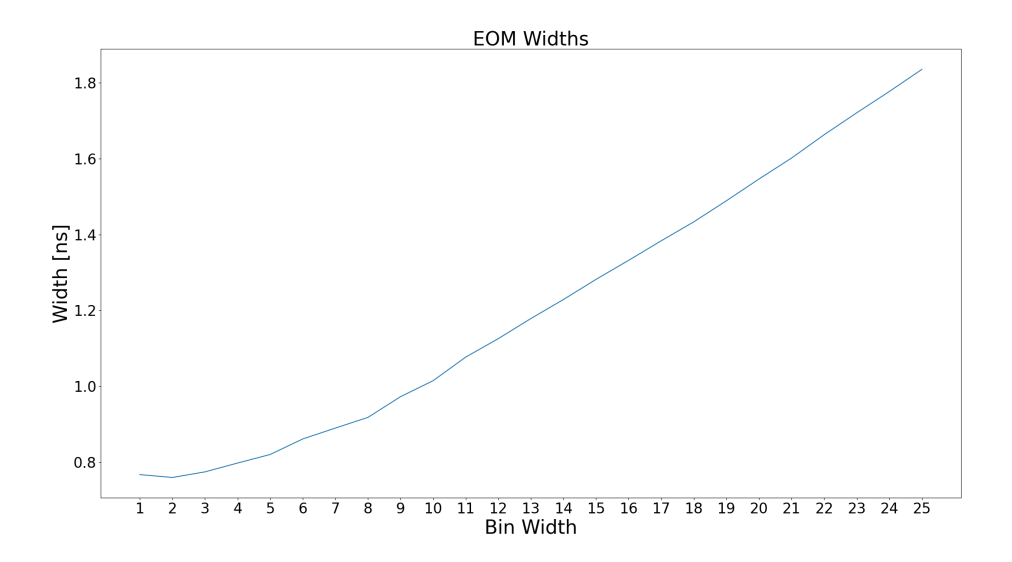


FIGURE 3.5: Varying EOM Widths. The inputted electronic width for the EOM, where 1 bin is 200ps compared to the measured width of the optical pulse created

which is used to change and monitor the DC bias on the EOM. This creates strong pulses with no light outside of the pulse.

Fig 3.5 shows how the measured width of the optical pulse compared to the number of bins drawn in the PPG software, where one bin should equal 200ps. One would expect this relationship to be linear, which is the case of more significant bin numbers; this non-linearity for lower bin numbers is more indicative of the response time of the Menlo APD used to detect these pulses rather than the behaviour of the EOM.

Fig 3.6 shows how the intensity of the optical pulses created by the EOM changes with larger bin widths. This graph shows that the optical pulses saturate at around 13 bins or 6.5ns. This is the region with the best extinction of the EOM and, therefore, the regime in which the EOM should operate effectively. In this figure, the max voltage value measured on the Menlo APD for each pulse was plotted against the inputted bin width in the PPG software.

#### 3.2.4 Beam Mode

The cross-section of the laser beams is measured using a Scanning-Slit Optical Beam Profiler (BP209IR1/M - Dual Scanning Slit Beam Profiler, 500 - 1700 nm,  $\emptyset 2.5 \, \mu m$  -  $\emptyset 9 \, mm$ , Metric) to measure the cross-section of the beams at the centre point of the Rb-87 memory cell, see Fig 3.7. It is useful to understand the shape of the beam. Ideally, the beam needs to have a Gaussian shape, but there are several points along the experiment where this shape is less than favourable. Propagation of Gaussian spatial modes of light is well understood, using, for example, the complex beam parameter

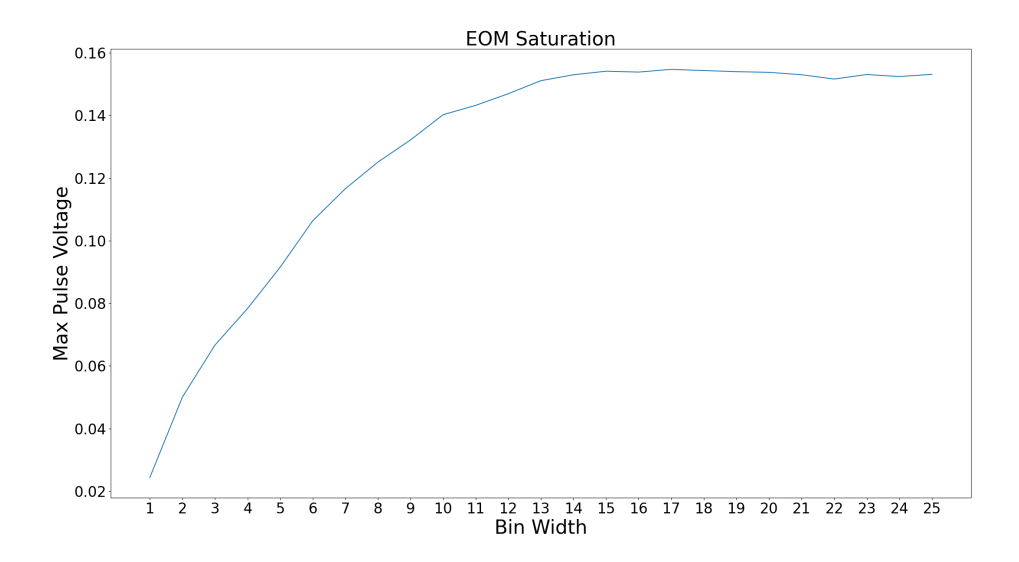


FIGURE 3.6: EOM saturation. This plot compares the height of the optical pulse created vs the input width, this show how the optical pulse height saturates showing the best extinction of the EOM is past 13 bins in width (where 1 bin is 200ps)

and ray transfer matrices. The goal is to have a collimated and circular Gaussian laser beam with lenses to focus and mode match to or from optics such as AOMs, Rb cells, fibres, etc. To achieve this criterion, the output of the Toptica laser and the TA are coupled into single-mode fibres.

The misshaping of beams can occur from several different sources; the first can arise from the output optics from a laser source or a free-space tapered amplifier. The easiest method for correcting this shape is to couple the unfavourable laser mode into an optical fibre, as the fibre output used in this experiment is always single mode; see Fig 3.3 for the placement of these fibres.

The pump laser's beam mode is slightly elliptical, with a diameter in the X direction of 2.841mm and a diameter in the Y direction of 3.178mm. Due to the nature of the TA, the output profile of the beam has a non-perfect Gaussian shape. The pump-back laser has a much stronger Gaussian shape with an X diameter of 1.684mm and a Y diameter of 2.203mm. It is apparent from Fig 3.7d that there is sufficient overlap of these beams with a combined X diameter of 1.964mm and a Y diameter of 2.433mm. These lasers have an imperfect Gaussian shape due to propagating through the AOMs.

Fig 3.7a shows the profile of the signal laser; this is in a different spatial location on the profiler to the other two modes due to the profiler facing the opposite direction than before; this does not mean that these modes do not overlap. The size of the signal is 0.26377mm by 0.25403mm.

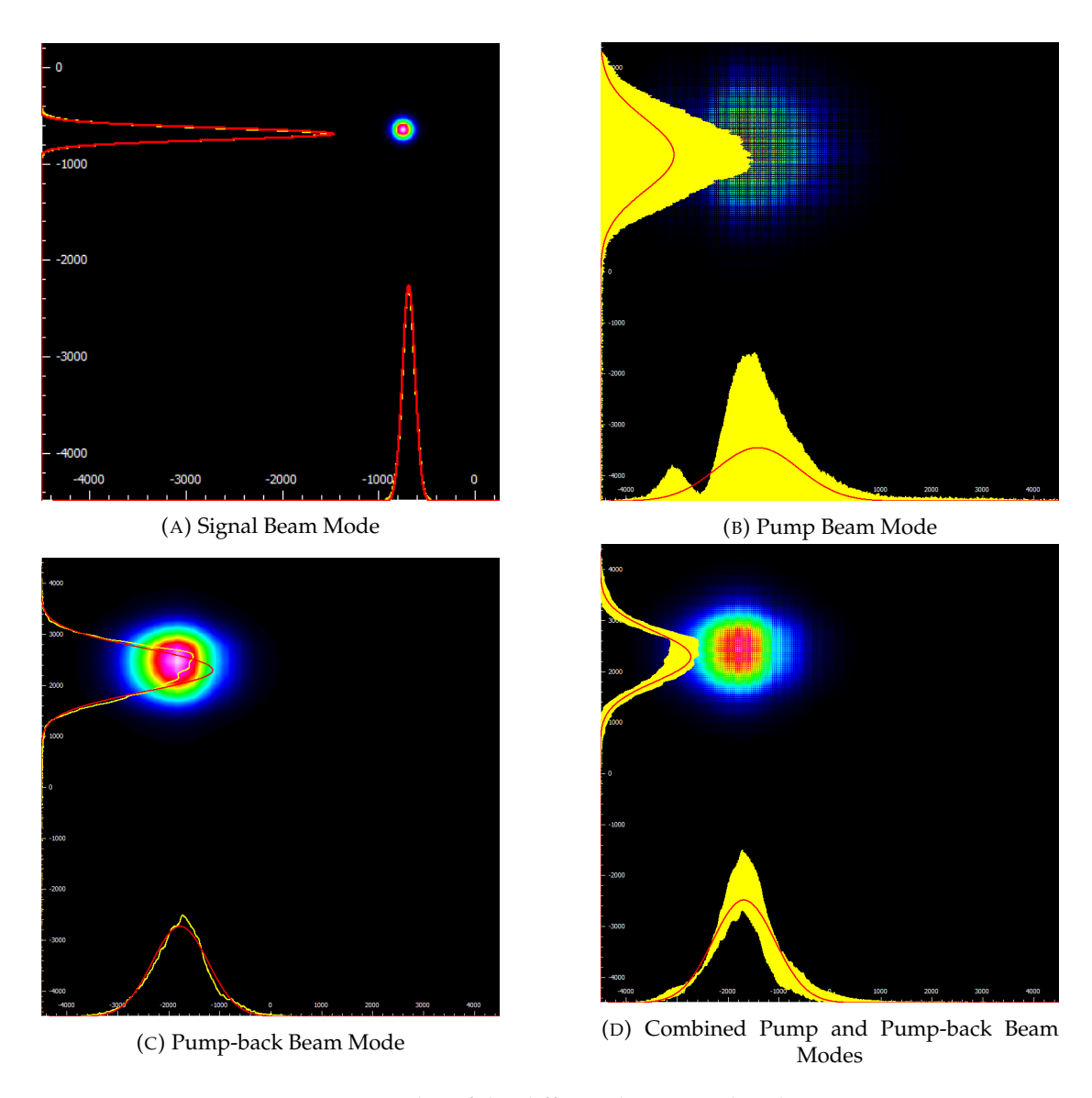


FIGURE 3.7: Beam Modes of the different lasers used in the experiment

#### 3.2.5 Telescope

As seen in Fig 3.3, there is an optical telescope within the path of the pump and pump-back, two lenses with a focal length of 40mm followed by a 100mm length where the focal points of these lenses are focused on the exact location on the optical table. This will increase the cross-sectional area of the light going through this telescope by a ratio of 1:2.5. This larger area allows for easier overlap of the signal to the pump and pump-back, ensuring that the signal is deep within the region where the AFC is created within the atoms in the cell. This overlap can be seen in Fig 3.3.

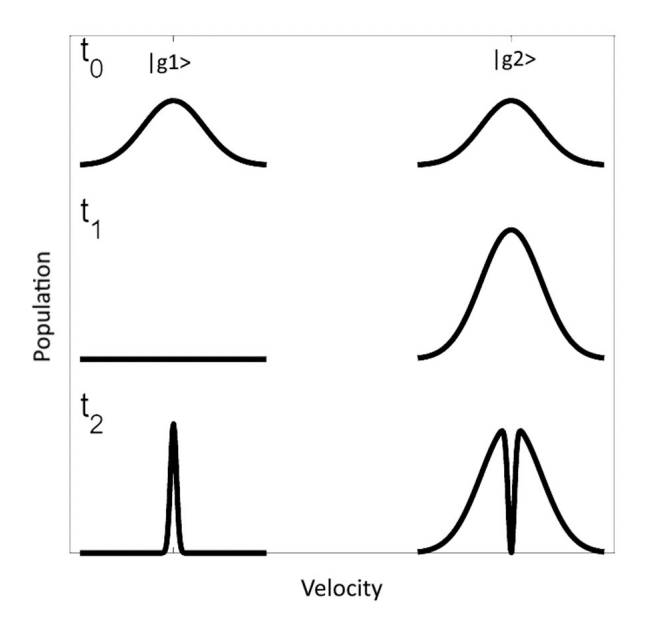


FIGURE 3.8: VSP Sequencing. At  $t_0$  the atoms are distributed between the two ground states each with a Maxwell-Boltzmann distribution of velocities, at  $t_1$  all the atoms are pumped into one of the ground states ( $|g2\rangle$ ), finally a narrow velocity class is returned to  $|g1\rangle$  at  $t_2$ .

#### 3.2.6 Transmission efficiency

When determining the efficiency of the whole experiment, one must consider the transmission efficiency of the experiment along with the efficiency of light recalled after storage. As the light propagates through the experiment, it interacts with several different optics, all of which have a loss associated with them. Therefore, the power was measured before and after each of these optics to determine the transmission efficiency ( $\eta_{trans}$ ) of the experiment. This will then be used to calculate the end-to-end efficiency of the whole experiment, as  $\eta_{e2e} = \eta_{tot} \cdot \eta_{trans}$ .

The largest source of loss in the experiment was the optical fibre that the memory outputs couples to be sent to a detector; this is labelled as just a detector in the experimental diagram in Fig 4.1, the coupling efficiency of this is roughly 75% with all the other optics (and Rb cell) having a transmission efficiency of over 95%. This gives an overall experimental transmission efficiency of 70%.

# 3.3 Velocity selective pumping

While warm vapour platforms offer large optical depths at ambient temperatures the velocity at which these atoms move becomes an important consideration. Moving atoms will collide with each other, leading to short coherence times as colliding atoms can transfer momentum and change the ground state of a given atom ruining the AFC structure. When optically addressing atomic ensembles of fast moving atoms,

individual atoms that are pumped will quickly move out of the cross section of the pumping laser following the ideal gas law [146].

A method for overcoming the Doppler limit is to only select a narrow velocity class of atoms as the ensemble used for quantum memory storage and discard the rest of the atoms, this method is called Velocity Selective optical Pumping (VSP).

Initially the populations are split between the two ground states ( $|g_1\rangle$  and  $|g_2\rangle$ ) and have a Maxwell-Boltzmann distribution of velocities. A high power pump laser is then used to empty one of the ground states ( $|g_1\rangle$  in Figure 3.8) of atoms, followed by a narrow-band pump-back laser used to return a narrow velocity class back into the initial ground state.  $|g_1\rangle$  is then used as the ground state for the memory  $|g\rangle$  and the other ground state  $|g_2\rangle$  is discarded for the purposes of quantum memories.

#### 3.3.1 Velocity selective optical pumping theory

The rate equations for population inversion density can be seen in (Eq 3.1) and (Eq 3.2). These equations can be obtained from a simplified treatment of the optical Bloch equations [147], where only the population terms are tracked, ignoring the coherences, in the limit of the weak fields. The Einstein rate equations are used to model stimulated and spontaneous emission [148]. Where  $n^*$  is the population inversion between the two ground states ( $n^*(v_z) = n_2(v_z) - n_1(v_z)$ ) F = 1 and F = 2 and  $n_{e_J}$  is the population of the excited state [149].

$$\frac{dn^*}{dt} = \mp \left(n_F - \frac{g_F}{g_{e_j}} n_{e_j}\right) \frac{B_{Fe_j}}{c} \int_0^\infty I_k(\omega) g_L\left(\omega - \omega_0 \left[1 + \frac{v_z}{c}\right]\right) d\omega + n_{e_j} (A_{e_j 2} - A_{e_j 1})$$
(3.1)

$$\frac{dn_{e_j}}{dt} = \left(n_F - \frac{g_f}{g_{e_j}}\right) \frac{B_{Fe_j}}{c} \int_0^\infty I_k(\omega) g_L\left(\omega - \omega_0 \left[1 + \frac{v_z}{c}\right]\right) d\omega - n_{e_j} (A_{e_j 2} + A_{e_j 1}) \quad (3.2)$$

In these equations; F = 1,2 refers to the ground states that the population is being sorted between, j = 1,2 are the excited states, k = pump, pump-back are the labels for the individual pump modes with frequency  $\omega$  and spectral intensity I( $\omega$ ).  $g_L$  is the lifetime-broadened lineshape for each velocity class with Doppler shifted resonant frequency  $\omega_0(1+v_z/c)$ ,  $g_j$  is the degeneracy of the  $j^{th}$  quantum state, and  $A_{e_fF}$  and  $B_{Fe_j}$  are the Einstein coefficients for describing the spontaneous decay and stimulated transfer between the ground states (F) to the excited state ( $e_j$ ). Therefore in these equations the first term describes how the population interacts with the lasers and the

second term represents the spontaneous emission from the excited states. This model assumes that there isn't significant movement of the atom outside of the pump region moving into it.

In order to get the spectrum from equations 3.1, 3.2 one must consider a weak scanning probe on the  $D_2$  line with frequency  $\omega$ ;

$$\sigma_{2-F'}(\omega, v_z) = B_{FF'} \frac{\hbar \omega}{c} g_L \left( \omega - \omega_{FF'} (1 + \frac{v_z}{c}) \right)$$
 (3.3)

where F = 1,2, F' = 0,1,2,3,  $B_{FF'}$  are the Einstein coefficients for a given transition,  $g_L$  are the lifetime-broadened line shapes of the transitions and  $\omega_{FF'}$  are the resonant frequencies of the transitions. Therefore the transmission through a region of a Rb cell with radius  $\sigma$  is:

$$-\ln T(W) = L \sum_{F,F'} \int_{-\infty}^{\infty} n_f(v_z) \sigma_{F \to F'}(\omega, v_Z) dv_z$$
 (3.4)

for a cell length L.

#### 3.3.2 VSP experimental results

Once the VSP is created, each of the allowed transitions will have the same velocity class of atoms. Therefore measuring the spectra of  $^{87}$ Rb with a narrow velocity class in the F = 2 ground state will show the allowed transitions, F = 2 - F' = 1,2,3 with their relative transition strengths. This can be seen in Fig 3.9, with the allowed transitions labelled on the figure. A larger optical power of this pump-back lasers leads to more atoms in a given velocity class and therefore a larger optical depth of the VSP features. Fig 3.10 shows different VSP structures at different pump-back powers.

The VSP method for shaping atomic spectra forms the basis for the AFC quantum memory, as modulating the pump-back lasers frequency will capture different velocity classes leading to frequency sidebands for the VSP features in the spectra. This behaviour is what forms the AFC in the atomic spectra. Therefore, understanding the VSP behaviour infers the behaviour of the AFC memory.

#### 3.3.3 Power broadening

When the intensity of the pump-back laser increases beyond the saturation value of the transition the excitation line width increases in proportion to the field amplitude, this saturation intensity is  $3.05 \text{mW}/\text{cm}^2$  [142]. This means that the AFC/VSP tooth width ( $\gamma$  from Eq 2.2 and Fig 2.2) depends on the pump-back power and the dependence can be extracted from a rate equation treatment and is shown to have a

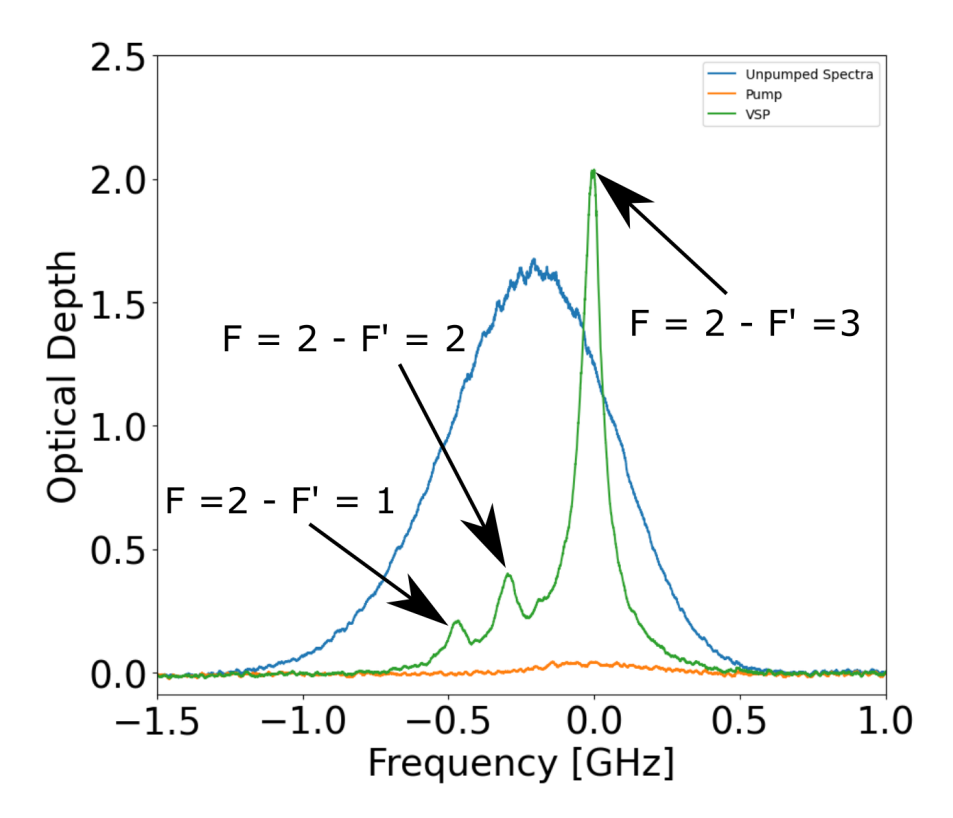


FIGURE 3.9: VSP with labelled transitions (see Fig 3.1)

square root dependence with spectral energy density [150]. Understanding this dependence is critical for finding the optimal conditions for the AFC protocol.

To investigate how the VSP spectra changes with pump-back power the VSP features were recorded at different pump-back powers. This experiment follows the same experimental setup as future chapters (see Fig 3.3 for more details on the experimental setup), the pump is kept at the same power to empty the F=2 ground state while the pump-back power is changed using a half wave plate (HWP) to change the amount of power pumping the atoms to create the VSP or AFC structures. Fig 3.10 shows how the VSP structure changes with different pump-back powers. The optical depth depends on this pump-back power because more atoms are returned into the F=2 ground state. The effect that the pump-back power has on the width can also be seen here. In both of the plots in Fig 3.11, the error bars are smaller than the data points and therefore are not viable on the plot.

Fig 3.11a shows how the optical depth of the strongest VSP transition changes with pump-back power, this is a linear relationship as more optical pump-back power means that there are more photons for the atoms in the F=1 state to absorb and change to the F=2 ground state, therefore increasing the optical depth of the VSP features.

One can extract the width by fitting a Lorentzian function to these features, Fig 3.11b shows how this width changes with pump-back power. It is clear that power

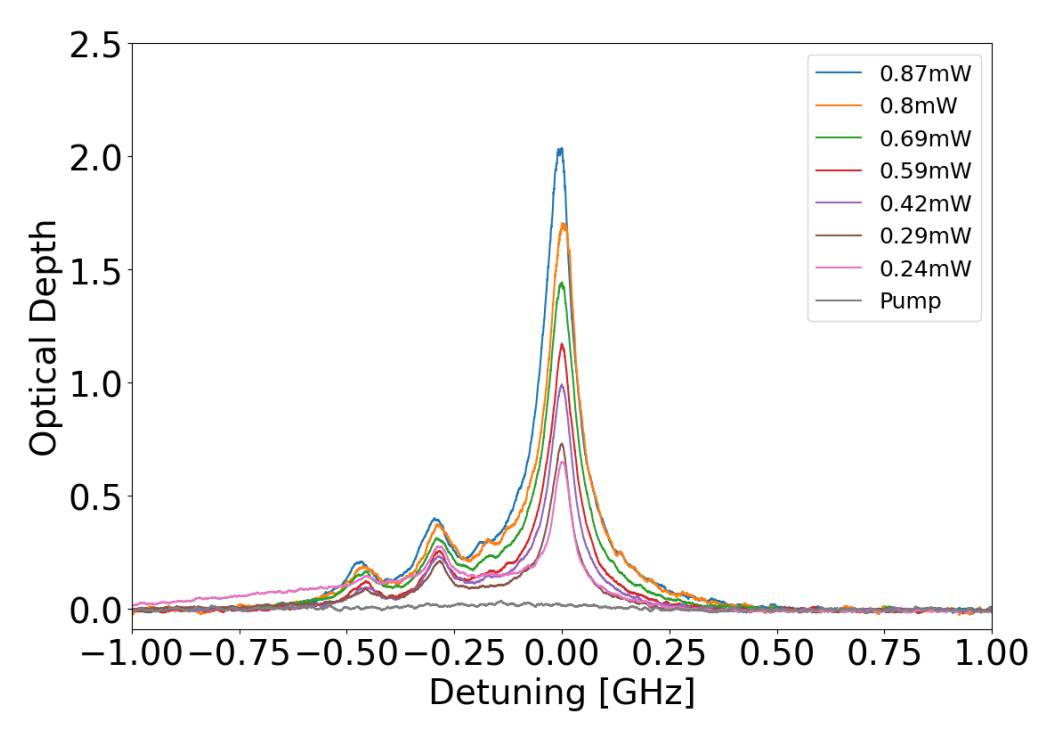


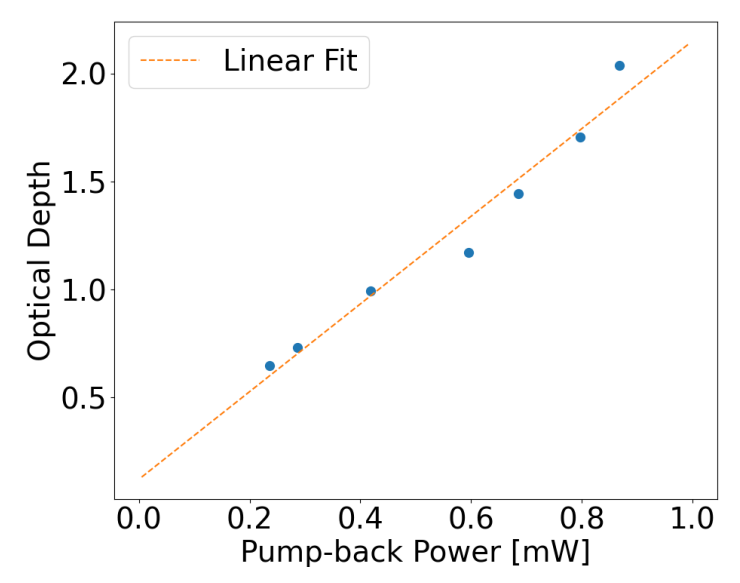
FIGURE 3.10: vsp power broadening demonstration

broadening has a large effect on the VSP width, this will be the same relationship for the AFC features, and therefore the efficiency of the memory. This is a phenomenological fit, as it does not follow the predicted relationship state earlier. Therefore, this fit is used to estimate the broadening for a given power and is only valid for the powers tested.

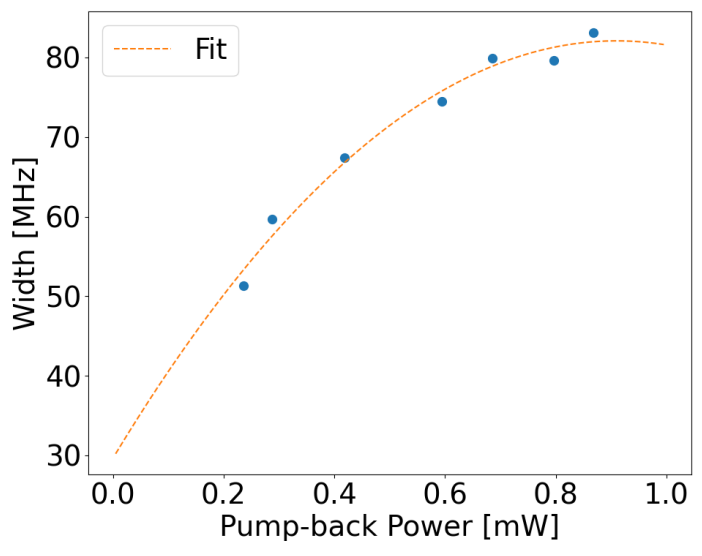
Using these widths on the VSP features, one can calculate the dephasing time for this collection of atoms, using the relation [151]:

$$T_{dephasing} \propto \frac{1}{\gamma}$$
 (3.5)

This can be seen in Fig3.12, where the red dotted line is the dephasing time for a natural 667MHz (taken from results) wide normal distribution of the atoms in the F = 2 ground state before any optical pumping occurs. The blue line are the widths taken from Fig 3.11b. This is the blue line in this figure. As can be seen the dephasing time decreases with pump-back power and therefore the width of these features.



(A) Pump-back Power vs Optical Depth of the F = 2 - F' = 3 transition, the power of the pump-back laser and optical depth is a linear relationship which can be explained intuitively - more photons in the pump-back laser, the more atoms get optically pumped back into this ground state.



(B) Pump-back Power vs Width of the F = 2 - F' = 3 transition, with a phenomenological fit.

FIGURE 3.11: Pump-back power dependence

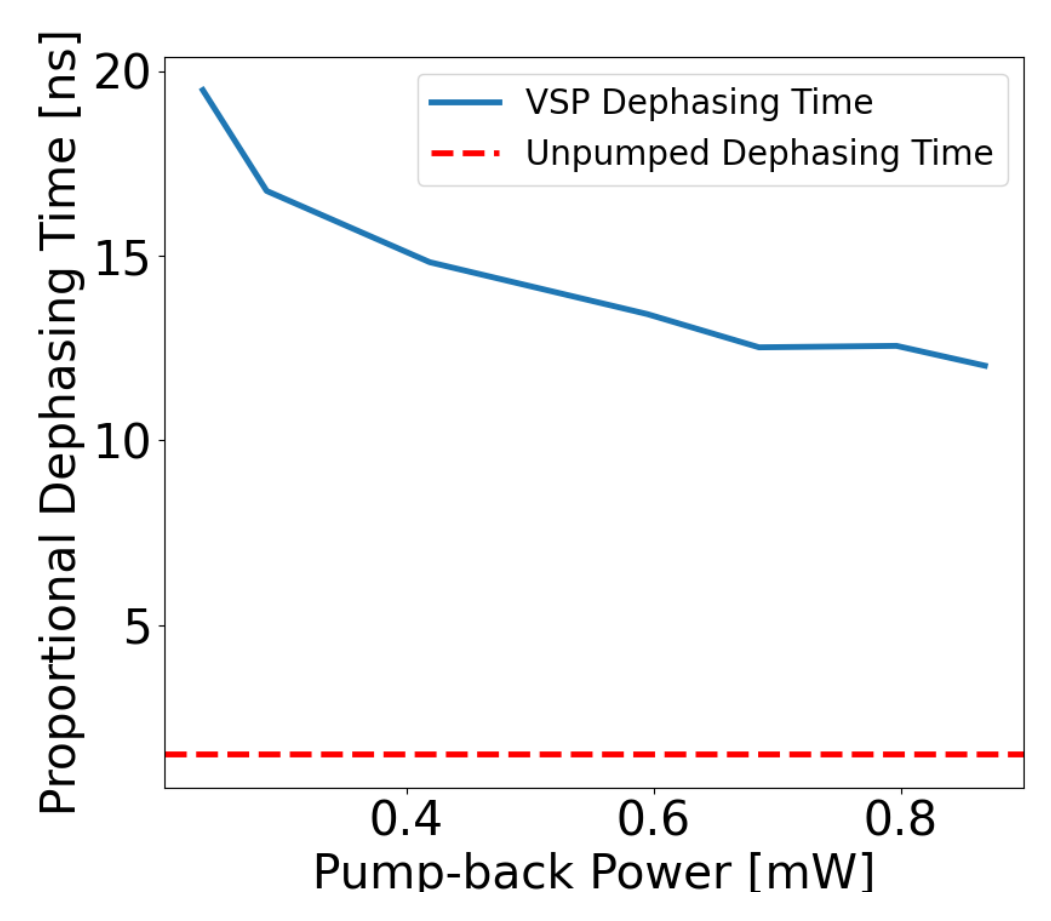


FIGURE 3.12: VSP Dephasing Time. These dephasing time is the reciprocal of the widths measured in Fig 3.11, compared to the dephasing time of the unpumped ground state (red dotted line).

# 3.4 Applications of VSP

This section discusses using the VSP method to improve the Off Resonant Cascaded Absorption (ORCA) protocol in <sup>87</sup>Rb, this section will describe a paper that I co-authored ([1]). This experiment was carried out in collaboration with Imperial College London (ICL) and investigates the warm vapour <sup>87</sup>Rb ORCA quantum memory with a telecom signal. This experiment was performed with the Photonic Quantum Information group at ICL led by Professor Ian Walmsley. HQNL provided a 780nm laser to scan the spectrum of the Rb cell at ICL as well as some code written to extract the temperature of the cell, I was present for the main data collection of experiment.

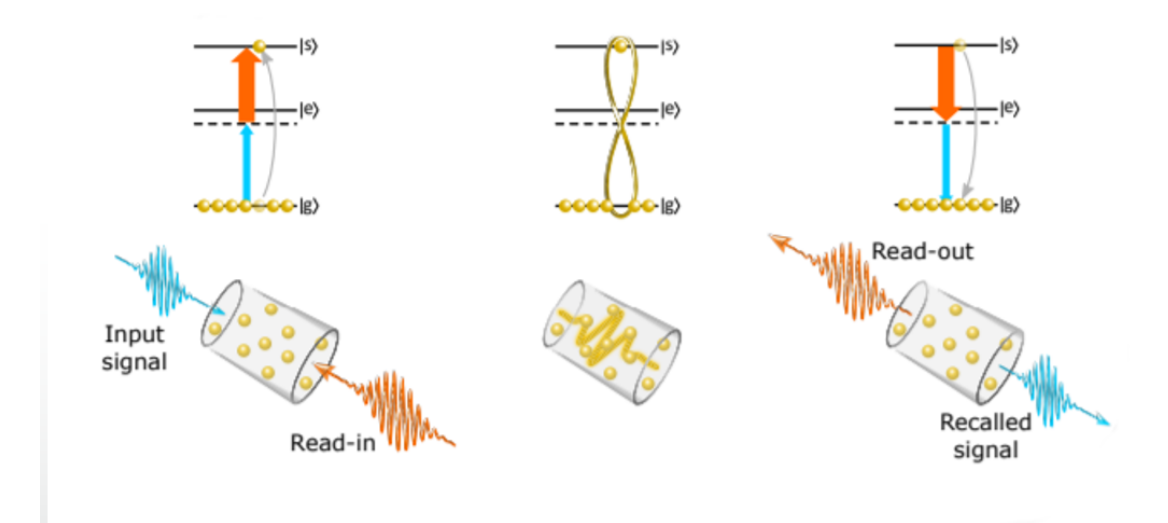


FIGURE 3.13: Illustration of the ORCA storage and retrieval process in a ladder configuration. The left shows how the memory is initialised with a strong control pulse and a weak signal to create the coherence seen in the middle, a second control pulse is used to recall the signal. This diagram is taken from [152].

#### 3.4.1 Introduction

The Off Resonant Cascaded Absorption (ORCA) protocol is an optically controlled inherently noise free protocol that utilises a doubly excited state as a storage state, in a three-level cascade configuration (see Figure 3.13). This configuration ensures that the storage state is empty, due to it being an excited state it has no population initially within it, and therefore the protocol requires no preparation before a coherence can be formed.

A coherence between the ground  $|g\rangle$  and storage states  $|s\rangle$  is established using a strong control and a weak signal field in a counter-propagating configuration. The counter-propagating nature of these fields allow for a reduced momentum mismatch on a given atom caused from interacting with these fields. Experimentally, counter-propagating fields are easier to separate to reduce the control leakage on the signal detection.

The overall ORCA process is resonant with the two photon  $|g\rangle$  -  $|s\rangle$  transition, but the individual control and signal fields are off-resonant with the intermediate excited state  $|e\rangle$ . This off-resonance allows for a broadband control pulse to be used , as well as preventing the atoms absorbing into the intermediate excited state which would then undergo spontaneous emission. In order to retrieve the signal, the control pulse is turned off in order to break the coherence and re-emit the input signal. In order to reset the ORCA protocol, one simply has to wait the excited state lifetime (90ns) for the storage state to completely empty again.

The major advantage of the ORCA protocol its inherently noise free nature. This feature originates from the fact that the storage state is initially empty therefore only

the required atom is put into a coherence between  $|g\rangle$  and  $|s\rangle$  and no other excitations are present to produce noise, although four wave mixing within the energy levels can still lead to noise. As the signal and control are different wavelengths the control itself cannot do two-photon transfer of atoms to the excited state, it would need to be 3 photons or more.

Currently, ORCA has been demonstrated with in a warm Caesium gas with an efficiency of 16.77%, a storage time of 3.5ns, bandwidth of 1GHz and a noise per trial of  $3.8 \cdot 10^{-4}$  [152] - this noise per trail is orders of magnitude better than the other optically controlled protocols.

This protocol has also been demonstrated with weak coherent pulses in room temperature Cs with an average photon number per pulse  $\mu = 0.06$  [153]. For a 1/e storage time of 32ns they measured an efficiency of 15% with a high signal-to-noise ratio of 830:1.

#### 3.4.2 Experimental setup

Fig 3.14 shows the ORCA level scheme (Left) used in the experiment, where a 780nm control and a 1529nm signal are used to create this ladder memory, these energy levels are discussed earlier in this chapter. Where the right side of this figure shows the experimental setup for the memory. The signal (1529nm) goes through an EOM in order to create short pulses of light with a 300ps duration that are the attenuated to the single photon level ( $\mu = 0.084$ ), this goes through the cell with dichroic mirrors (DM,DMLP735B) either side to transmit the 1529nm light and reflect the 780nm control light before reaching the Superconducting Nanowire Single Photon Detectors (SNSPDs). This pathway also includes a set of longpass filters - FGL1000S to block any of the control laser leaking through the experiment. The control laser is a Titanium Sapphire laser (Spectra Physics Tsunami) at a repetition rate of 80 MHz that goes through an unbalanced Mach-Zehnder interferometer (UMZI) to precisely set the time difference between the first and second control pulses and therefore tune the storage time of the protocol. As mentioned before, this control is counter propagating the signal in order to reduce the momentum difference on the atoms and greatly reduce the amount of control light leaking onto the SNSPDs. The control laser has its power monitored to keep consistency throughout the experiment.

This cell is 80mm in length and is heated to a temperature of  $120^{\circ}C$  in order to have a large optical depth of the ensemble.

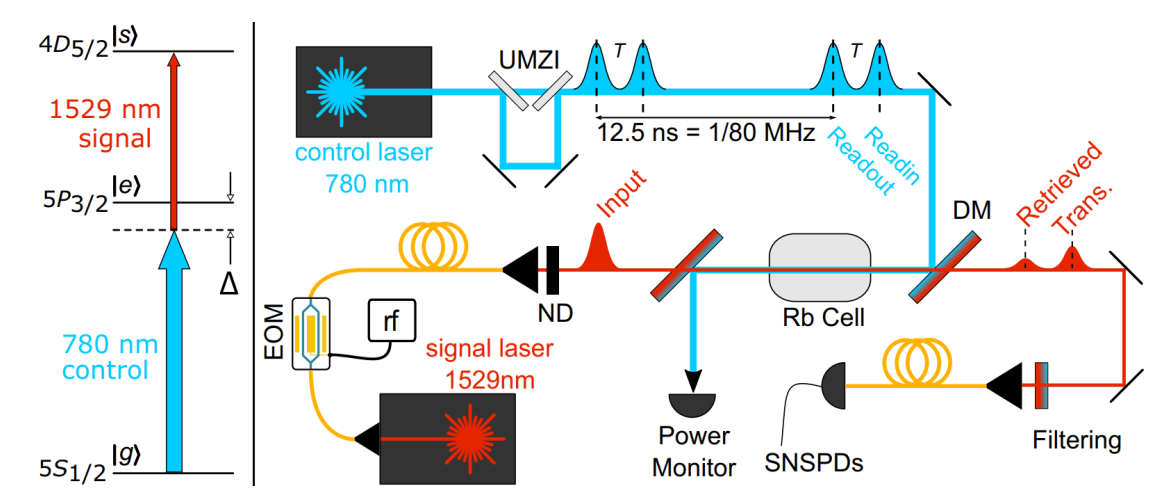


Figure 3.14: Telecom ORCA level diagram and experimental setup. The left shows the energy level scheme for implementing the protocol where  $\Delta=6 GHz$ . The right part of the figure is the experimental setup; where DM - dichroic mirror, ND - neutral density filters, EOM - Electro-optic modulator, RF - arbitrary waveform generator, SNSPD - superconducting nanowire single-photon detectors and UMZI - unbalanced Mach–Zehnder interferometer. This figure is taken from [1].

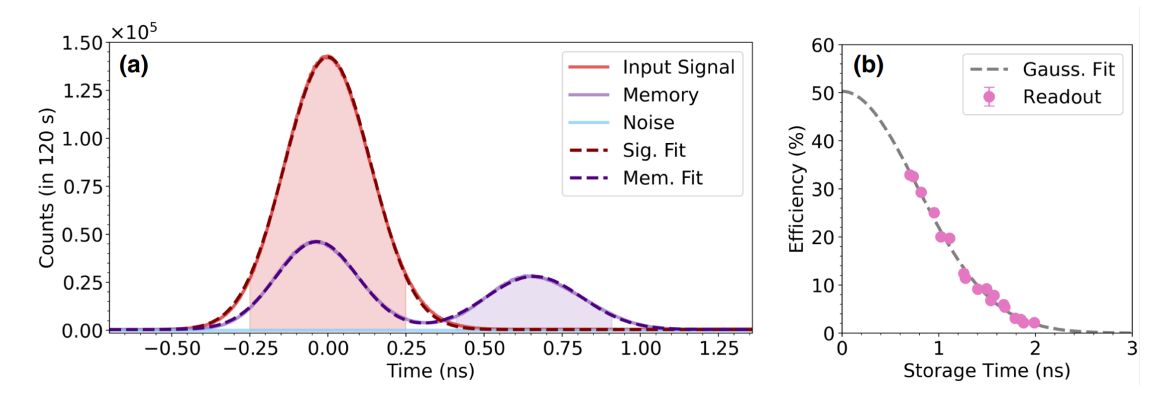


FIGURE 3.15: ORCA Results. (a) The red dotted line is the fitted input pulse, the purple is the fitted recalled pulse. The red (purple) areas are used to calculate the efficiency of the protocol, each data set has an integration time of 120s. (b) Read-out efficiency vs storage time, the grey dotted line is a Gaussian fit to the data (pink circles), for this data the integration time is 10s per point with the same integration window as (a). This figure is taken from [1].

#### 3.4.3 Results

The results can be seen in Fig 3.15 (taken from [1]), this experiment was performed with a mean photon per pulse of  $\mu = 0.084$ . The two control pulses had a separation of 660ps (and therefore a memory storage time of 660ps) which lead to a total efficiency of  $\eta_{tot} = 20.90\%$  and a read-in efficiency of  $\eta_{read-in} = 69.13\%$ . If we include the transmission efficiency of light through the experiment is  $\eta_{trans} = 56\%$  and the detector efficiency  $\eta_{det} = 80\%$  gives an overall end-to-end efficiency  $\eta_{e2e} = 9.4\%$ .

The storage time of the memory was changed in order to find the characteristic lifetime of the memory based on the readout efficiency (the area of the recalled pulse

compared to the amount of light read into the memory). This experiment gave a characteristic lifetime of 1.10ns for the ORCA protocol, this was calculated using a Gaussian fit on the readout data. This storage time is short as it is limited by the Doppler dephasing of the protocol; as the ground state has as Doppler broadened line-width of 585MHz leading to a dephasing time consistent with the time measured suggesting that this is the limiting factor for the storage time of the memory. The signal to noise ratio (SNR) for an input photon number  $\mu = 0.084$  was measured to be  $1.9x10^{-4}$  which can yield a fidelity with a maximum value of nearly 1. This is calculated using the equation, F = (SNR + 1) / (SNR + 2) which assumes a true single photon input [154].

#### 3.4.4 Conclusion

As ORCA has now been demonstrated with single photon level telecom inputs the next step is to introduce this protocol with a true single photon source, this was done with a MOVPE-grown InAs QD emitting at 1529.3 nm with GHz bandwidth [155]. A total efficiency of  $12 \pm 0.4\%$  for a storage time of 800ps and a signal to noise ratio of  $18.2 \pm 0.6$ .

As mentioned before the main factor limiting the storage time of this protocol is the Doppler lifetime of the inhomogenoulsy broadened transition used, therefore if one was to use VSP to reduce the spread of velocities the storage time can be pushed up to the excited state lifetime of the telecom transition (90ns) which is the ultimate upper bound of the memory. For example if a width of 51.31MHz (from Fig 3.11b) then the storage time is limited to 19.48ns. The issue with this approach is that VSP reduces the number of atoms in the ground state used for the ORCA protocol which will reduce the absorption of the signal and therefore reduce the total efficiency of the protocol. Another approach to overcome this issue is to combine the ORCA protocol with the AFC protocol [156].

## 3.5 Summary

This chapter has provided information on how to experimentally realise this quantum memory protocol in warm <sup>87</sup>Rb vapour, along with some initial characterisation experiments to help further understand the mechanics at play for creating the AFC structure. This laid all the groundwork for the following chapters to demonstrate and characterise the AFC memory protocol, to find the ideal operating conditions and compatibility with single photon level inputs which is a key step in using this protocol for larger and more complex quantum applications. This chapter has also used the

experimental realisation experiments to justify a potential method for improving the ORCA protocol applied to the same memory platform.

# Chapter 4

# Warm Vapour AFC Experiment

This chapter is split into two main sections covering two different experimental regimes: the continuous wave (CW) and the pulsed regimes. Both contain results aiming to fully characterise the memory and find the optimal experimental conditions to achieve maximum efficiency in storing and retrieving light. Avenues for investigations include the initial demonstration of AFC storage, the dependence of this efficiency on the temperature (and hence the number density) of the atoms and the detuning of the input signal. Whereas the pulsed regime resolves some of the issues found during the CW investigation, as well as finding the lifetime of the AFC structure, this is how long the AFC structure survives before the atoms repopulate the ground states.

#### 4.1 CW Results

The CW regime is the case where the pump and pump-back lasers are always on for the entire experimental procedure, even when the signal is introduced. While the pumping lasers would deplete the excited state coherence during the storage, the rate of this is much slower than the storage times of the AFC, so the AFC echos are still observable. This is the technically simplest approach to characterise the AFC performance. Section 4.2 presents results where the pumps are off when the signal is introduced. Fig 4.1 shows the simplified setup for the CW experiments; this diagram doesn't include the actual path of the laser around the optical table, unlike Fig 3.3, and the fibres, the TA, reference cell and additional optics are removed for a more straightforward interpretation. As this is the CW experiment, the AOMs are also removed from the diagram; in reality, these are still present on the table but are 'on' for almost the whole experimental run.

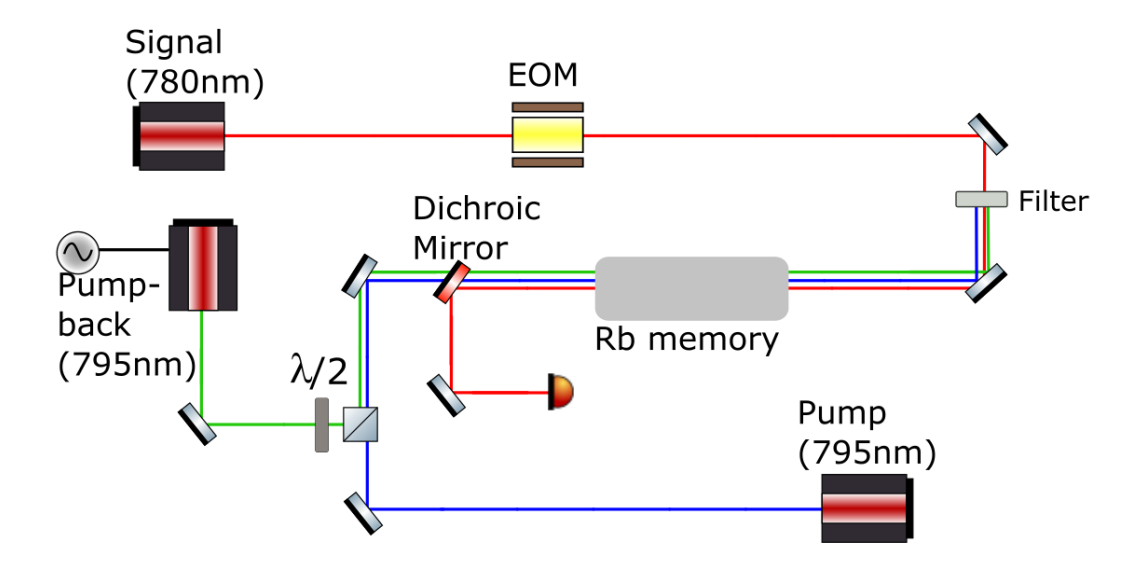


FIGURE 4.1: Simplified CW Experimental Diagram. Where, EOM - Electro-optic modulator,  $\lambda/2$  - half wave plate, and the filters stop the pump and pump-back light from coupling into the EOM.

To create the AFC structure in the CW regime in a heated cell the pump had a power of 80 mW and a pump-back power of 1.4 mW was used along with a modulation frequency of 66.667 MHz; this frequency was produced from an AWG along with a multiplexer (ZX90-2-13-S+) and a high pass filter (ZX75HP-73-S+) to make a 133 MHz modulation on the frequency of the pump-back laser. This created the AFC structure in Fig 4.2 on the F = 2 ground state.

In this figure, the cyan trace is the natural ground state population distribution of the F=2 state at this given temperature (35 °C), the purple trace is the VSP features (i.e. the pump-back laser without frequency modulation), this trace shows the allowed transitions from the F=2 ground state. The most prominent purple peak is the F=2 - F'=3 transition, the next one to the left is the F=2 - F'=2 transition, and the final peak is the F=2 - F'=1 transition. The dark blue trace is the AFC structure that is created when the pump-back laser is modulated, these extra peaks are created by the sidebands of the purple trace overlapping. This happens when the modulation of the pump-back laser is equal to the excited state separation of the allowed transitions, see Fig 3.1. For this AFC the pump-back modulation is 133MHz, which is the separation between the F'=2 and the F'=3 excited states. The acceptance bandwidth of this AFC is shown by the dotted blue line; this bandwidth is 0.682GHz.

Fig 4.3 shows the storage and retrieval of light using the AFC Quantum Memory with an input pulse bandwidth of 200MHz (5ns); the blue curve is input light for the memory and is recorded when the pump-back laser is physically blocked so no AFC is made on the atoms. Once this laser is unblocked, the Orange trace is recorded. The

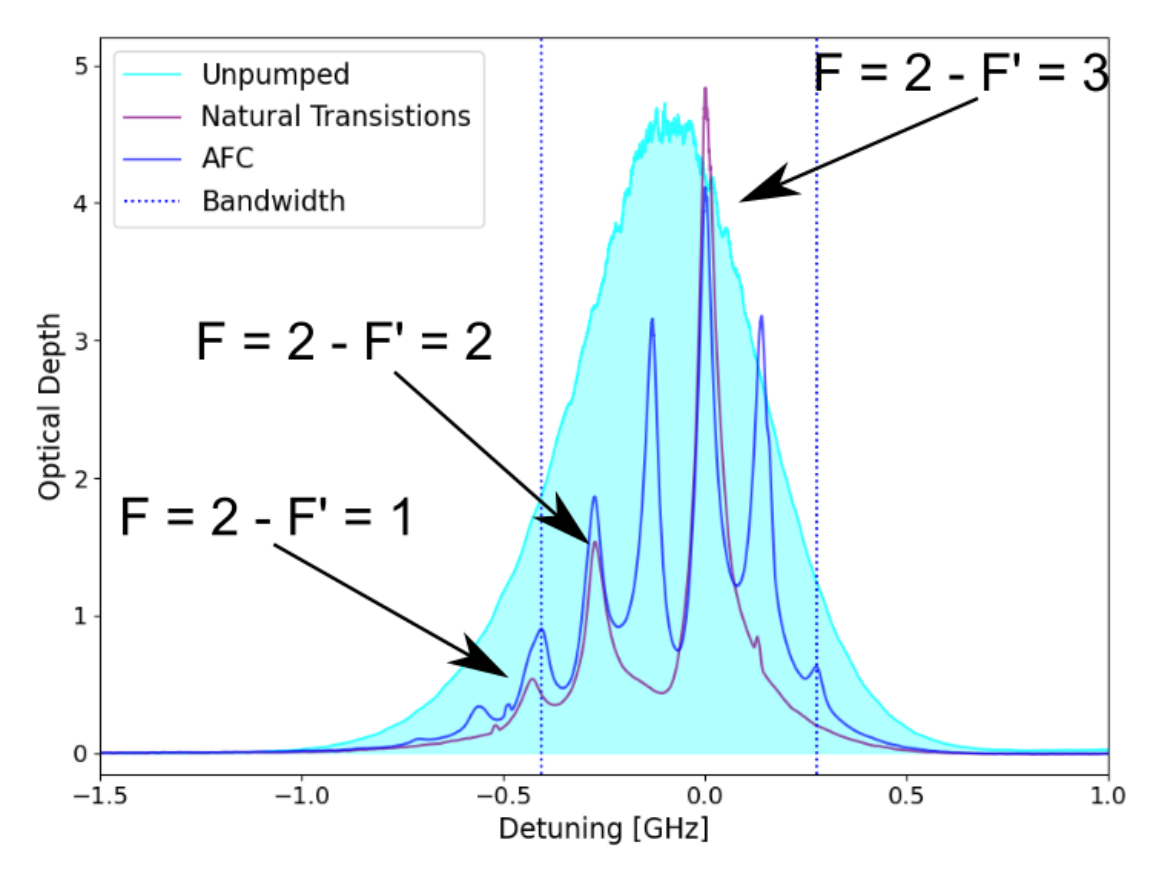


FIGURE 4.2: CW AFC Spectrum. The AFC acceptance bandwidth is shown by the blue dotted lines, this is an area of 0.682GHz.

total efficiency of this storage and retrieval process is 9.04%, and the read-in efficiency is 59.1%.

The read-in efficiency is calculated by integrating the transmitted Orange pulse over the integration window (Red region) and comparing it to the integrated blue pulse over the same window (Blue area); this window is 4ns wide, and this window size is chosen to capture as much of the input and recalled pulse as possible. The total efficiency is calculated by integrating the recalled pulse over the same width of the window as before, centred in the middle of the recalled pulse. These are represented by Eq 4.1 and Eq 4.2, where the values are expressed as percentages.

$$\eta_{readin} = \left(1 - \frac{\Sigma transmitted}{\Sigma input}\right) \cdot 100 \tag{4.1}$$

$$\eta_{total} = \frac{\Sigma recall}{\Sigma input} \cdot 100 \tag{4.2}$$

In Fig 4.3 both the input and AFC pulses have negative values after the pulse, this is due to the response time of the detector (Menlo APD210) being close to the timescale

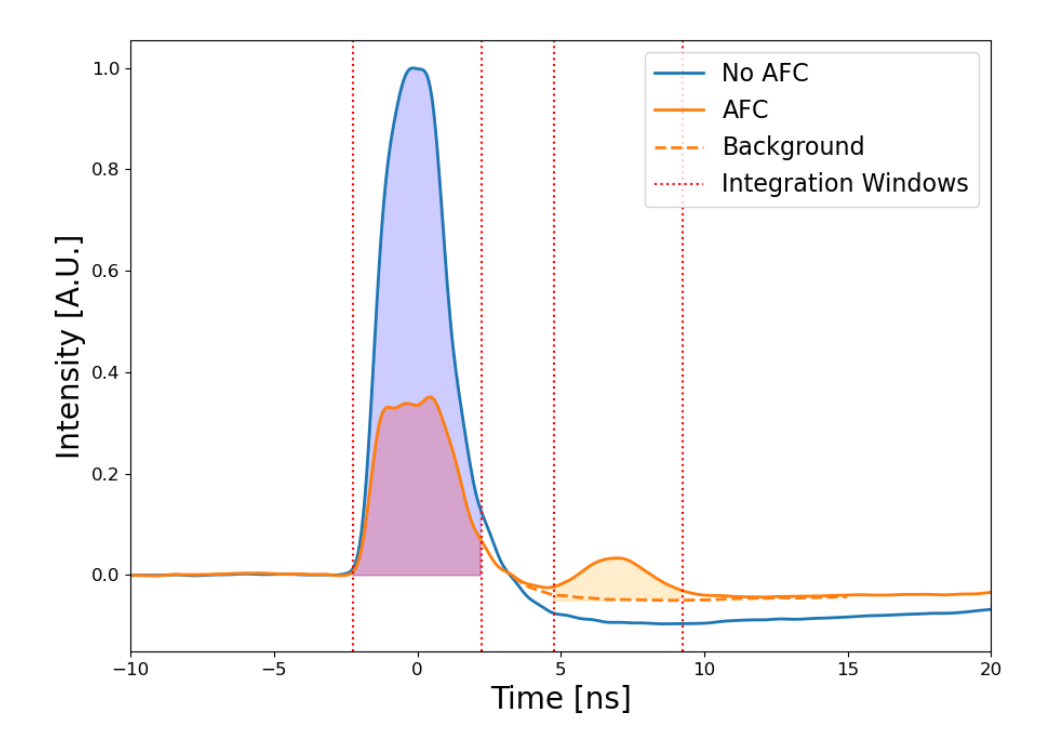


FIGURE 4.3: CW AFC Storage. The coloured regions and the integration windows are used to determine the efficiency of the memory, Blue is the input pulse, Red is the transmitted pulse and Orange is the recalled pulse.

of the storage and retrieval process and therefore over-shooting the voltage output of said detector. This adds difficulty to calculating the efficiency of the interaction.

Therefore a new zero line needs to be added to the recall pulse. This was done by finding the difference in height of the traces of the input and recall many nanoseconds after the recall pulse has been observed, and multiplying the input trace by this difference to get the dotted orange line as the new zero of the pulse. This is then used in the efficiency calculations described before.

Using Eq 2.2 we can calculate the predicted efficiency based on fitting a Lorentzian to the main AFC peak in Fig 4.2, doing this gives a predicted total efficiency of 6.08%. This value is less than the one measured from Fig 4.3, this could be due to the assumptions of Eq 2.2 (as discussed in Chapter 2). Alternatively, the fitting to the recall pulse that was required to measure the efficiency in Fig 4.3 could also lead to a misleading total efficiency.

#### 4.1.1 Temperature dependence

Higher cell temperature means more atoms in the vapour phase and therefore a higher optical depth [142], looking at the vapour-pressure model:

$$\log_{10} P_v = -94.04826 - \frac{1961.258}{T} - 0.03771687 T + 42.57526 \log_{10} T$$
 (4.3)

$$\log_{10} P_v = 15.88253 - \frac{4529.635}{T} + 0.00058663 \ T - 2.99138 \log_{10} T \tag{4.4}$$

Where Eq 4.3 is the equation for the solid phase and Eq 4.4 is the equation for the liquid phase, and  $P_v$  is the vapour pressure in Torr and T is the temperature in Kelvin.

Referring back to Chapter 2, Eq. 2.2 indicates that the total efficiency will be greater due to this larger atom number.

The cell is heated using insulated quad twist wire from lakeshore cryogenics (Quad-Twist WQT). The wire comprises two twisted pairs, each pair is 3.15 twists per cm and the two pairs are entwined at 1.57 twists per cm. The four wires are soldered such that the current meanders back and forth the length of the wire i.e. the output ends of wires 1 and 2, 3 and 4 are soldered, and the input ends of 2 and 3 are soldered, with current introduced into the input of wire 1 and coming out the input of wire 4. This configuration ensures that any induced magnetic field from one wire is cancelled out by the field induced by the paired wire. Minimizing these fields is critical to not induce unwanted Zeeman shifts on the atoms, which can cause a shift of 10s of MHz per voltage of the wire.

Increasing the voltage supplied to the wire wrapping the cell increases the temperature of the wire and heats up the cell (this is known as Joule heating [157]), this converts more atoms into the vapour phase from the solid phase therefore increasing the optical depth of the ensemble. This can be seen in Fig 4.4. Where Fig 4.4a is the voltage supplied to the heating wire vs the temperature measured by a temperature probe placed within these wires, the heating of the wire is a linear relationship with voltage supplied [157] which doesn't fit to the first point (with no heating voltage) representing the temperature of room at the cells position (the measured temperature of the lab is 19°C which is below the temperature measured in the cell due to a number of laser heads and other electronic equipment on the optical table rasing the temperature to around 20°C). Fig 4.4b is the heating voltage vs a temperature fitted to the ground states in the spectrum, this is also a linear relationship [157], the first point on this plot shows agreement with the temperature of the room. Fig 4.4c is the heating voltage vs the number of atoms in the ensemble, this shows how the optical depth of the AFC features will change with cell temperature.

There is a temperature probe (Fig 4.4a) inserted into the wire wrapping of the<sup>87</sup>Rb cell that measures the temperature of the cell wall, the fitted temperature (Fig 4.4b) takes the Doppler width of the ground state population and compares this to structure of <sup>87</sup>Rb and information provided in [142] to extract a temperature from this width,

similarly the atom number temperature (Fig 4.4c) to measure the optical depth of these ground states to extract the temperature based off Eq 4.3, 4.4.

#### 4.1.1.1 Temperature dependence results

The signals frequency was resonant with the tooth with the largest optical depth, this tooth is the one created from the modulation side bands from the F = 2 - F' = 3 and the F = 2 - F' = 2 transitions.

Fig 4.5 shows how the total efficiency of the AFC storage changes with temperature. The total efficiency peaks at 35°C. The shape of this dependence matches with the AFC simulations (Fig 2.3) performed in Chapter 2, where the efficiency rolls over when one increases the optical depth of the ensemble.

All of these AFC structures were created with the same Pump and Pump-back powers, these powers were: Pump power =  $1.82 \pm 4.07$ mW and Pump-back power =  $1.11 \pm 6.94 \cdot 10^{-4}$ mW. These powers were kept fixed for ease of data acquisition.

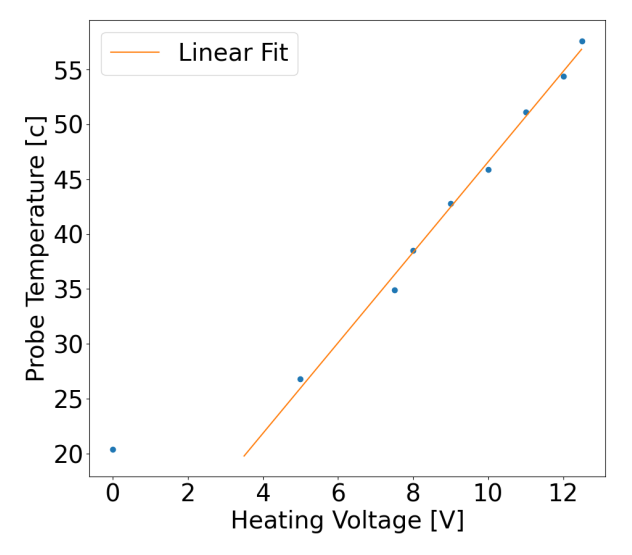
The issue with a higher temperature is there is a broader ground state with a larger OD making optical pumping less efficient, this is because the pump is a narrow band laser therefore pumping the ground state relies on power broadening and a larger optical depth of the ground state means more atoms detuned from the frequency of the laser.

#### 4.1.2 Detuning dependence

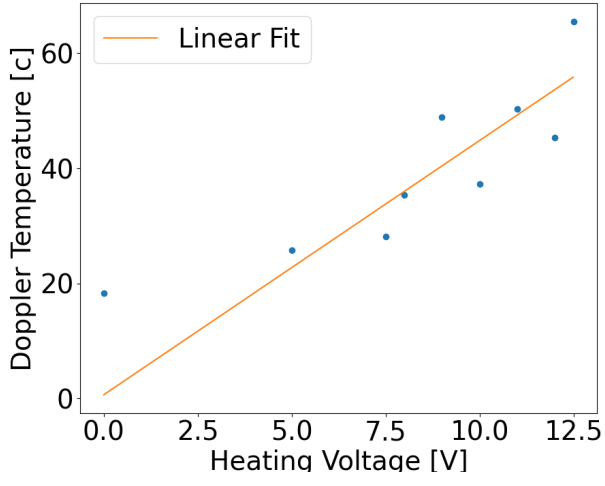
It is clear that when the signal is resonant with an AFC tooth there is efficient storage and retrieval of light, but if the signal is detuned between two teeth then the recalled signal disappears without much effect on the read-in efficiency, this can be seen in Fig 4.6.

It is believed that the cause of this effect is due to an AFC structure existing on each of the allowed transitions (F=2 - F'=3 and the F=2 - F'=2), due to the pump-back laser modulation causing a large number of additional peaks for each of the transitions. These two effective AFCs give rise to constructive and destructive interference dependent on the relative detuning of the input spectrum to the AFC structure. This means that when the signal is resonant with the main AFC peak (detuning  $\Delta=0$ ) there is constructive interference between these different AFCs, when the detuning is changed to  $\pm\Delta/2$  there is destructive interference cancelling out the recalled pulse.

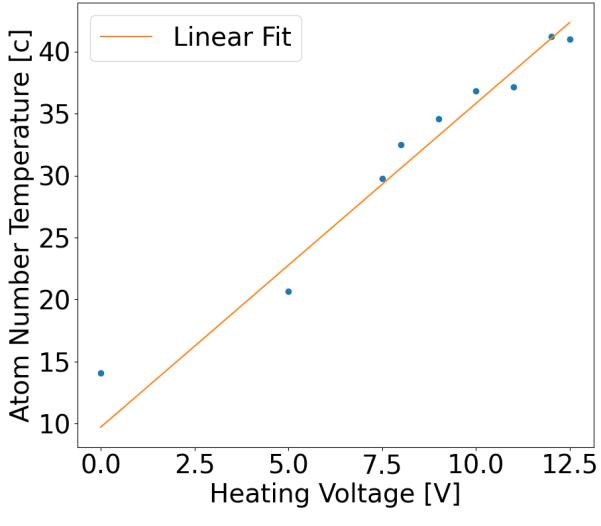
If we consider the field equation relation between the input light field  $E_{in}$  and output light field  $E_{out}$  for the light interacting with the AFC memory and define  $\Delta_0$  as the signal detuning from the centre AFC peak, see Eq 4.5 [89]:



(A) Heating voltage vs probe temperature



(B) Heating voltage vs Doppler temperature.



(C) Heating voltage vs number of atoms

FIGURE 4.4: Cell heating voltage dependence - there are error bars present in these plots but they are smaller than the data points and therefore cannot be seen.

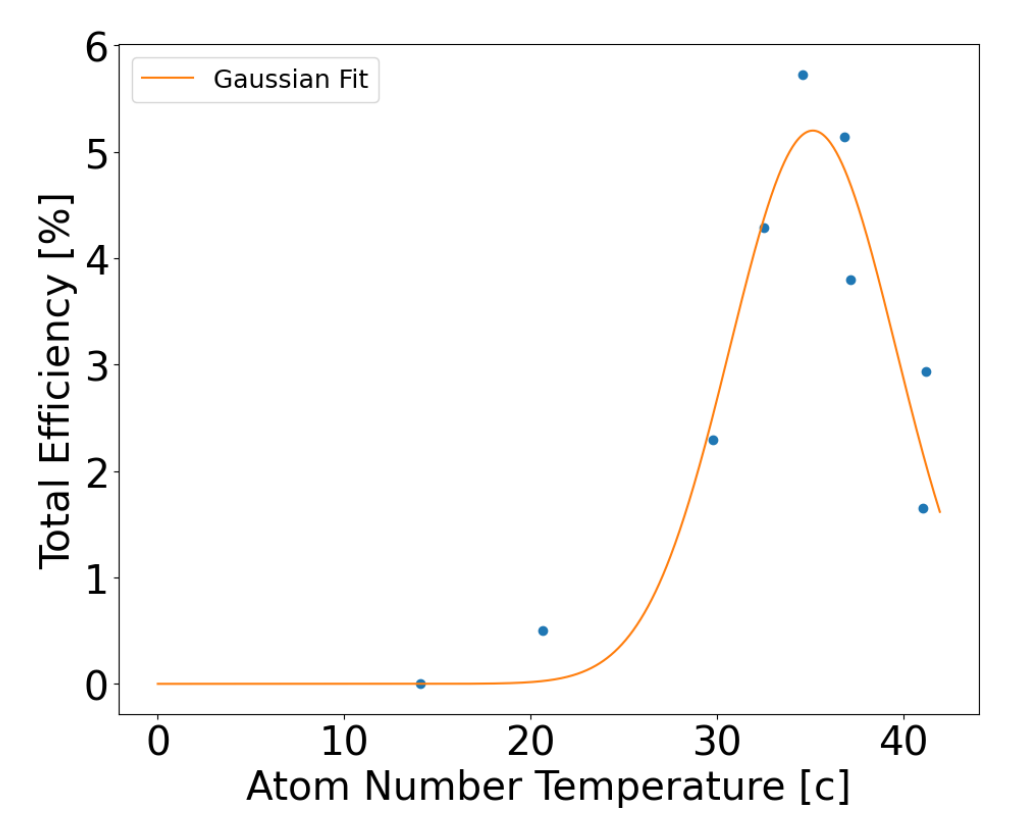


FIGURE 4.5: Atom Number Temperature vs Total Efficiency. The data points in this figure have error bars that are smaller than the data points and are therefore not visible.

$$E_{out} = E_{in}e^{-i2\pi\frac{\Delta_0}{\Delta}}\tilde{d}e^{-\tilde{d}}e^{-\frac{1}{F^2}\frac{\pi^2}{4ln^2}}$$
(4.5)

the first term of this equation is the global phase shift, the second term is the input and output field coupling and the final term is the dephasing due to the finite peak width. This equation was taken from the initial theory paper for the AFC memory first proposed in 2009 [89].

Referring back to the atomic spectral distribution (Eq 2.4) and if one introduces the detuning from the centre AFC peak  $\Delta_0$  such that  $n(\delta) \rightarrow n(\delta - \Delta_0)$ , we get:

$$n(\delta) \propto e^{-(\delta - \Delta_0)^2 / 2\Gamma^2} \sum_{j = -\infty}^{\infty} e^{-(\delta - \Delta_0 - j\Delta)^2 / (2\tilde{\gamma}^2)}$$
(4.6)

if we take the Fourier transform of Eq 4.6 we get:

$$\tilde{n}(t) \propto e^{-t\tilde{\gamma}^2/2} e^{i\Delta_0 t} \sum_{j=-\infty}^{\infty} e^{-(t-2\pi j/\Delta)^2 \Gamma^2/2} e^{i2\pi \frac{\Delta_0}{\Delta}}$$
(4.7)

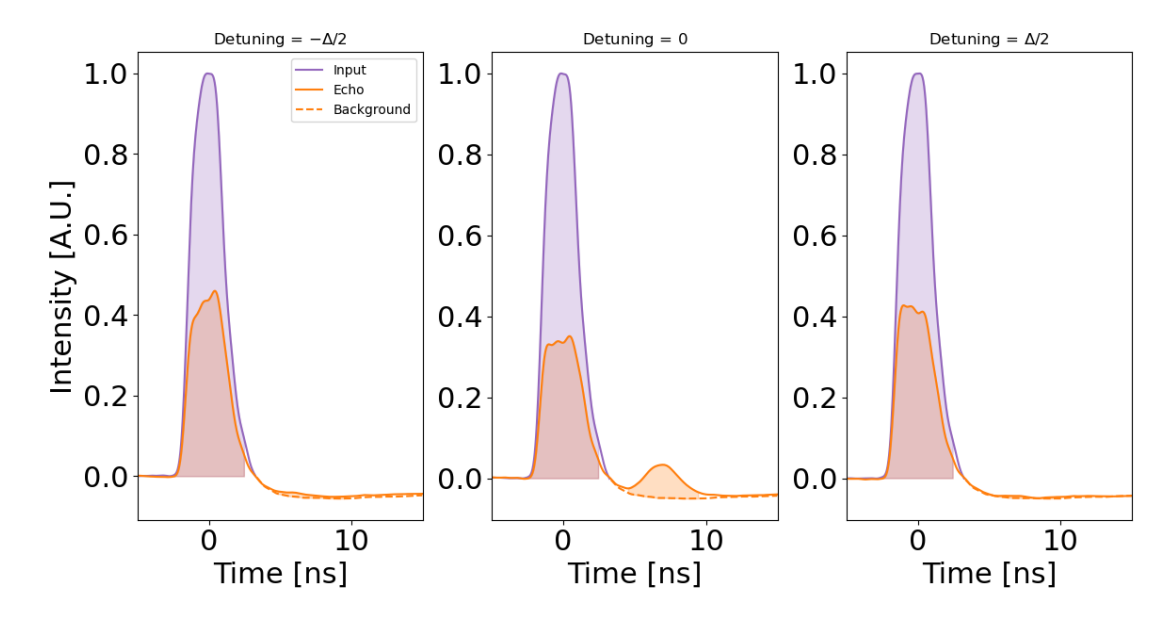


FIGURE 4.6: AFC memory comparison of different signal detuning. The middle plot is resonant with the largest AFC tooth, whereas the left and right plots are detuned to in-between two teeth.

in this equation  $e^{i\Delta_0 t}$  is the general phase and  $e^{i2\pi\frac{\Delta_0}{\Delta}}$  is the phase of the re-emitted light.

When  $\Delta_0 = \Delta/2$ , the reemitted phase becomes  $e^{i\pi}$  which, according to Euler's identity, is equal to -1 corresponding to destructive interference and removing the recalled pulse. whereas  $\Delta_0 = \Delta$ ,  $e^0 = 1$  corresponds to constructive interference. This behaviour is demonstrated in Fig 4.6, this figure shows the signal resonant with an AFC tooth defined with a detuning of zero, with a total efficiency of 9.04% and a read-in efficiency of 59.1%. As the signal is shifted by half the comb separation ( $\Delta$ ) with a detuning of 66.667MHz, the total and recall efficiency is reduced to 1.15% and 49.73% for - $\Delta/2$  0.48% and 51.69%. The read-in efficiency changes due to the total OD of the atoms resonant with the input light, see Fig 4.6.

This observed effect allows for the recreation of the AFC structure when the total efficiency is plotted against the detuning of the signal pulse from the most optically deep AFC tooth. This can be seen in Fig 4.7. As the signal is further detuned from the centre of the AFC less of the pulse in frequency space is resonant with the atoms and therefore the read-in efficiency is lower.

Interestingly, one can see the frequency of the pump laser, as this laser is on the atoms all time (continuous wave) it is constantly pumping the population especially at the centre point of the laser, this point is at a detuning value of 0.286GHz. This creates a transparency window (like the EIT memory scheme discussed in Chapter 1) causing a lower read-in efficiency, due to a lower population at that frequency, and subsequently a lower total efficiency. The echo efficiency also dips below zero due to the fitting on the recall pulse, this does not imply a negative region of light.

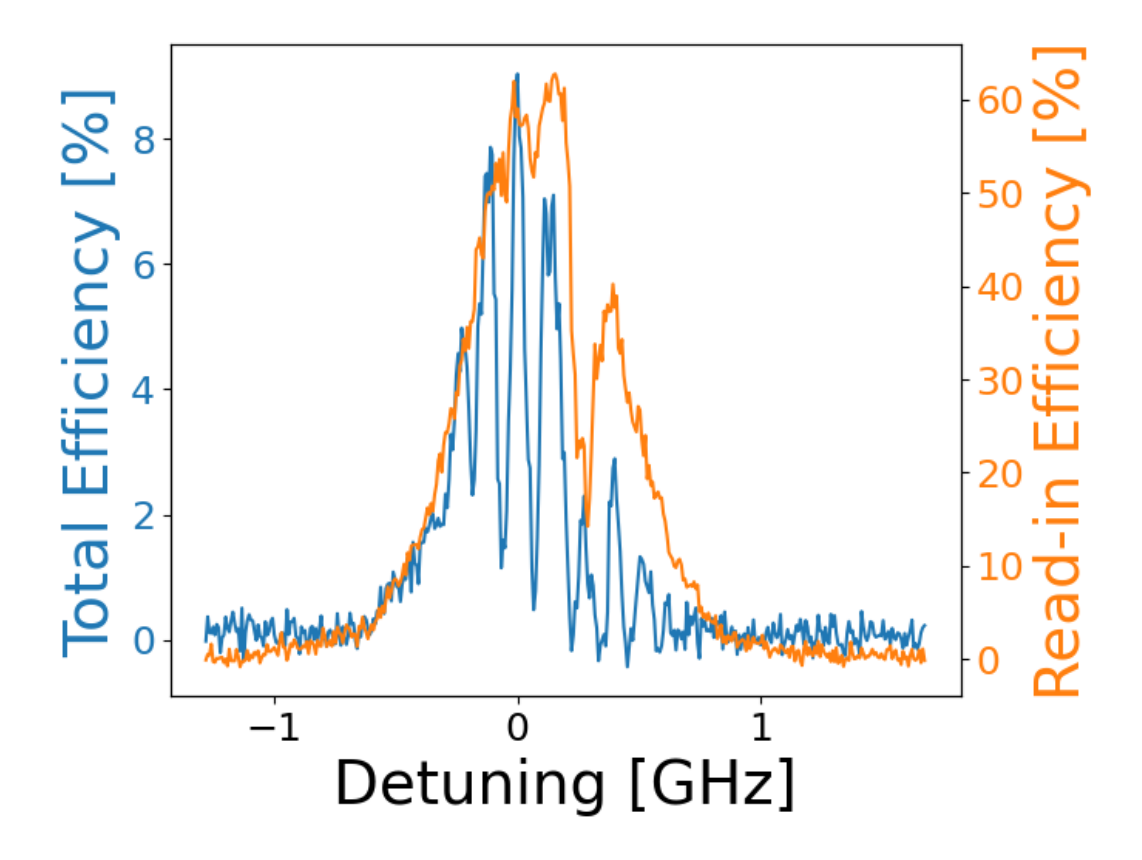
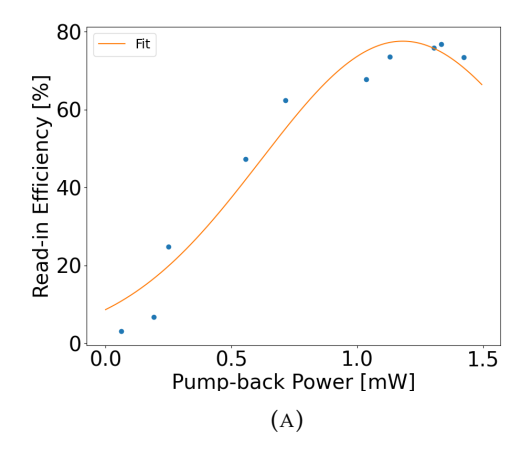


FIGURE 4.7: Efficiency vs detuning for cw AFC. This measurement allows for the recreation of the AFC structure of the atoms using the total efficiency (Blue).

#### 4.1.3 Pump-back power dependence

The optical power of the pump-back laser determines the optical depth of the AFC teeth and their width (this was shown in Chapter 3), as mentioned previously this changes the predicted efficiency of the AFC memory. Therefore this was investigated with the aim of proving these theoretical plots (Fig 2.3). The pump-back power can introduce a larger background which the combs sit on, meaning that while the OD of the peaks will be larger the efficiency may be worse. Power broadening will also widen the AFC combs leading to a lower efficiency see Eq 2.2 for efficiency approximations along with Fig 2.3 for a simulations on the effect of varying the comb width.

For the reasons discussed in Chapter 3 the power of the pump-back laser can broaden the width of the AFC teeth and therefore lower the efficiency of the protocol. In order to prove this, the pump-back power is increased and the total efficiency of the protocol is measured. This was achieved by changing the setting of the waveplate before the PBS that combines the pump and pump-back lasers (see Fig 3.3) and the dumped power was measured in order to infer the pump-back power. Fig 4.8b shows the same behaviour predicted in Chapter 2 Fig 2.3, where the efficiency peaks and then



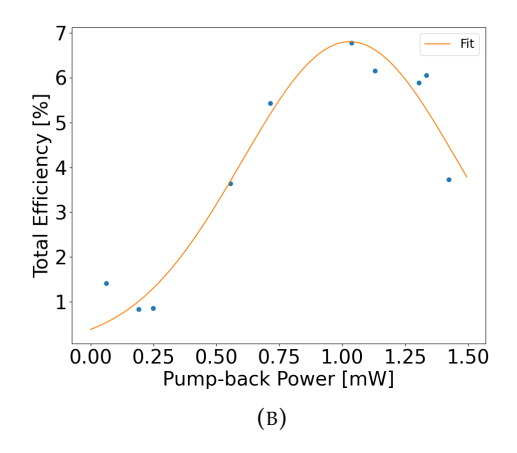


FIGURE 4.8: Pump-back Power Dependence. (A) is the read-in efficiency and (B) is the total efficiency. The read-in efficiency seems to saturate for large pump-back powers, whereas the total efficiency follows the same relationship shown in Fig 2.3a.The data points in this figure are smaller than the data points and therefore cannot be seen.

decreases as a larger optical depth of the AFC (i.e. more atoms are being pumped-back due to a higher optical power) the recalled light gets reabsorbed more efficiently than at lower powers. Whereas for the read-in efficiency (Fig 4.8a) the efficiency keeps increasing due to a larger number of atoms resonant with the input pulse bandwidth. These plots follow the same relationship seen in Fig 2.3.

#### 4.2 Pulsed AFC

There are several justifications for moving from a continuous wave (CW) regime to a pulsed regime, where the pump and pump-back are off for a portion of the experimental runtime. The first of these builds off the spectral results seen in Fig 4.7; there is a transparency window on the efficiency of the memory dependent on detuning of the pump laser. Therefore, the experiment is moved to the pulsed regime, so this feature should not exist.

The second benefit of moving to a pulsed regime is that once this experiment is used for single photons, pulsing the pump and pump-back lasers should reduce any leakage light from these lasers, making it to the single photon detectors when storage takes place. There is also spontaneous emission from the D1 excited state to the ground state as the atoms are pumped, which can cause photons to make their way to the detector; less than one percent of the atoms remain in the excited state after five excited state lifetimes (roughly 130ns). Therefore, one needs to introduce the signal at least 130ns after the pumps have been turned off to reduce the noise on the recall pulse. Understanding how long the AFC lasts after the pump lasers turn off is also important, with results given in Fig 4.13. Spontaneous emission is an effect that

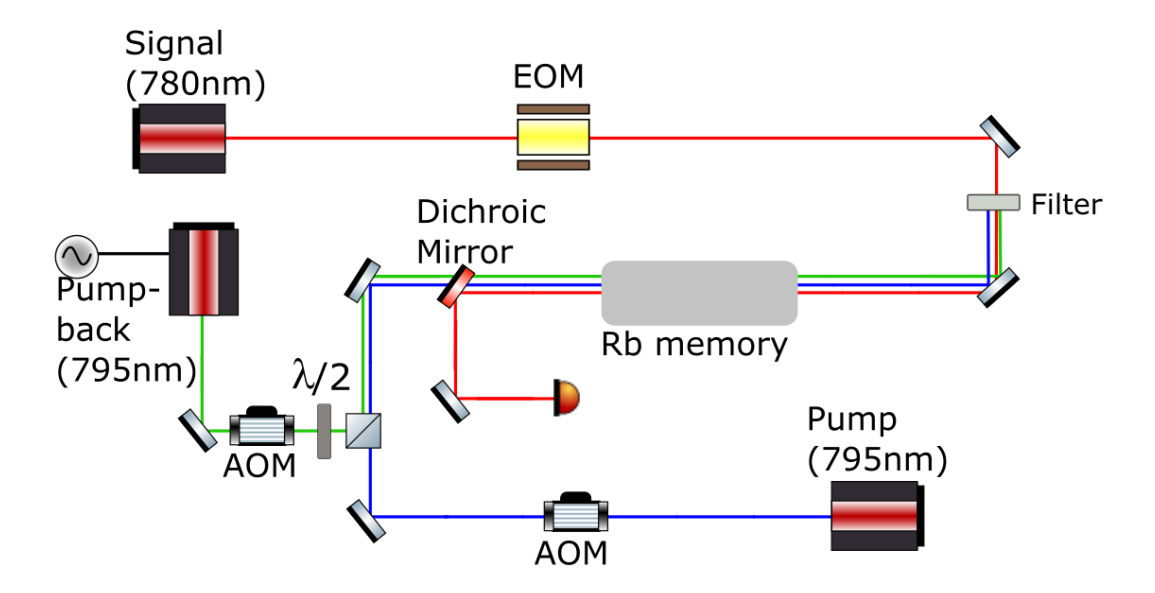


FIGURE 4.9: Pulsed AFC Experimental Diagram. AOM - Acoustic-Optical Modulator, EOM - Electro-Optic Modulator,  $\lambda/2$  - half-wave plate, the filter is used to block the pump and pump-back from coupling into the EOM.

produces photons in random directions, meaning that only a small fraction of photons actually make it to the detectors. These factors should reduce the SNR of the memory.

The pulsed regime is created using Acoustic-Optical Modulators (AOMs) to quickly block and unblock the lasers before they reach the memory.

An AOM works by an RF signal, creating a travelling wave within a crystal [158]. This standing wave creates a travelling strain wave in the material, and through the photo-elastic effect, the refractive index changes, so it is a travelling refractive index grating. The laser can then undergo Bragg diffraction off of that grating. The Zeroth order of these spatial modes is then blocked by a physical barrier such as an iris, and the first-order mode is sent through the rest of the experiment. Therefore, when the RF signal is switched off through the AOM, the higher-order spatial modes disappear, and the whole laser is blocked by the iris. This allows for quick turning on and off laser beams throughout the experiment. In total, two different AOMs are used for the pulsed regime experiment, one for the pump laser and one for the pump-back laser; these can be seen in Fig 4.9.

Fig 4.10 shows the response time for switching off the pump AOM; this response time arises mainly from the speed of sound in the AOM material and the beam size of the laser going through this medium. A larger beam means a more efficient AOM operation because the laser sees more of the diffraction grating. Still, when the RF signal is turned off, it will take longer for the trailing edge of the wave to propagate through the AOM crystal. Therefore, the pump-back laser is focused on the AOM as

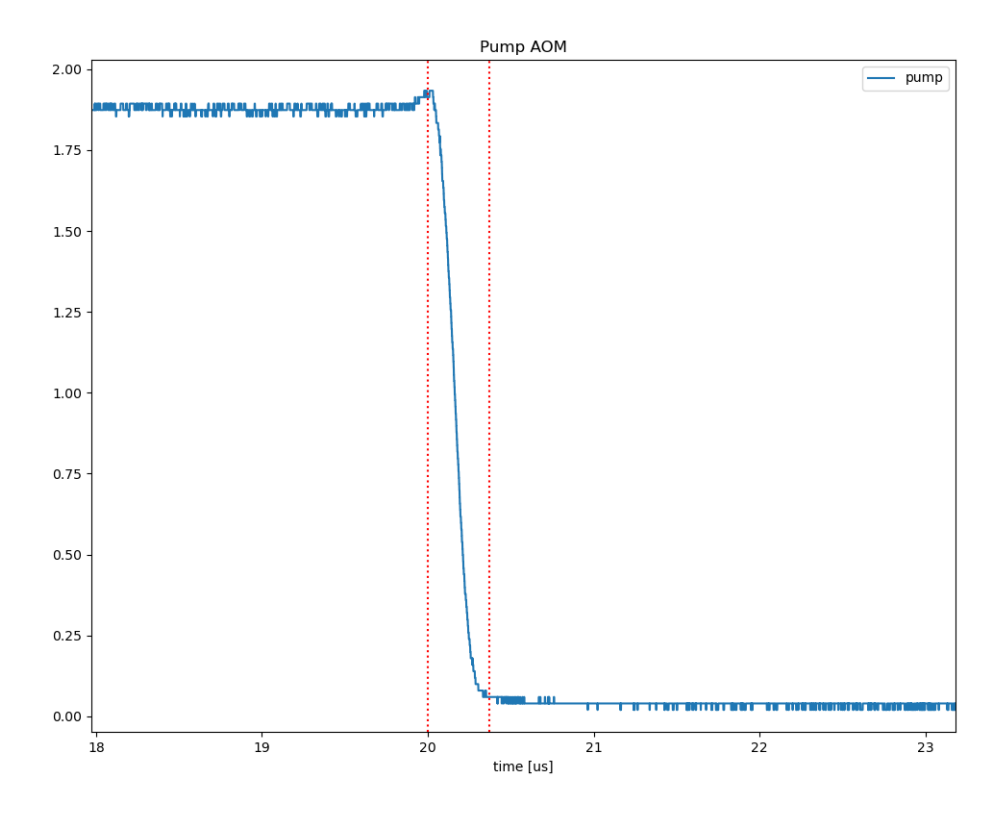


FIGURE 4.10: AOM Response time. This plot demonstrates how long it takes the AOM to block the pump laser from heading to the memory, the red dotted lines represent the time window for this process and is measured to be 370ns long.

the speed of turning this laser on/off is more critical than that of the pump laser, which is not focused. Larger optical power (AOM efficiency) is prioritised.

Therefore, understanding how long this time is is crucial for implementing the AOMs into the experiment. This data was taken by measuring the optical output of the pump laser at the cell after the light has passed through the AOM. The red lines on this plot represent the points at which the light is propagating onto the detector and the point at which it is entirely blocked; using these points, we can determine how long it takes for the AOMs to turn off entirely; this time is 370 ns. This informs the time delay for introducing the signal pulse into the AFC,  $\tau_{delay} > 370ns$ .

An AOM's efficiency is defined as the ratio of the power of the first-order spatial mode compared to the power before the AOM. This efficiency can be maximised by optimising the coupling of the light into the AOM crystal. The typical efficiency measured is around 25 - 30%.

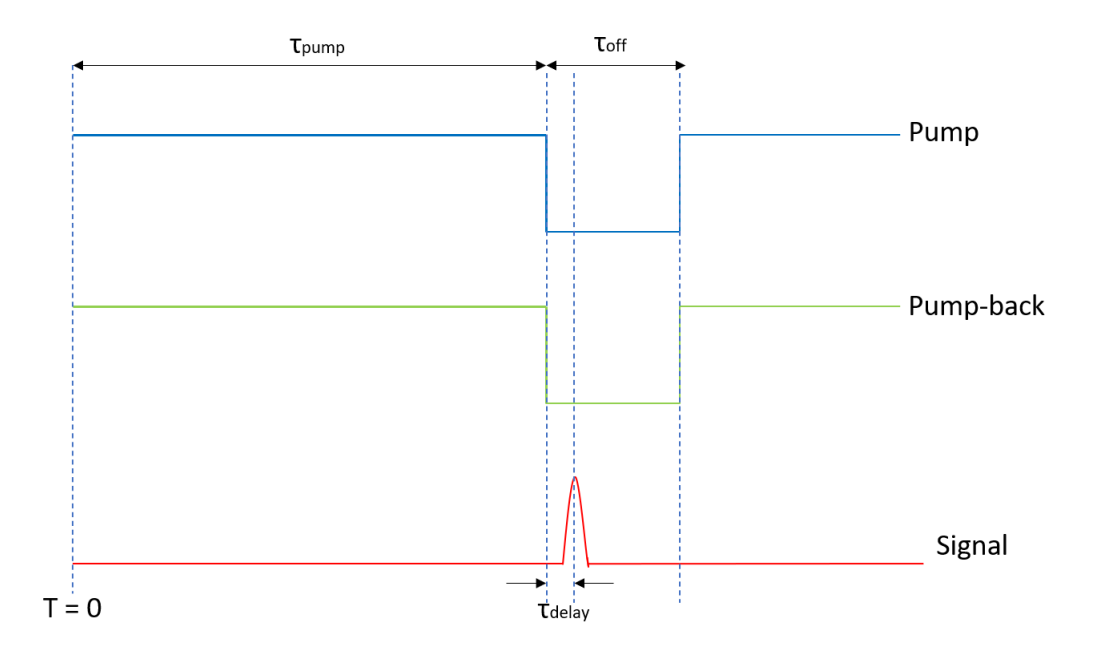


FIGURE 4.11: Pulsed regime pumping order. The pump and pump-back lasers are on for  $\tau_{pump}$  before turning off, after a time delay ( $\tau_{delay}$ ) the signal is introduced.

#### 4.2.1 Pump sequencing

Fig 4.11 shows the pumping order for the different lasers used in the pulsed AFC experiment. There are a number of factors at play when deciding the different parameters of this graph ( $\tau_{pump}$ ,  $\tau_{off}$ ,  $\tau_{delay}$ ), in order to properly create the AFC structure enough pumping time is required to empty the state initially and pump-back the required population. Also, the AOMs have a non-zero response time (as seen in Fig4.10 and stated previously); therefore, ample time is required between the AOMs turning off and the signal triggering; this is labelled as  $\tau_{delay}$  in the Fig 4.11. Finally, the overall experiment time needs to be as short as possible in order to have a high repetition rate. This will allow for more pulses to be stored and recalled per second. This is important when using single photon counters as it reduces the overall integration time. A large repetition rate will also help integrate the memory with a single photon source, for example, single photon sources based on semiconductors, which have a typical repetition rate of 50MHz - 1GHz. The goal is to maximise the standard clock rate for quantum networks with quantum memories.

#### 4.2.2 Pulsed results

Fig 4.12 shows the spectral dependence of the AFC memory in the pulsed regime; unlike the previous demonstration of this memory in the CW regime, there is no drop in efficiency (and therefore no transparency window) at the frequency of the pump laser. Once again, the structure of the AFC can be resolved, and a more accurate

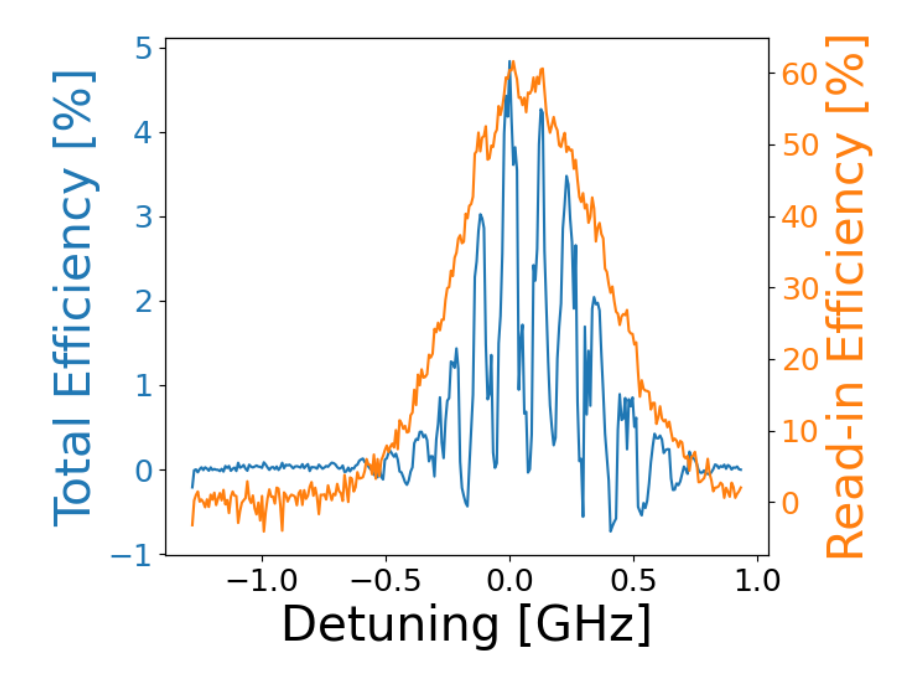


FIGURE 4.12: Efficiency vs detuning for pulsed AFC. This measurement allows for the recreation of the AFC structure of the atoms using the total efficiency (Blue). Unlike Fig 4.7 the transparency window is not present. The total efficiency is lower for this case due to normal day-to-day changes of the experimental conditions and should not be due to the changing of the experimental regime.

representation of the read-in pulse temporal width can also be seen. This AFC was made with a pump power of 134 mW and a pump-back power of 0.31 mW, along with a  $10 \mu \text{s}$  off time and a  $10 \mu \text{s}$  on time. The total efficiency of this memory is lower than the cw case due to normal day-to-day changes in the experiment, such as alignment, room temperature, laser thermalisation, thus the pulsed regime may not be the sole reason for the lower efficiency.

#### 4.2.3 AFC diffusion lifetime

The pulsed regime allows for investigation into the diffusion lifetime of the AFC structure. This is how long the atomic distribution stays as an AFC before redistributing back to the natural ground state population distribution by the arrival of un-pumped atoms entering the path of the signal and replacing the pumped atoms. This will determine when the signal pulse should be introduced, i.e., after the pumps are blocked but before the AFC structure is lost. The arrival time of the signal pulse is defined using the same Digital Delay Generator (DDG645) as the AOMs, so syncing the signal to the AOMs is trivial.

Changing  $\tau_{delay}$  from Fig 4.11 allows for the signal to be placed at different points in time, moving from the 'cw' case when the pump and pump-back are unblocked to the pulsed case where they are blocked. Measuring the total efficiency at different times

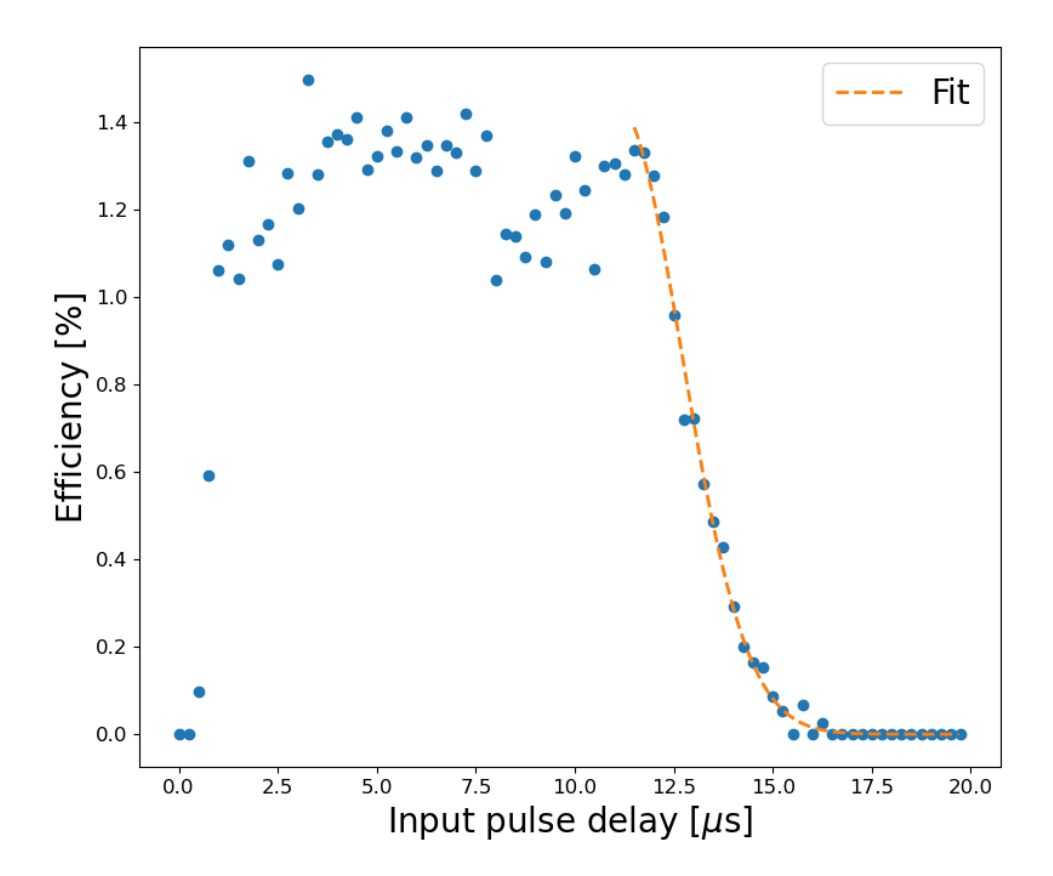


FIGURE 4.13: Diffusion lifetime. Each blue point represents the total efficiency for the storage and retrieval of light in the AFC memory for the pulsed regime. In this demonstration the pump and pump-back lasers are resonant with the atoms from 0-10  $\mu$ s. The Gaussian fit shows the diffusion lifetime of the atoms inside the laser beams with a centre at  $11.05\mu$ s

will determine how long it takes for atoms not initially pumped to enter the cell's laser interaction region. If the whole cell were pumped, this AFC structural lifetime would depend on the interaction of the atoms to redistribute the AFC.

This was plotted in Fig 4.13; this experiment had  $10\mu$ s of pumping and pump-back and another  $10\mu$ s of AOMs off time.

As the AOMs take roughly  $0.5\mu$ s to turn off, there is some extra lag time in the experiment where the AFC is still being created; therefore, the decay in efficiency starts a little later (this can be seen in Fig 4.13).

The fit in this figure is a Gaussian following the equation:

$$f(x) = e^{\frac{-(t-t_0)^2}{2\sigma^2}} (4.8)$$

Where A is the amplitude,  $\sigma$  is the width, and  $t_0$  is the centre point of the distribution. The lifetime of this decay is the diffusion lifetime,  $\tau_{diff} = \sqrt{2\sigma} = 1.53 \mu s$ . Using the ideal gas law, knowing the properties of our Rb vapour, one can determine the speed at which the atoms move within the cell. Using the equation [146]:

$$v = \sqrt{\frac{2RT}{M}} \tag{4.9}$$

Where R is the ideal gas constant (R = 8.31 J/ $mol \cdot k$ ), T is the temperature of the Rb vapour an M is Molar mass of  $^{87}$ Rb (M = 86.909g/mol) with a cell temperature of  $65.7^{\circ}$ c (338.92K) gives a velocity with respect to the k vector v = 254.59 ms $^{-1}$ . As the diameter of the signal mode was measured previously (See beam modes, Fig 3.7, earlier in this chapter) the time taken for an atom to travel across the radius of the beam is,  $\tau_{atom} = 1.107 \mu s$ . This predicted diffusion time is less than the one measured from Fig 4.13, as the above calculation assumes only one velocity class at 254.59 ms $^{-1}$  which is the case for no pump-back modulation (VSP). Once the AFC is created, there are atoms with detuned frequencies equal to the pump-back modulation sidebands (133MHz) which are a different velocity class. This velocity can be calculated as the Doppler frequency of these teeth are pre decided (comb spacing  $\Delta$ ) and usiong the equation:

$$\delta = \cos\theta \cdot k \cdot v \tag{4.10}$$

where,  $\delta$  is the Doppler frequency,  $\theta$  is the angle of the atoms vector, k is the vector of the light wave interacting with the atom (where  $k=2\pi/\lambda$ ) and v is the velocity vector of the atom. To find the angle of the vector one must rearrange eq 4.10 to get:

$$\theta = \cos^{-1}(\frac{\lambda \delta}{\tau}) \tag{4.11}$$

Using;  $\delta$  = 133MHz,  $\lambda$  = 780nm and v = 254.59ms<sup>-1</sup> gives an angle of  $\theta$  = 65°. Using this angle the velocity of these Doppler detuned atoms is calculated to be; v = 103ms<sup>-1</sup> giving a travel time through the signals cross section to be 2.514 $\mu$ s, leading to an average diffusion time of 1.77 $\mu$ s which is much closer to the measured diffusion time from Fig 4.13. These theoretical diffusion times are under the assumption that the AFC teeth have no width in frequency, as demonstrated before this is not the case experimentally (tooth width is roughly 30MHz), therefore there are more atoms that are not at this ideal velocity class and have a smaller velocity vector.

Fig 4.14 is a similar plot but with the read-in efficiency on the y-axis, the decay time for this efficiency is 6.08  $\mu$ s which is longer than the diffusion time measured from Fig 4.13 which is due to cross section area of the pump laser being 10 times larger than the

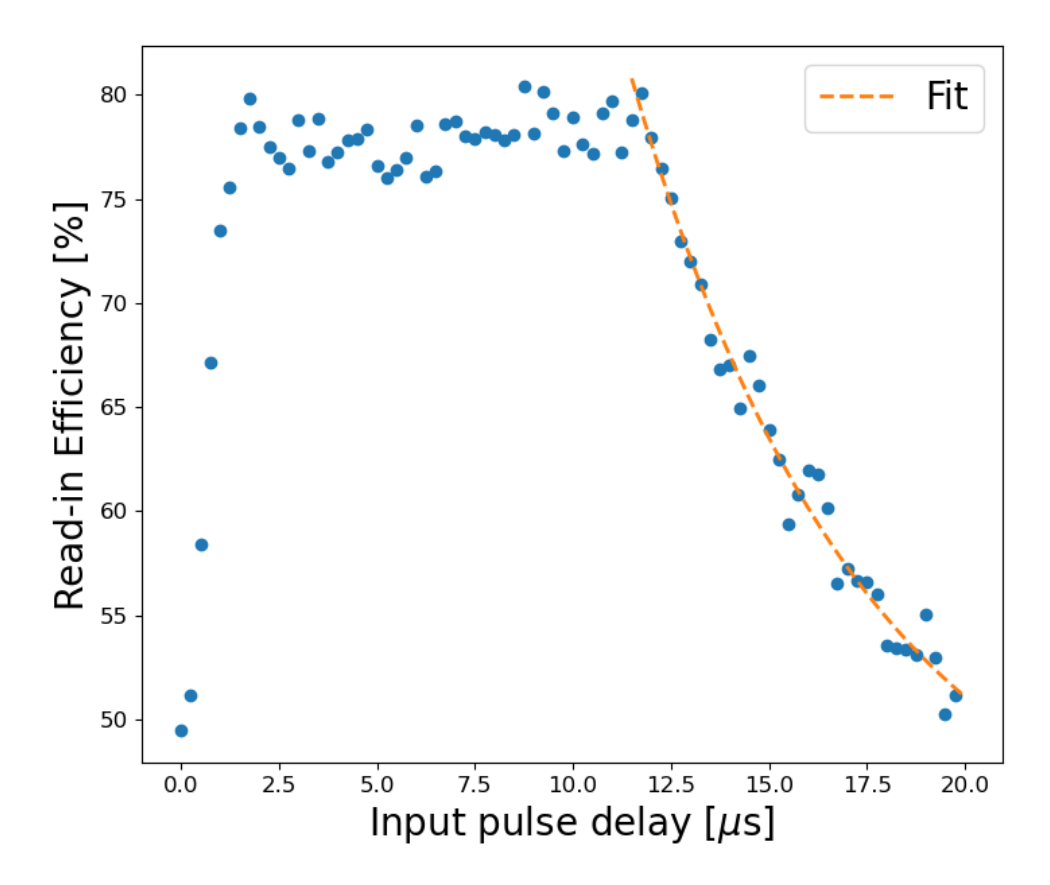


FIGURE 4.14: Diffusion lifetime - read-in efficiency. Each blue point represents the read-in efficiency for the storage and retrieval of light in the AFC memory for the pulsed regime. In this demonstration, the pump and pump-back lasers are resonant with the atoms from 0 - 10  $\mu$ s. The Gaussian fit shows the diffusion lifetime of the atoms inside the laser beams.

signal meaning that the atoms entering the signals path are still pumped into the F = 1 ground state. As a lower read-in efficiency means that there are fewer atoms in the F = 2 ground state so less of the pulse gets absorbed by the atoms.

## 4.3 Summary

This chapter outlines the entire experimental procedure, apart from the single-photon level experiments, for the AFC protocol in warm <sup>87</sup>Rb vapour. In depth details of the experiment is provided not only to provide full context on the results and investigations carried out but to allow any future reader to rebuild the experiment to carry out further experiments or to combine this experiment with another. As stated in Appendix A HQNL is moving from the School of Physics and Astronomy to the Opto-Electronics Research Centre, this means that the experiment currently in Lab

2020 in B46 will be moving to another room. Therefore this chapter will be a great help for whoever takes over the warm vapour avenue of HQNL.

This is the first demonstration of the AFC memory in the warm <sup>87</sup>Rb platform with a total efficiency of 9.04% and a read-in efficiency of 59.1%, these efficiencies are comparable to the same memory in the warm Cs platform [134] (demonstrated with a total efficiency of 9.3 % with a storage time of 8ns), showing consistency between these similar platforms. This chapter also completes the first investigation into the detuning dependence of the signal on the total efficiency of the recalled light leading to the first recreation of the AFC structure while measuring the total efficiency of the memory. This further strengthens the understanding of the protocol and allows for the same experiment to be performed in other memory platforms, such as REIDS.

Now that the memory is fully realised it allows for single-photon level inputs to be used to generate more accurate results and to test the qubit compatibility of the memory, these are investigated in the following two chapters.

# **Chapter 5**

# Warm Vapour AFC: Single-Photon Level Experiments

In order to fully realise a quantum memory for quantum applications it needs to be compatible with single photons. In order for this to be the case, there needs to be a high fidelity (F) of the output quantum state with respect to the input quantum state. This is related to the signal-to-noise ratio (SNR), F = (SNR + 1)/(SNR + 2) [159]. In the absence of a single photon source, a quantum memory can be benchmarked using weak coherent states [160]. These inputs are coherent light attenuated to the single photon level which is an average photon number per pulse of 1 or less. This is achieved by stacking neutral density (ND) filters in the path of the signal until the single photon level is reached.

Single-photon level pulses were detected with Silicon avalanche photon detectors (APDs) from Perkin Elmer (SPCM-AQ4C). These detectors have a detection efficiency associated with them, for 780nm the Perkin Elmer have an efficiency of roughly 50% [161], which is an underestimate. These are 4-channel detectors that use sensitive photon detectors (APD) that delivers a TTL signal when a photon is detected. This is connected to a time tagger module (quTAG from qutools) that records the time of this TTL signal along with the triggering TTL from the PPG that produces the signal pulse with the EOM. Start-stop measurements are implemented with the quTAG software, where the triggering TTL is the start and the APD TTL is the stop, to build histograms over some overall integration time.

The PBS that is before the memory input fibre (See Fig 3.3) is also used to fine tune the amount of power heading towards the memory and therefore the detectors. A power meter measures the average power of the signal pulses before the memory and an appropriate level of attenuation if calculated to bring that down to the single photon level. Fine tuning of the photon number is achieved with a waveplate and a PBS before the ND filters. The single photon number at the memory is estimated from

taking the count rate measured by the APD in the region of the input pulse, dividing out the detector efficiency and the transmission through the experiment. As the EOM has a limited extinction ratio the majority of the counts recorded by the quTAG is for the region outside of the signal pulse, therefore only the counts inside the signal can be used to determine the input photon number.

For the following single photon level experiments the stack of ND filters added up to a total ND = 11 (See Fig 5.1), resulting in an optical power 11 orders of magnitude lower. Along with the aforementioned PBS this allows for single photon level to be varied from nearly zero (this is the case when the photon number is equivalent to the noise floor of the experiment) to close to one photon per signal pulse.

Due to the response time of the conventional detectors used, switching to single photon detectors allows for a more accurate calculation of efficiency. One of the downsides to this approach is that the SPDs require longer integration times than the detectors used up until this point, some cases this integration time reached several minutes. The lasers used in this experiment are not actively frequency locked and therefore drift on these times scales, therefore more careful monitoring of the centre frequency of these lasers was required when performing the experiments described in this chapter and the next.

The goal of the experiments in this chapter is to characterise the single photon level AFC memory, use the faster detectors to perform experiments that couldn't be done with the previous detectors as well as achieve a more precise efficiency measurement, and to find the noise floor of the memory. More detail on these experiments will be provided in their given sections of this Chapter. The final goal of using single photon level inputs is to test the qubit compatibility of the Warm Rb AFC memory, this is investigated in the next Chapter (Chapter 6).

# 5.1 Single photon AFC measurements

In the previous chapters of this thesis, the memory inputs have been high power pulses. Thus, to make a direct comparison to the previous chapter, the output of the memory was attenuated to the single-photon level to maintain the same conditions at the memory. This was done by placing ND filters before the fibre coupled SPD, as seen in Fig 5.1. this ensures that any leakage from the AFC preparation does not impact the detection, see Fig 5.1. First, the experimental conditions from Chapter 4 and the resulting storage and retrial was measured using the single photon detectors. This can be seen in Fig 5.2a, where the read-in efficiency  $\eta_{read-in}=75.86\pm0.22\%$  and the total efficiency  $\eta_{tot}=4.80\pm0.028\%$ , for a photon number  $\mu=0.151\pm0.00018$  before the detection fibre. The regions for calculating these efficiencies are the same as before, in this figure the blue region is for the input pulse and the red region is the recalled pulse.

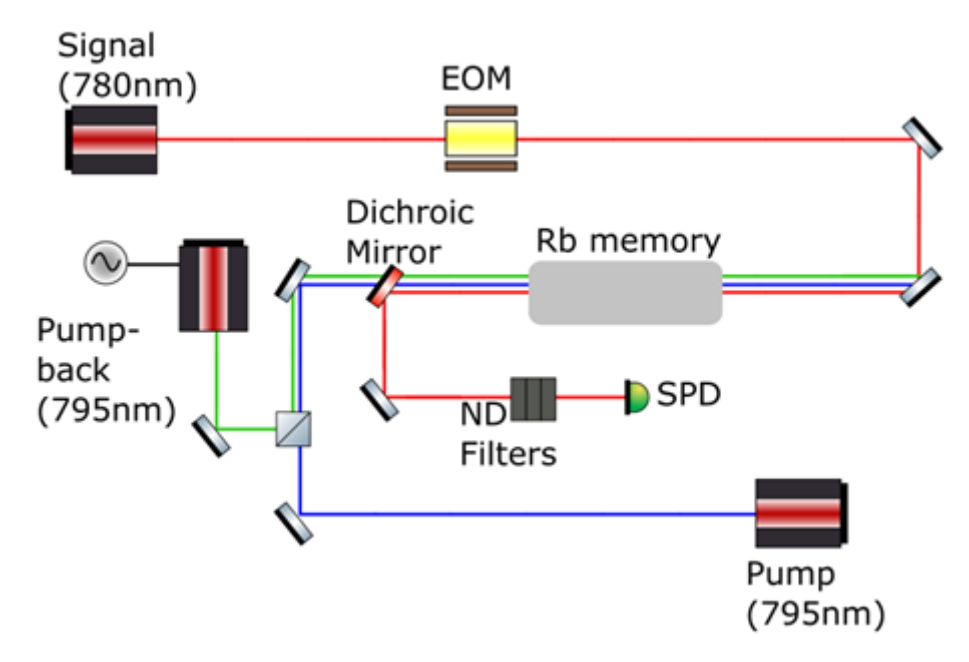


FIGURE 5.1: Single-photon level output AFC Experimental Setup. Where EOM - Electro-optic modulator, ND - Neutral density filters, SPD - Single Photon Detectors.

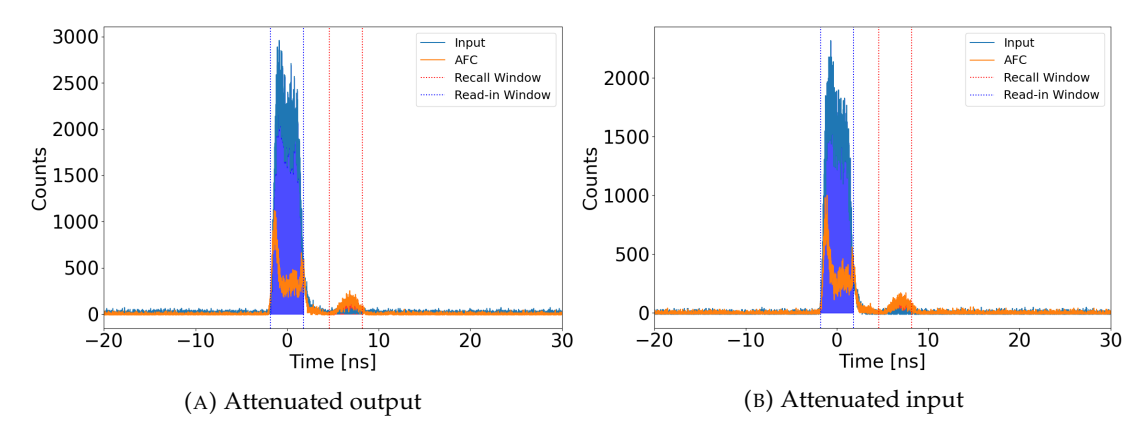


FIGURE 5.2: Single-photon level AFC demonstration. This is comparing the attenuated AFC input vs attenuated output.

The ND filters were then moved to before the memory fibre so that the single photon level is reached before the memory, this is to simulate the behaviour of the memory with a true single photon source as an input. The AFC memory for this case can be seen to perform in the same way, see Fig 5.2b, comparable read-in and total efficiencies; where the read-in efficiency  $\eta_{read-in}=73.62\pm0.23\%$  and the total efficiency  $\eta_{tot}=4.14\pm0.030\%$ , for a photon number  $\mu=0.113\pm0.00016$ . The difference in these values is due to drifts in the pump-back laser frequency.

From this point forward the single photon level will be achieved before the memory cell, i.e. the configuration where the ND filters are before the fibre input for the memory.

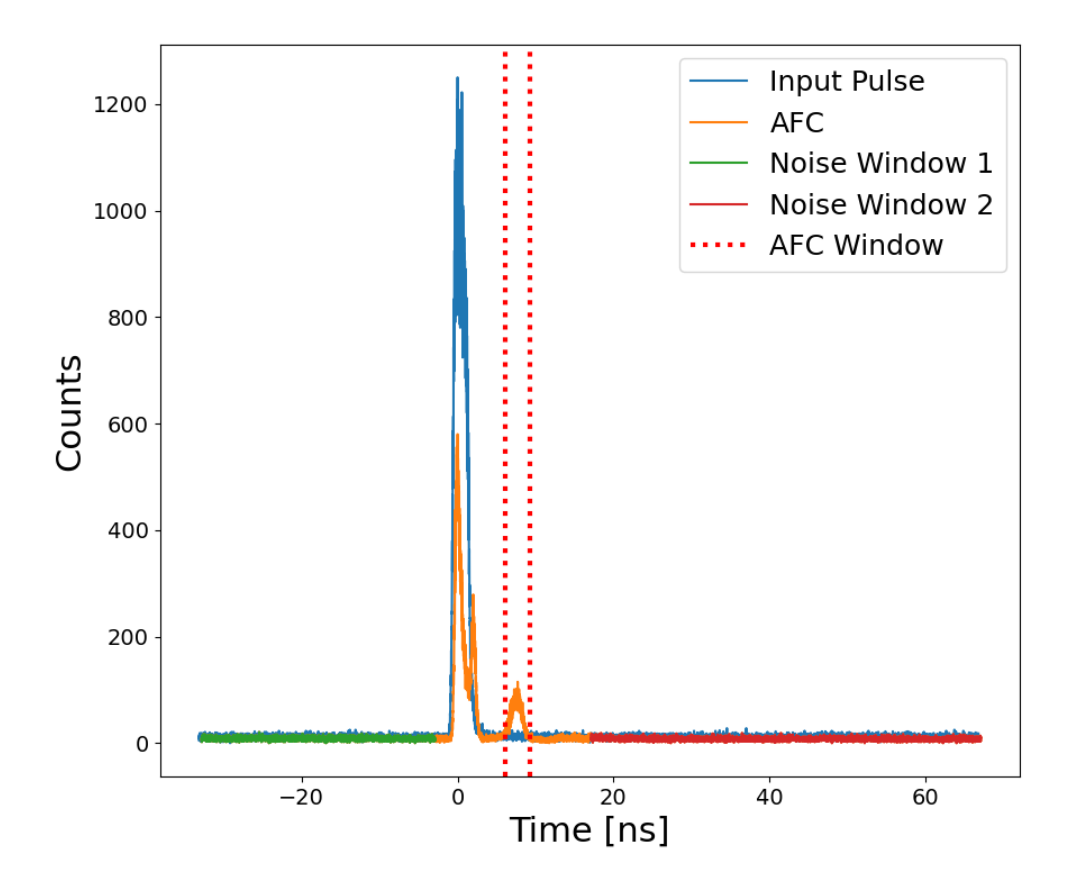


FIGURE 5.3: SNR calculation regions. The noise counts in Noise Window 1 (green) and Noise Window 2 (red) are averaged over the width of the AFC window (red dotted lines) and compared to the recalled counts (orange) in this window to obtain the SNR.

#### 5.1.1 Signal to Noise ratio

The Signal to Noise Ratio (SNR) is defined as the area of the output pulse compared to the noise floor of the memory in the same integration window. The recall pulse is integrated over a 3.2ns time window capturing the whole pulse. The noise is obtained by integrating the counts over the time regions defined by Noise Windows 1 and 2 in Fig 5.3. This represents a total window duration of 80ns, giving a much larger number of counts for a greater certainty. The noise is then proportionally scaled to the signal integration window of 3.2ns.

SNR is then calculated using the following equations:

$$SNR = \frac{N_{AFC}}{Noise} \tag{5.1}$$

$$Noise = \frac{NW1 + NW1}{Total\ Noise\ Window} \cdot AFC\ Window \tag{5.2}$$

Where, NW1 and NW2 are Noise Window 1 & 2 respectively and is the total number of counts for these regions represented on Fig 5.3, the total noise window is 80ns,  $N_{afc}$  is the total number of AFC counts in the AFC Window. In this figure, the SNR = 6.29  $\pm$  0.056 over an AFC window of 3.2ns.

In this experiment the main source of noise is from the limited of extinction of the EOM. The EOM leakage is resonant with the atoms, therefore is absorbed when the AFC is present, due to there being more atoms at the frequency of the background; for example, the total noise counts for the input pulse (blue trace) is 88,991 whereas for the AFC pulse (orange trace) it is 62,812 which is 70% of the input noise, which is comparable to the read-in efficiency.

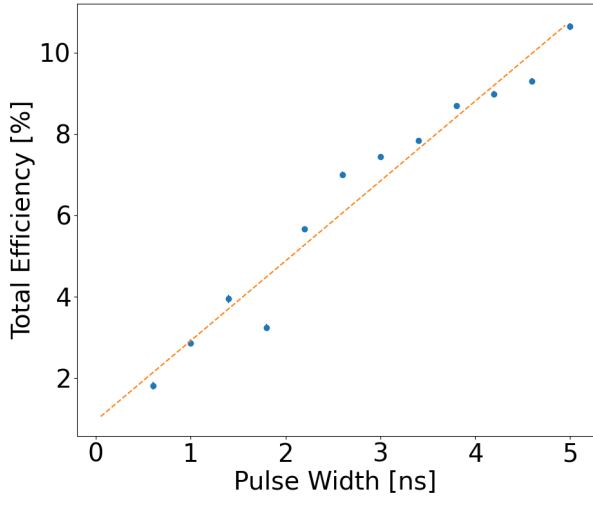
This can be seen in Fig. 5.3 where the background level (the data away from the input and the recalled pulses) is lower for the AFC case.

#### 5.2 Pulse Width Characterisation

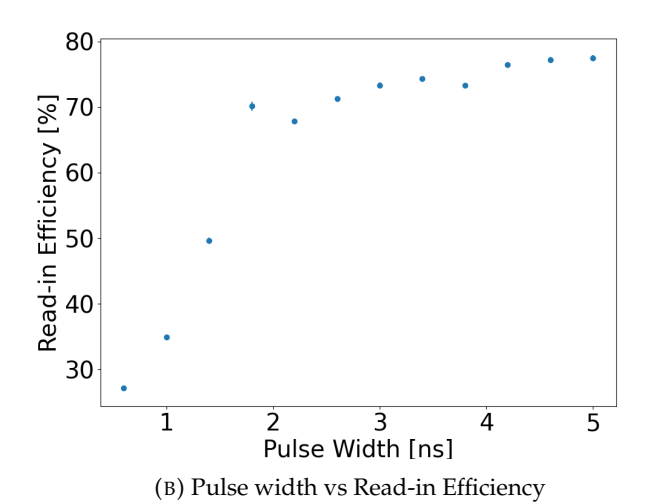
As the single photon detectors give a more accurate view into the operation of the memory, they can be used as a tool to fully understand the process of creating a pulse using an EOM and therefore can be used to optimise the input pulse on the pulse generation software to optimise the AFC storage efficiency.

Using the EOM one can change the bin width of the input pulse, this EOM input is programmed with square pulses of differing duration that are delivered to the EOM to generate pulses. The resulting pulses aren't squares due to the response time of the PPG and the EOM. Fig 5.4a shows that the total efficiency of the AFC memory is roughly linear with the input pulse width, which is due to the wider temporal pulses giving a narrower input pulse bandwidth meaning that more of the input photons are resonant with the optically deep AFC teeth, thus leading to a larger efficiency. One would expect the total efficiency to level out once this bandwidth reaches the width of an individual AFC tooth, but as the typical tooth width is around 30MHz, this corresponds to a 33ns wide input pulse which would 'cover up' the recall pulse not allowing the efficiency to be measured, this can be seen in Fig 5.5b as the falling edge of the input pulse almost overlaps with the rising edge of the recall pulse, also if the bandwidth of the signal is less than the width of an individual tooth then storage and recall won't occur.

Fig 5.4b shows how the input width affects read-in efficiency. The read-in efficiency seems to plateau at around 1.8ns or 0.55GHz, which is roughly equivalent to the AFC's most optically deep peaks which give the best read-in efficiency. Once the bandwidth of the input pulse is less than the total length of the comb then there is



(A) Pulse Width vs Total Efficiency



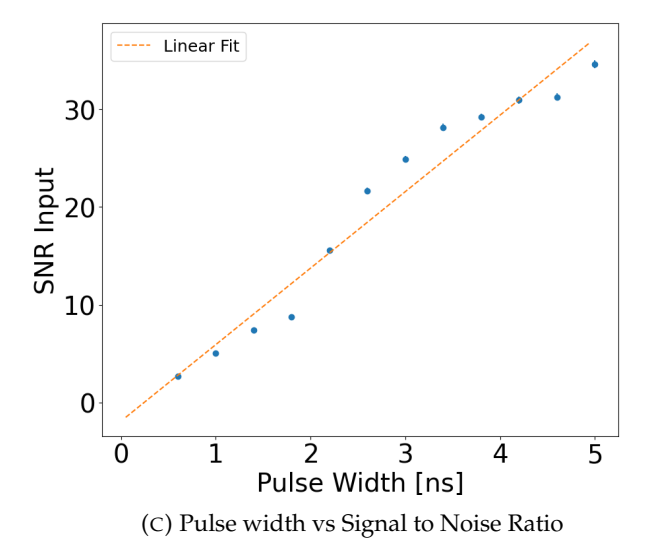
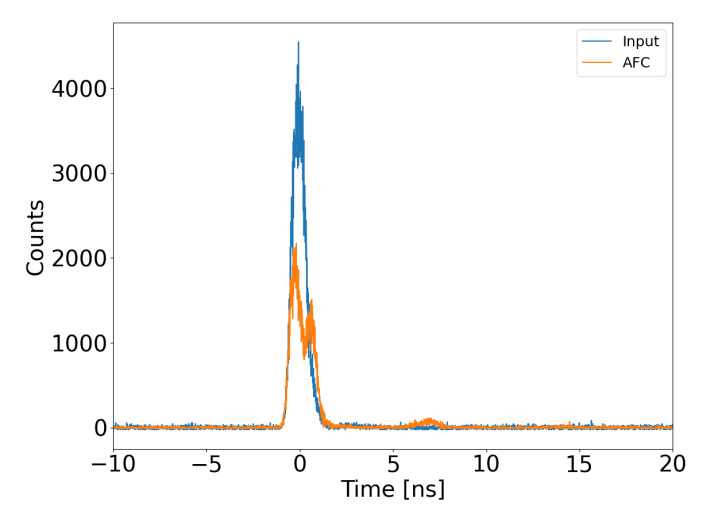
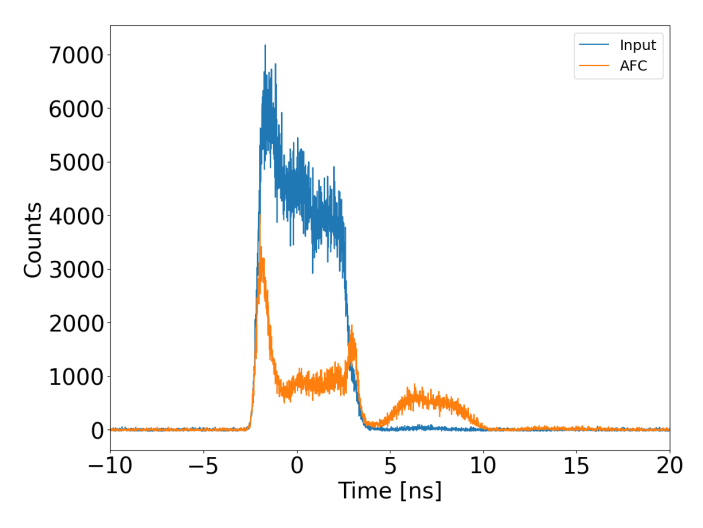


FIGURE 5.4: Pulse Width Investigation



(A) 1ns width:  $\eta_{read-in}=34.89\pm0.09\%$ ,  $\eta_{total}=2.86\pm0.029\%$  and  $\mu=0.085\pm0.00014$ .



(B) 5ns width:  $\eta_{read-in}=77.48\pm0.14\%$ ,  $\eta_{total}=10.64\pm0.027\%$  and  $\mu=0.397\pm0.00031$ .

FIGURE 5.5: Comparison of different input pulse widths. This shows the effect that the input pulse width has on the efficiency of the memory.

efficiency read-in of the input light due to all the light being resonant with the atoms. Therefore, the read-in efficiency levels out.

Fig 5.4c shows the SNR compared to the input pulse width, this is a proportional relationship, as the noise level does not change, but the number of photons inside the input pulse increases with pulse width. All of the plots in Fig 5.4 have error bars associated with them, but they are absorbed by the size of the points. The PBS before the memory fibre was constant throughout this experiment, but as the width of the input pulse was increased the photon number will also increase, this changed from  $\mu = [36 \pm 0.09] \times 10^{-3}$  to  $\mu = [542 \pm 0.35] \times 10^{-3}$ .

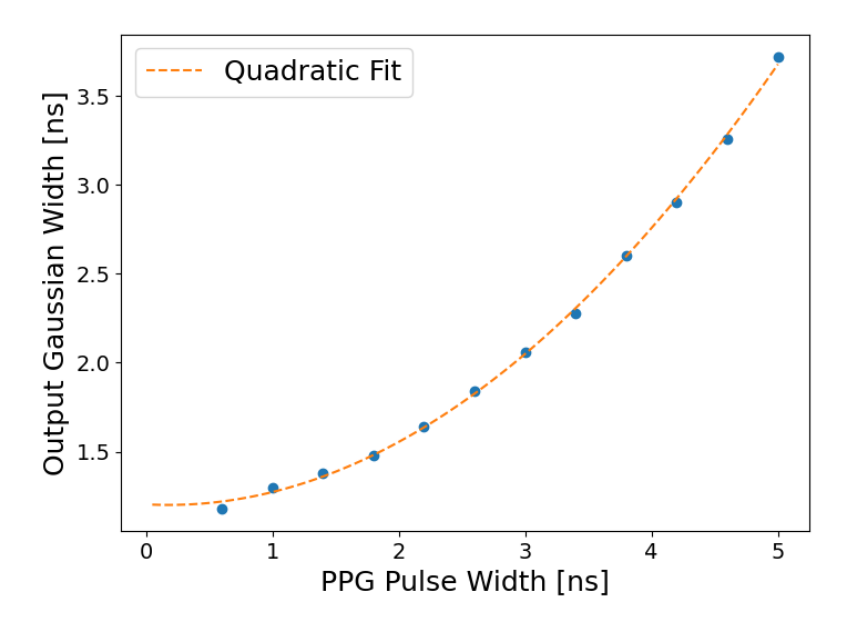


FIGURE 5.6: PPG width vs recall pulse width with a Guassian fit that intercepts the y-axis at 1.20ns

The recalled pulse of the memory is always a Gaussian, therefore fitting to this pulse one can extract the width. Fig 5.6 shows how this recalled width changes with the PPG software's width for input pulse, fitting a quadratic function to this data allows for the y-intercept to be found which will be the bandwidth of the AFC structure, as for large input pulse bandwidths (greater than the AFC bandwidth) the AFC bandwidths will only absorbed. On this Figure this was found to be 1.20ns or 0.831GHz. From Fig 5.4b it was concluded that the width of the AFC is 0.55GHz, this value is for efficient read-in of the input light - when the light is resonant with the largest amount of atoms. Whereas Fig 5.6 shows the bandwidth of all the atoms within the AFC structure, which is close to the measured value of 0.9GHz.

For the following sections, a pulse width of 3.2ns is used as this is a good trade off between SNR and temporal separation between the input and retrieved pulses.

# 5.3 Single photon number characterisation

The photons per pulse is adjusted using the waveplate behind the PBS for these measurements, the range of  $\mu$  was changed from close to zero to greater than one, [938  $\pm$  0.47]x10<sup>-3</sup> to [18.3  $\pm$  0.066]x10<sup>-3</sup> average photons per pulse before the memory.

Fig 5.7a shows how the total efficiency changes with the single photon number  $\mu$ , for low photon numbers the total efficiency of the memory is constant, what is observed

here is the instability of the lasers, given that the total time for this measurement is 240 seconds per point or 44 minutes in total.

Fig 5.7b shows how the SNR changes with the single-photon number  $\mu$ , as  $\mu$  reduces the SNR stays roughly the same (at a value of 18.6) until it reaches 0.28 average photons per pulse where the SNR begins to decrease. This is the point where the recall pulse count rate is close to that of the background of the pulse caused by the EOM extinction. The SNR saturation value depends on the extinction ratio of the EOM which is quoted at 0.1%, but in reality is much higher, thus an EOM with a better extinction ratio will give a larger SNR value. If true single-photons were used the SNR would only depend on the dark counts, the leakage of the control pulses and fundamentally it is limited by the efficiency of the memory as a larger efficiency will give a larger SNR.

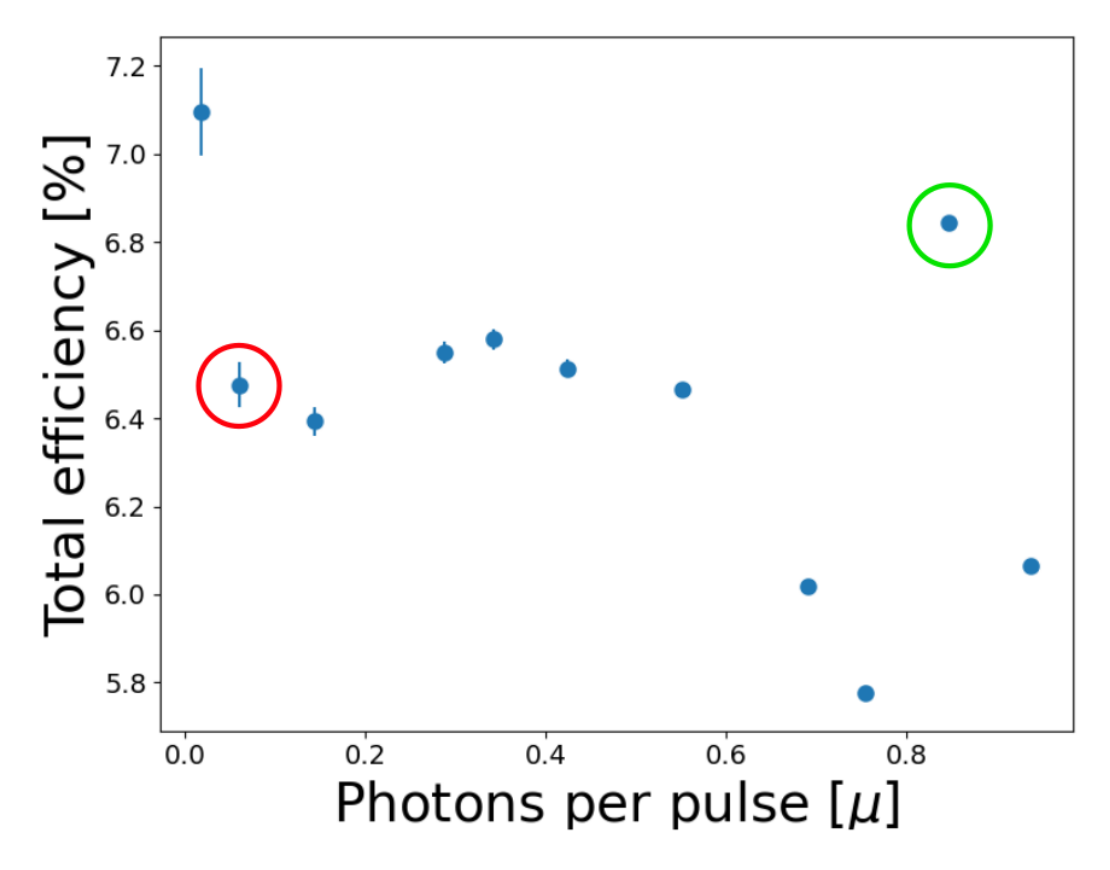
Fig 5.8 shows a direct comparison of different values of  $\mu$ . Specifically, Fig 5.8a is  $\mu = 0.846 \pm 0.0004$  and Fig 5.8b is  $\mu = 0.06 \pm 0.0001$ .

### 5.4 Varying Storage Time

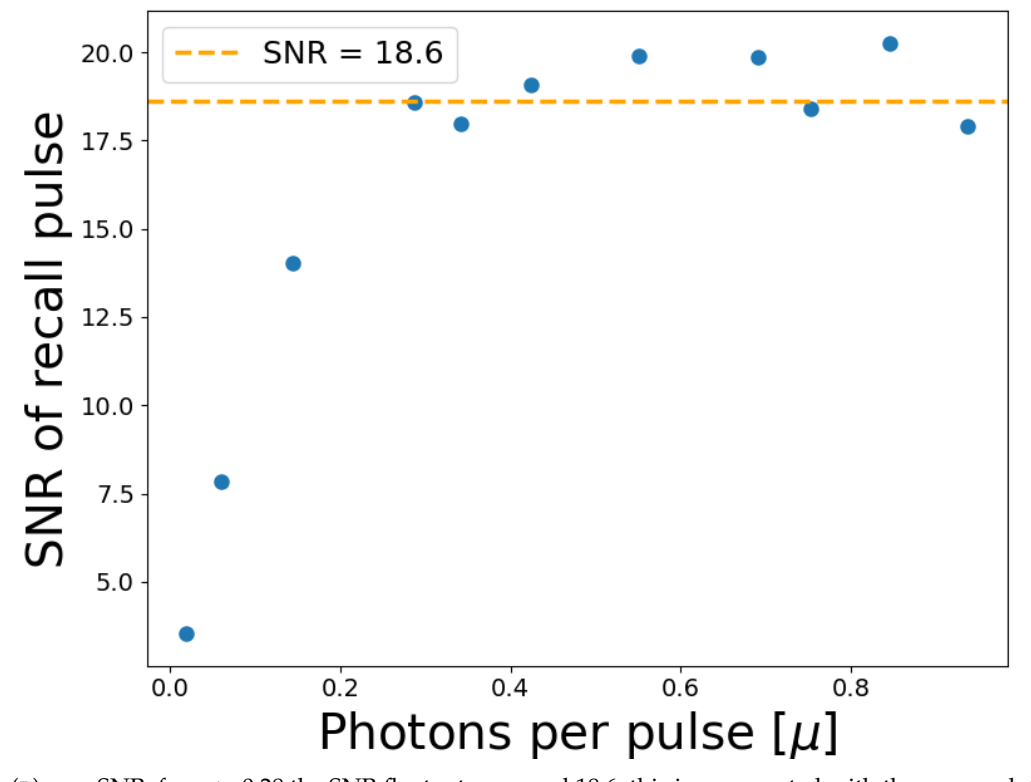
By changing the comb spacing of the AFC one can change the storage time by changing the modulation frequency of the pump-back laser using an AWG, this is measured using the single photon APDs due to the better recovery time and sensitivity that it offers.

In order to have regular spaced comb teeth, the AFC spacing used is matched to that of the relevant hyperfine splittings resulting in reduced freedom of the storage time. As the excited state separation for the transition that the AFC is built off is 266.650 MHz, the comb spacing is chosen to be integer divisibles of this separation. For example, 266.650 MHz/2n where n = 1,2,3,4. The modulation amplitude on the pump-back laser needs to be increased so that the higher order modulation modes can sufficiently overlap.

Fig 5.9 is an illustration showing how the AFC changes with different pump-back modulation frequencies. In these figures, the black arrows on the left (seen on their own in Fig 5.9a) represent the excited states F' = 2 and F' = 3, refer to Fig 3.1 for the energy level diagram of <sup>87</sup>Rb. The plot on the right of Fig 5.9a-e, is the AFC structure for each of these modulation frequencies; 133MHz, 66MHz, 33MHz and 16MHz. These spectra were taken in the CW regime therefore the position of the pump laser can be seen adding extra peaks in the comb, this can also be seen on the green trace which is the ground state population after pumping. Once the single photon detectors are used to measure the AFC storage this extra 'pump peak' is no longer there as this

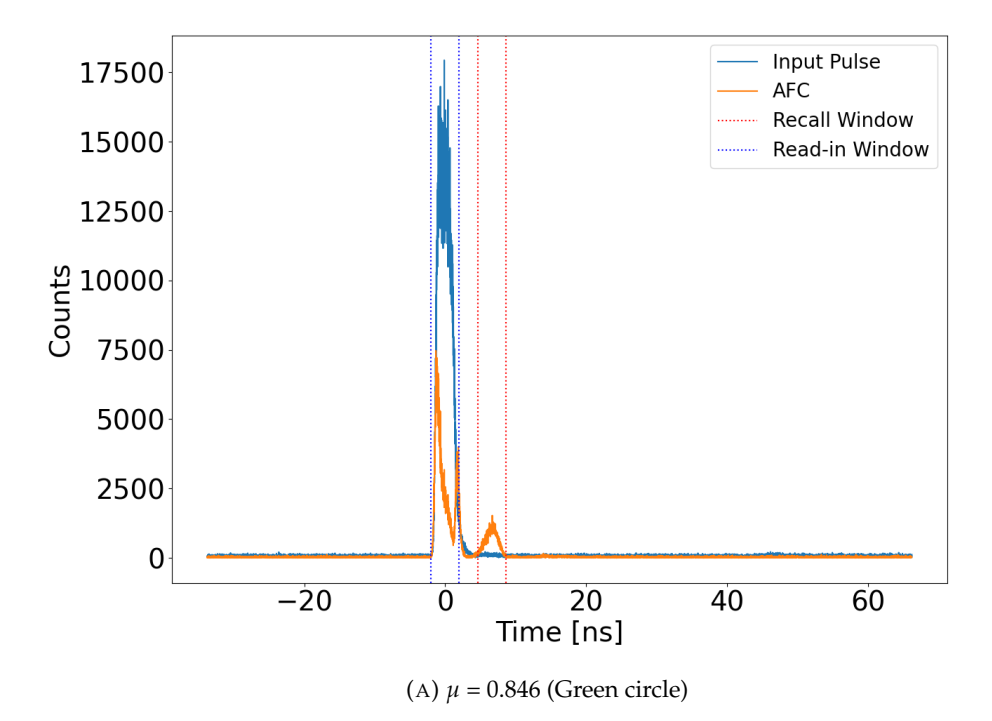


(A)  $\mu$  vs Total Efficiency, the red circle corresponds to Fig 5.8b and the green circle is for 5.8a. The variation in these efficiency values is caused by the instability of the lasers used for the memory.



(B)  $\mu$  vs SNR, for  $\mu$  > 0.28 the SNR fluctuates around 18.6, this is represented with the orange dotted line

FIGURE 5.7: Single Photon Limit Investigation



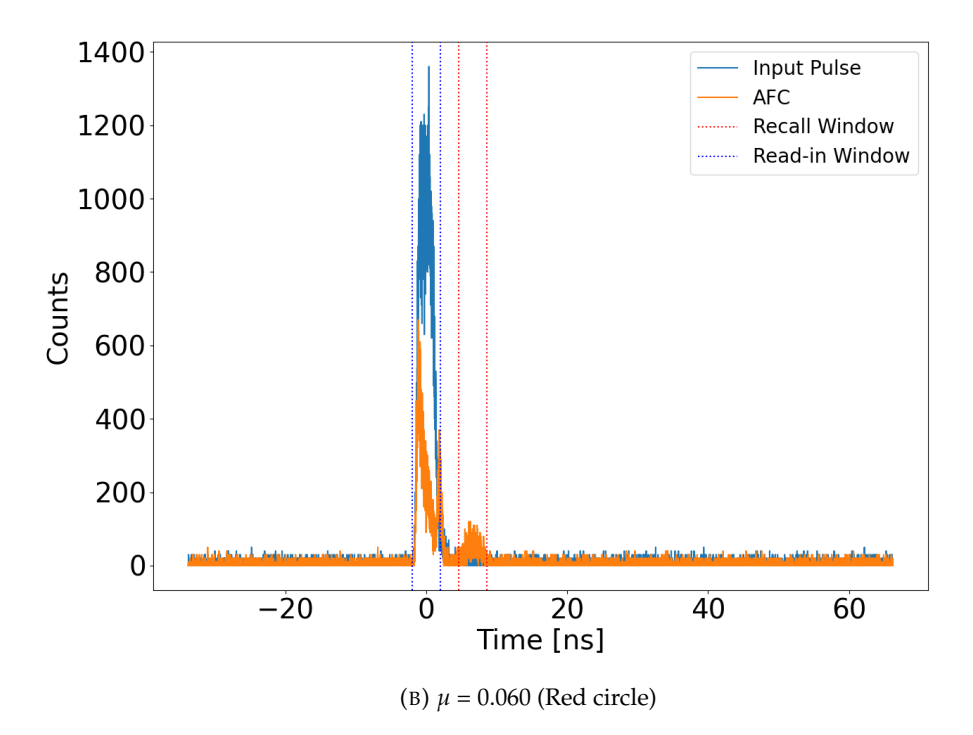


Figure 5.8: Comparison of different  $\mu$ , the colour in brackets refers to the circles from Fig 5.7a

measurement is done in the pulsed regime meaning that no atoms are being optically pumped once the input pulse arrives meaning that only the AFC structure is present.

This figure also visualises the idea of overlapping the atomic velocity classes from each transition, this is shown on the left of Fig 5.9b-e. Pumping back with a frequency modulated laser results in multiple atomic velocity classes. Each velocity class created results in three absorption features, corresponding to three allowed transitions. With weak modulation amplitude, there are three string frequency modes on the laser: the carrier at  $\Omega_0$  and two sidebands ( $\Omega_0 \pm \Omega_{mod}$ ). Choosing the modulation frequencies above, ensures that the absorption features created form a regular spaced comb. For example, the  $+\Omega_{mod}$  atomic velocity class for the F = 2 - F' = 2 transition overlaps with the  $-\Omega_{mod}$  atomic velocity class for the F = 2 - F' = 3 transition, for an  $\Omega_{mod} = \delta_{hyperfine}/2$ .

When increasing the storage time of memory a difficulty in overlapping these side bands arises, Fig 5.9 shows that the overlap now needs to be achieved with the higher order side bands of this modulation. This is achieved by increasing the modulation amplitude from the AWG into the pump-back laser. Due to the higher order side bands having a lower height than the lower order ones this overlap and therefore the teeth of the AFC become weaker. This can be seen clearly in Fig 5.9e where the effect of this is the 'broadening' of the transitions seen in Fig 5.9a, this will reduce the efficiency of the input light stored into this AFC due to less well defined AFC teeth which, referring to Eq 2.2 gives a larger  $d_0$  that is close to d and results in a much lower efficiency.

These spectra are used for AFC storage where the efficiency values are represented in Fig 5.10 which is a plot of storage time vs efficiency.

This data has a fit which is a combination of two exponential decays, one with a 1/e lifetime of 2.95ns and the other with a lifetime of 10.24ns. This can be explained by the AFC structure essentially going away with smaller tooth separation, this can be seen in Fig 5.9, the smaller  $\Delta$  values cause the teeth to overlap to the extent where the structure starts to resemble a VSP rather than an AFC. This leads to a change in lifetime.

The storage time is limited mainly by the excited state lifetime of the F' = 3 energy level which is 26ns [142], as this lifetime is also an exponential decay there is still a small population in this excited state at the longer storage times, but this is one of the factors contributing to the near zero total efficiency of the AFC storage. Other factors limiting the efficiency of the longer storage times include the messy AFC structure created by the teeth of the AFC from the pump-back population overlapping, as seen in Eq 2.2. This occurs due to the linewidth of the laser being around 30MHz, therefore pump-back laser modulations near this linewidth causes this observed overlap of AFC teeth.

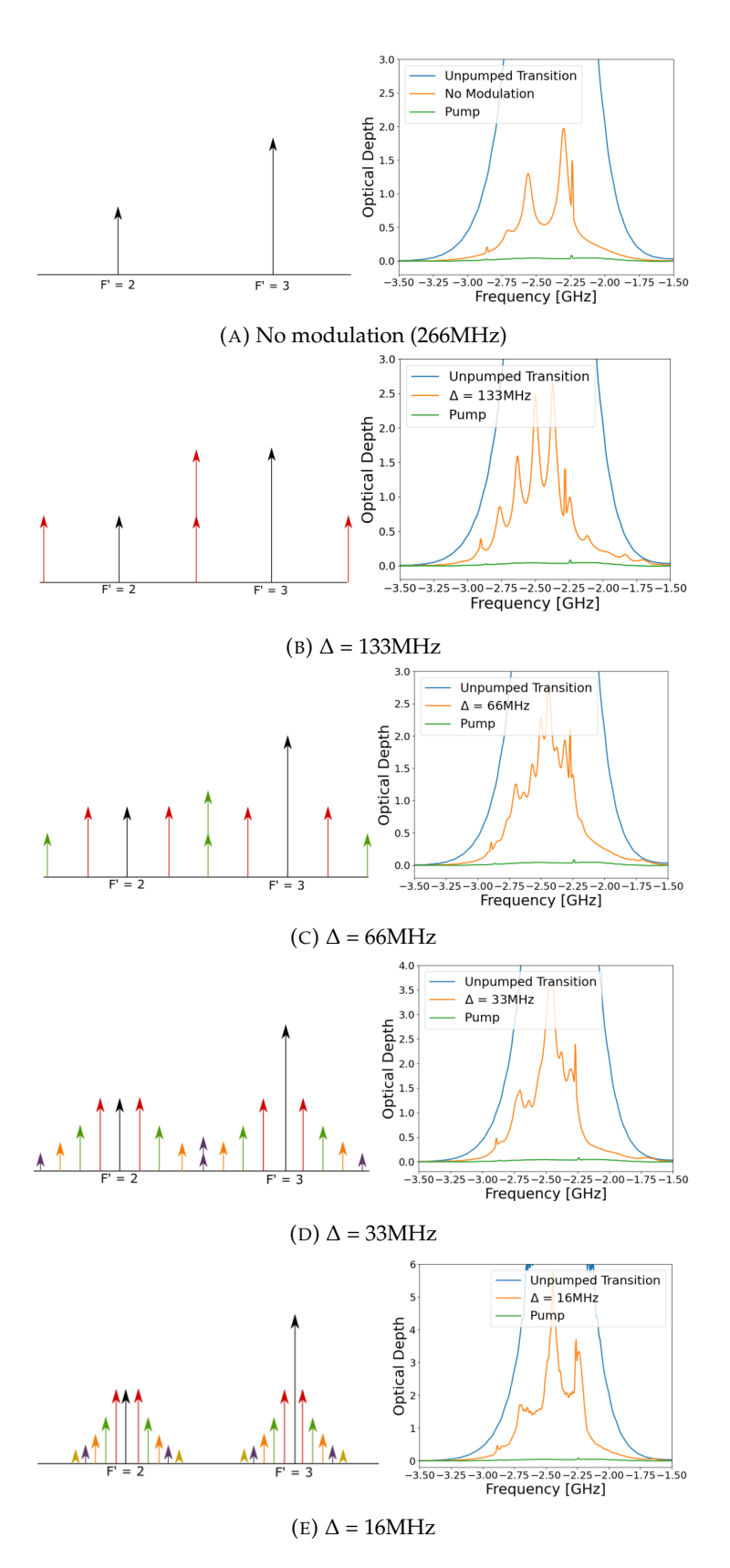


FIGURE 5.9: AFC structures for different pump-back laser modulation. The left side of sub figures demonstrates how the higher order frequency sidebands of the transitions overlap change with modulation frequency, the different colours are for the order of the sideband. The right side of these sub figures are the associated spectrum for these modulation frequencies.

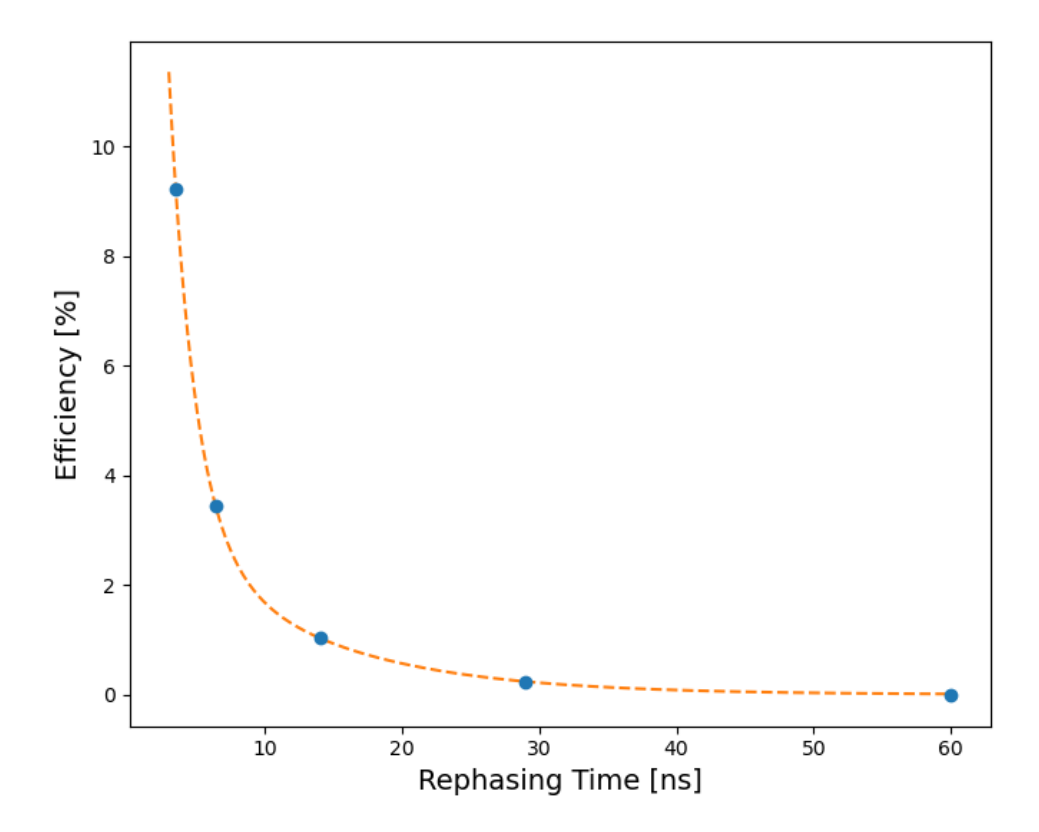


FIGURE 5.10: Storage Time vs Total Efficiency. This is fitted with a function that is a combination of two exponential decays, the first one is fitted to the first three points and has a lifetime  $\tau$  = 2.95ns and the second one is fitted to the last two points with a  $\tau$  = 10.24ns.

While increasing the storage time is experimentally trivial there is a lack of freedom in defining a storage time, this means that this memory can be limited with its applications.

There have been several approaches into overcoming this limitation, for example experiments where the input signal, after absorption into the excited state, is mapped to a longer lived ground state have been proposed within the HQNL research group. This method requires using a strong magnetic field to lift the degeneracy of the F=1 and F=2 ground states and using selection rules to empty one of the Zeeman ground states to allow for this signal to be mapped into it. This would require a control pulse resonant with the excited state that is storing the light and this new storage ground state to map and un-map the light into. To achieve a  $\pi$  pulse the pulse duration ( $\tau$ ) and Rabi frequency must satisfy;  $\Omega \tau = \pi$ . For a  $\tau = 3.5ns$ ,  $\Omega \approx 9x10^8 rad/s$ . Using the saturation relations:  $\omega/\Gamma = \sqrt{I/2I_{sat}}$  [162], for <sup>87</sup>Rb D2 transition; the natural linewidth  $\Gamma = 2\pi \times 6.07$ MHz and the saturation intensity  $I_{sat} = 1.6$ mW/ $cm^2$  [142] gives an intensity of 1.77W/ $cm^2$ . This would require a pulsed laser with a larger power

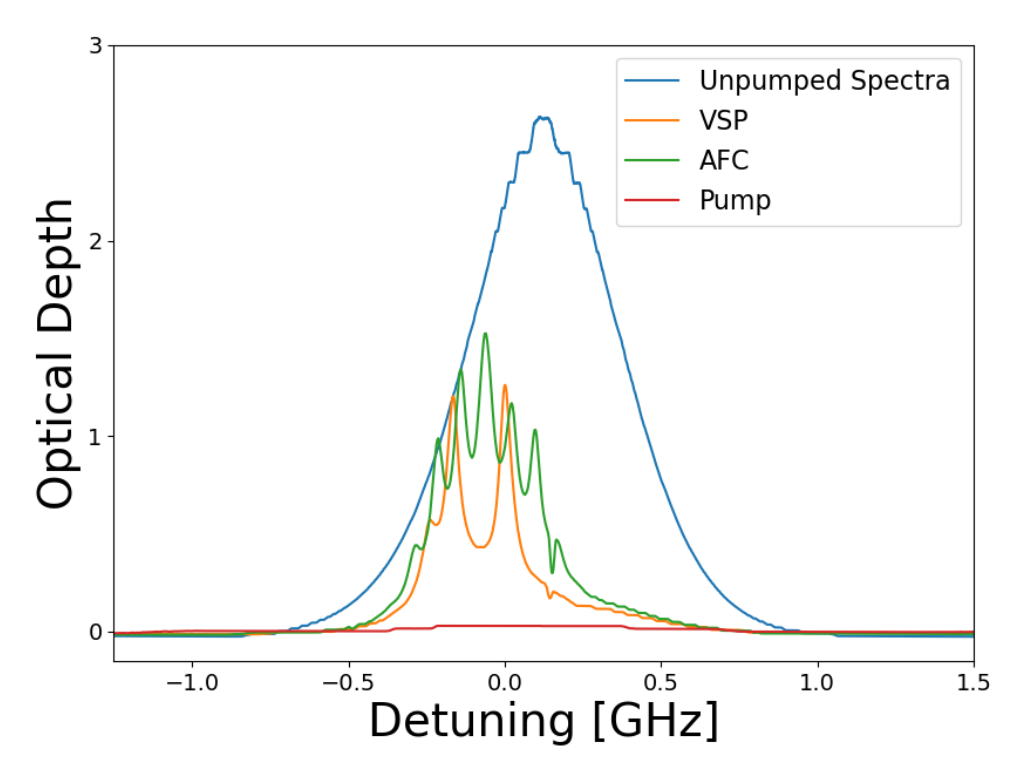


FIGURE 5.11: AFC spectrum in F = 1 ground state

output than the ones used for the experiments in this thesis, this laser can also be focused into an area of a few mm to reduce the overall required power.

### 5.5 AFC in F = 1 ground state

The AFC experiment was also performed in the F = 1 ground state to justify why the F = 2 ground state was used for the majority of the memory characterisation experiments. To make the structure seen in Fig 5.11 the pump-back laser was modulated at a frequency of 78.5MHz which is half the excited state separation of the F' = 2 and the F' = 1 levels (see Fig 3.1) which corresponds to a storage time of 12.7ns. It can be seen that the unpumped spectra has a stepped shape at large optical depths, this behaviour is due to the resolution of the oscilloscope (Rigol ds7024) used to measure this spectra, this resolution is 0.005V This experiment was performed at the single photon level due to this longer storage time and therefore lower efficiency as the Menlo APD detector used in Chapter 4 cannot capture recall pulses with efficiency this low. This AFC was created with a 360 $\mu$ W pump-back and 120mW pump powers.

Fig 5.12 shows the storage and retrieval of standard pulse with an integration window width of 3.2ns and a single photon number of  $\mu$  = 3.20  $\pm$  0.0009. over a 120s integration time, with a trigger rate of 100KHz. This storage gave a read-in efficiency

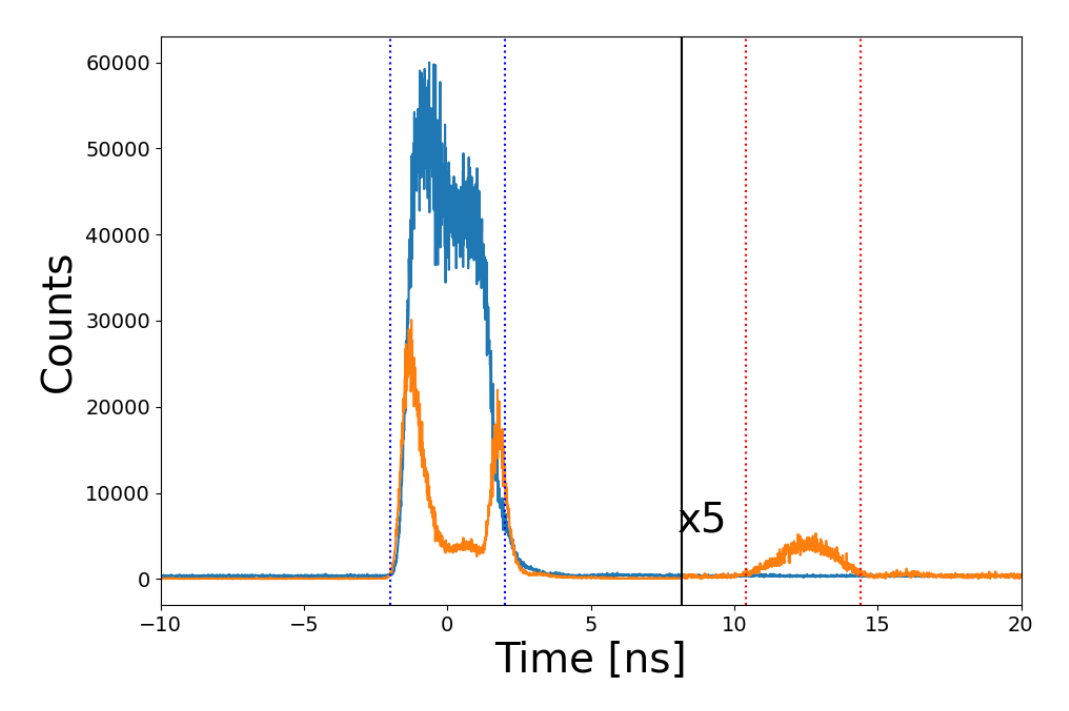


FIGURE 5.12: AFC storage in F = 1 ground state, all data pass the black line has a x5 multiplier for to ease of viewing

of 72.22  $\pm$  0.04 % and a total efficiency of 1.42  $\pm$  0.003 %, this total efficiency is equivalent to a similar comb separation (and therefore storage time) in the usual F = 2 ground state.

As stated previously the upper limit for the storage time in the excited state lifetime, and the shortest storage for the memory is defined by the separation of the exited states. As the excited states allowed from the F=2 ground state have a larger separation than those from the F=1 state, this a shorter minimum storage time and therefore a higher maximum total efficiency for the memory. Whereas the benefit for using the F=1 ground state is that the F=1 - F'=1 and the F=1 - F'=1 transitions have the same relative strength to each other leading to a more uniform AFC structure.

# 5.6 Summary

This chapter proves that the warm vapour  $^{87}$ Rb AFC memory is compatible with single-photon level and below inputs. Operating at the single-photon level also provides a further insight into the operation of the memory, such as determining the SNR of the memory, optimising the input pulse width, finding the single photon limit and testing the F = 1 ground state. These are all key steps in fully realising and optimising the memory. Performing single-photon level measurements provides more

precise values for total and read-in efficiency with a maximum measured total efficiency of  $10.64\pm0.027\%$ .

These results will allow for true single-photons to be used for this memory, and in order for this memory to have wider quantum applications the qubit comparability needs to be tested, this is investigated in the next chapter of this thesis.

# **Chapter 6**

# Warm Vapour AFC: Qubit Compatibility Experiments

Chapter 5 shows that the warm <sup>87</sup>Rb vapour AFC memory is compatible with single photon level inputs; therefore, the next step in realising this memory for a quantum network is to test its qubit compatibility using a single photon level input of  $\mu \leq 1$ .

As discussed in Chapter 1, two commonly used methods for encoding information onto photons are to create polarisation and time-bin qubits. This chapter will investigate how this memory will perform with different possible qubit states and test it with weak coherent states. Single photon-level inputs will be used to test the polarisation and multimodal capabilities of the quantum memory, proving that it is compatible with its true single-photon qubit counterparts while maintaining fidelity.

# 6.1 Polarisation Dependence

Polarisation qubits are photons prepared as a linear superposition of two orthogonal polarisation states. An example of a wavefunction for a qubit polarised in the Horizontal and Vertical plane is represented by the following:

$$|\Psi\rangle = \alpha |H\rangle + \beta |V\rangle \tag{6.1}$$

Where  $\alpha$  and  $\beta$  are complex coefficients.

To make fidelity measurements of an arbitrary polarisation qubit, one needs to make six measurements of 3 polarisation pairs: Horizontal ( $|H\rangle$ ) and Vertical ( $|V\rangle$ ), Diagonal ( $|D\rangle$ ) and Anti-diagonal ( $|A\rangle$ ) and finally Left-hand circular ( $|L\rangle$ ) and Right-hand circular ( $|R\rangle$ ). These are three sets of mutually orthogonal states: H and V, D and A, L

and R. These can be visualised using a Poincaré sphere representation, see Fig 1.4. With those six measurements, one can determine the complex amplitudes  $\alpha$  and  $\beta$ . Thus, the qubit state can be represented as a vector starting from the centre of the Poincaré sphere and stretching to the surface. To determine the state of an input photon with fewer measurements, one can measure one of the polarisation state pairs (e.g.  $|H\rangle$  and  $|V\rangle$ ) to determine the total photon number. One can then measure D or L, as D is orthogonal to A. Measuring D, one can infer A by comparing it to the total photon number measured from H and V. This is the same case for R being inferred from L. Therefore, the input polarisation state can be determined from four measurements (H, V, D and L). This assumes that the qubit's photon number does not change between measurements and that the efficiency is the same for all polarisations when storing and recalling the qubit from memory.

Two aspects must be considered to achieve high-fidelity storage of these polarisation qubits. The first is that the total efficiency is constant for all polarisations. The other is that the phase coherence of the qubit is preserved, and  $\alpha$  and  $\beta$  are preserved. The measurements above only confirm the former. If there is a strong polarisation dependence, one can infer which polarisation state has been stored within the memory. This will modify the qubit state, causing the output state to lower fidelity with respect to the input.

### 6.1.1 Experimental setup

The modified experimental setup for this investigation can be seen in Fig 6.1; the new editions are two sets of polarisers and Quarter Wave Plates (QWP). The green region is for correcting the polarisation before memory (after the fibre) to maximise the transmission through the blue region; this is needed as the fibre itself can change the polarisation of the light propagating through. The blue area is used to create the polarisation input state before the cell, and the orange area is used to measure the polarisation after the cell to determine if the memory operation changes the polarisation of the light.

To create the input polarisation states, the following settings for the Polariser (P1) and Quarter (QWP) waveplate will be used; see the table below:

Polarisation	P1 [°]	λ/4 [°]	
$ H\rangle$	90	0	
$ V\rangle$	0	0	
$ D\rangle$	45	45	
$ A\rangle$	315	45	
$ L\rangle$	45	0	
$ R\rangle$	315	0	

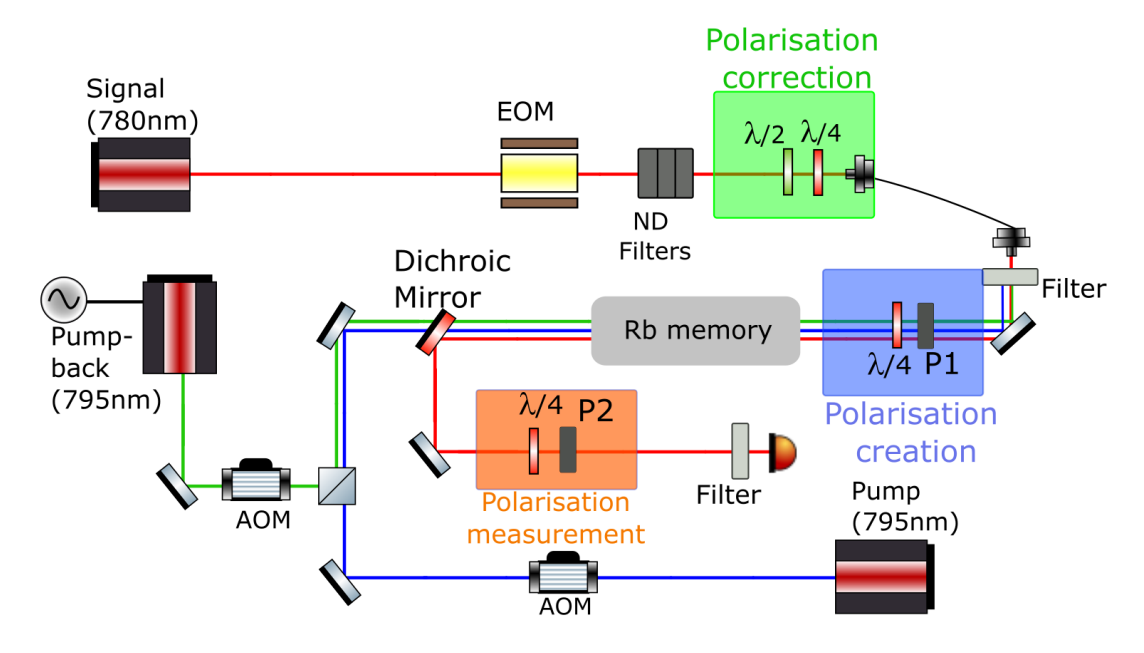


FIGURE 6.1: Simplified experimental setup for polarisation dependence. AOM - Acousto-optical modulator, EOM - Electro-optic modulator, ND - neutral density filters, P1, P2 - polarisers, the filters are used to block leakage from the pump and pump-back lasers (these are BH780-10, Semrock LL01-780-25)

These optics are mounted in indexed rotation mounts, with the P1s polarisation axis mounted to align with 0 degrees on the rotation mount, i.e., perpendicular to the optical table, and the fast axis of the quarter waveplate also mounted to align with 0 degrees. To confirm that these states were created correctly, a second polariser (P2) was placed after the polarisation creation, for the V polarised light P2 was rotated from 0° to 90° where the transmission through P2 changed from maximum to minimum but remained constant with when D, A, R or L was prepared. Introducing a second QWP will convert the circular light to linear, and then rotating P2 will show the power changing from max to min. This was the same case when these new optics were moved to after the cell; this tells us that the memory is not changing the polarisation of the light, see the orange region in Fig 6.1.

### 6.1.2 Results

Fig 6.2 shows the total efficiency for the different input polarisation states stated previously, the approach for performing this experiment was to rotate the polarisers and quarter-wave plates in the green and blue regions of Fig 6.1 following table 6.1.1 and record the histograms for each input state.

As the error bars for each polarisation state captures the errors of every other polarisation state, we can conclude that the total efficiency of the AFC storage does not depend on the input polarisation of the light. The average SNR of these data points is  $27.17 \pm 0.56$ ; as this SNR is greater than one, the upper limit of this fidelity

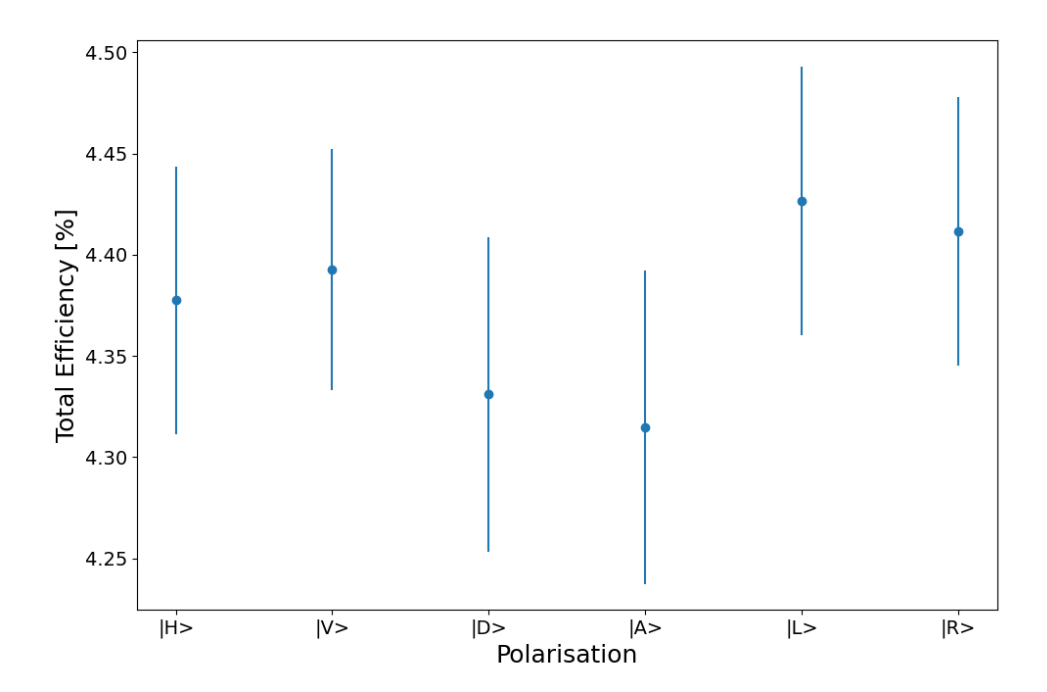


FIGURE 6.2: Polarisation state vs total Efficiency

will be F = (SNR + 1)/(SNR + 2) = 0.966. If true single photons were used, this value is different for the  $\mu$  used in this experiment. Therefore, this memory can store polarisation qubits while maintaining the fidelity of the qubit.

# 6.2 Temporal Multi-modality

Multi-modality is storing and recalling different time bins in the memory before either of them are recalled. Storing two distinct time-bins allows the memory to store time-bin qubits, i.e. arbitrary linear superpositions of the basis states defined by the two time-bins, as discussed in Chapter 1.

One criterion for memory compatibility is that memory efficiency must be identical across time bins. As mentioned above, there are ultimately two requirements: one is efficiency, and the other is that the phase coherence between the two-time bins needs to be preserved.

One way to create time-bin qubits is to inject them into an unbalanced Mach-Zehnder interferometer (see Fig 1.2 in Chapter 1 for complete details on this) where one path is longer than another by the time-bin separation and with a means to change the relative phase difference between these two paths. For the experiments in this chapter, the two pulses are created using an EOM, and the phase between the pulses cannot be arbitrarily changed.

This means that the photon will arrive at the memory Early ( $|E\rangle$ ) or Late ( $|L\rangle$ ), giving the wavefunction:

$$\Psi = \alpha |E\rangle + \beta |L\rangle \tag{6.2}$$

The experimental setup is the same as described in the previous chapter (Fig 5.1) but with the ND filter before the memory.

### 6.2.1 Results

The pulses are created with an EOM and a programmable pulse generator (ppg645) as discussed in Chapter 3, to fit multiple pulses before the recalled time the width of the pulses was reduced, see Fig 6.3, from  $T_{width} = 1.78$ ns to  $T_{width} = 0.76$ ns. These pulses had a time-bin separation of 3ns.

This was demonstrated with an average photon number of  $\mu = 0.19 \pm 0.0002$  over the two pulses, and therefore,  $\mu$  for an individual pulse is 0.095. In the Figure, the red dotted line shows the read-in and recall regions for the first pulse, and the blue dotted line is for the second pulse. These regions are used to calculate the efficiencies of this memory.

These two new pulses (Early and Late) are being stored and recalled with a total efficiency of 2.22  $\pm$  0.077 % and 2.12  $\pm$  0.078 % respectively and an SNR of 0.97  $\pm$  0.049 and 0.96  $\pm$  0.049. The values for SNR are lower than expected, this could be due to normal experimental day-to-day changes that could be increasing the noise floor of the memory.

While these total efficiencies are comparable, they are less than those previously demonstrated with the longer input pulse. The cause of this reduction in efficiency is due to these pulses having a much larger bandwidth, 1.32GHz, compared to 0.56GHz previously. Therefore, these new shorter pulses have a larger bandwidth than the total frequency range of the AFC structure (1GHz), resulting in less of the input signal being absorbed by the atoms in the AFC; this can be seen in Fig 6.3 on the height of the transmitted AFC pulse. The longer input pulses have a read-in efficiency of around 70%, whereas these shorter ones only have around 46% read-in efficiency.

A pulse with a typical width ( $T_{b2b} = 1.78$ ns) was also stored for a direct comparison for this given AFC. This AFC had a total efficiency of  $3.14 \pm 0.045$  % and a read-in efficiency of 82.65 + /-0.53 % and an SNR =  $1 \pm 0.013$ , meaning that the SNR is comparable for one pulse and two but less than the values for SNR measured in previous experiments which have measured values of SNR at around 7 in Chapter 5.

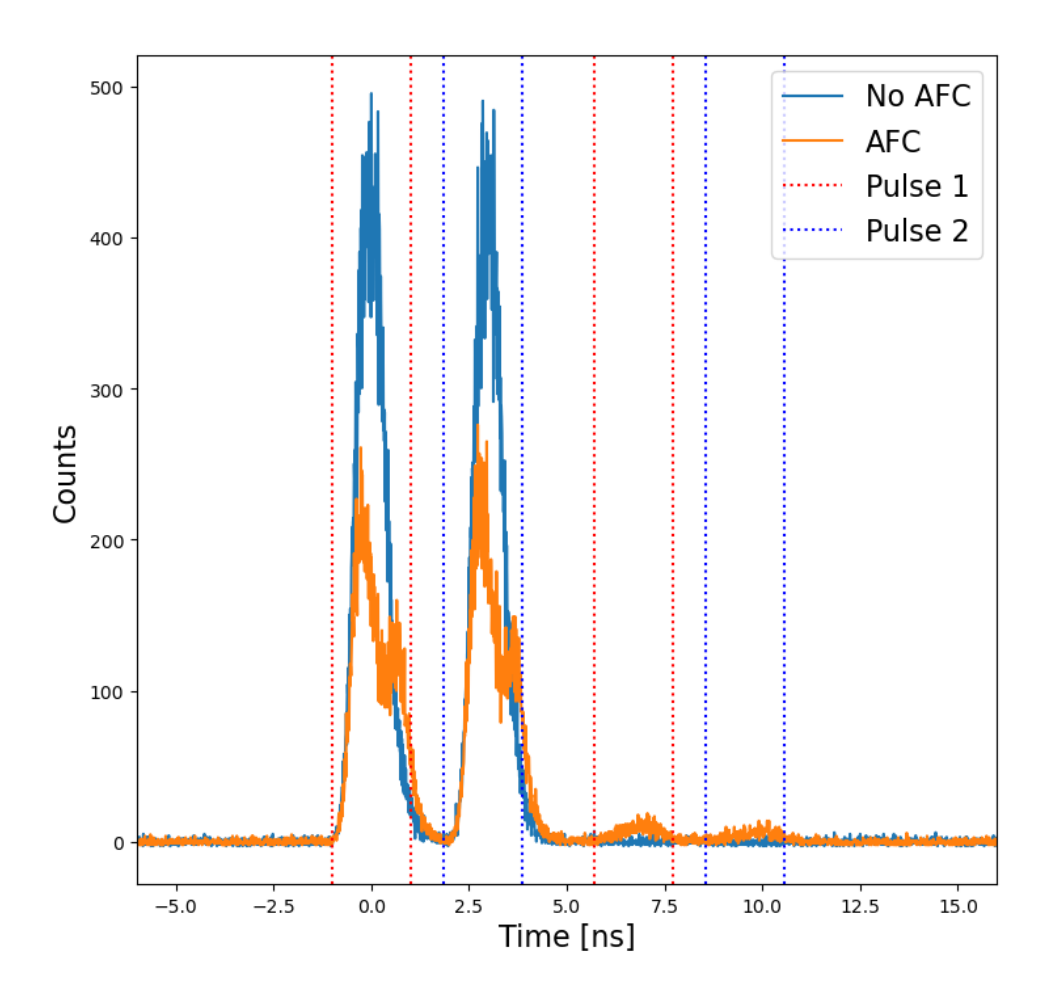


FIGURE 6.3: Multi-modality demonstration. Two pulses with a duration of 0.76 ns are stored for 7 ns each.

As the total efficiencies of the two stored pulses lie within each other's error range, it's concluded that there is no temporal dependence on the pulses stored within the memory. Although the SNR is less than one, the maximum fidelity is still above the classical limit (2/3); thus, the memory in its current configuration cannot be used to store time-bin qubits with high fidelity. This SNR needs to be improved for this memory to store time-bin qubits.

To perform projective measurements to the time-bin qubits, another unbalanced Mach-Zehnder interferometer with a path difference equal to the time-bin separation is required after the memory. This UMZI needs to change the relative phase difference between the paths so the early and late bins can go from constructively to destructively interfering.

### 6.3 Summary

This chapter shows the total efficiency of the memory is independent of input polarisation and temporal positions, this allows these basis states to be stored and recalled with the same efficiency. Projective measurements in both the polarisation and time-bin measurements remain to be performed to ensure the coherence between basis states is maintained for high fidelity. The polarisation dependence results also shows that there is a theoretical fidelity that is above the classical limit for true single photon inputs, justifying these qubits to be used to test this memory protocol in order to find the true fidelity. This is a crucial step in realising this memory for quantum applications. In order to do this, a true single photon source is required and is therefore out of the scope of this thesis.

Due to the noise of the memory (caused by the EOM), the compatibility of the time-bin qubit - although it does not depend on efficiency - gives a theoretical fidelity that is below the classical limit, indicating that these cannot be used for further quantum applications. As the SNR will be reduced if true single photons are used, this should give a fidelity above the classical limit, due to this being a prediction it will need to be verified with a true single photon source.

This chapter provided the first insight into using true single photons for the AFC memory in the warm <sup>87</sup>Rb platform. These results form the foundation for further research into this memory using encoded single photons from a source. This is crucial in fully realising a quantum network with this protocol.

# Chapter 7

# **Conclusions**

### 7.1 Summary

This thesis has provided a view into the quantum technological landscape and justified using quantum memories in realising key technologies such as quantum networks and photonic quantum computers. Chapter 1 has outlined these technologies, focusing on the criteria for building a quantum memory, along with a look into the current memory protocols and platforms used to realise them.

Chapter 2 is a detailed description of the AFC protocol outlining the advantages and applications for this protocol along with a comprehensive view into the current state-of-the-art of the protocol. Chapter 3 described the methods for implementing the AFC protocol into the warm Rb vapour platform. This includes the complete experimental diagram used throughout this thesis. Alongside the velocity selective pumping method, which forms the base for the AFC protocol, it is to be used to improve the storage time of the ORCA protocol in warm Rb vapour. Chapter 4 includes the AFC experiments for storing and retrieving high-power optical pulses. The CW and pulsed pumping regimes were compared, and investigations into the temperature and detuning dependence were carried out to further the understanding of the protocol. The pulsed regime allowed for the diffusion lifetime of the memory to be found and compared to the velocity of the atoms through the pumping regions determined by the ideal gas law. This thesis demonstrated storage time of 7ns with an end-to-end efficiency of 6.328 % Chapter 5 proves that the AFC memory can be used with single-photon level inputs. This allowed for the signal-to-noise ratio to be found alongside the single-photon limit. The single photon detectors also allowed for the measurement of longer storage times of the protocol, and the 1/e lifetime of the memory was found to be  $\tau$  = 2.898ns. The final chapter (6) demonstrated that the memory can be used with time-bin and polarisation qubits, which can lead to fidelity measurements being made for this protocol.

In conclusion, all of these results form the perfect baseline for further experiments on this protocol to either improve some of its issues (short storage time, for example) or integrate it with other experiments being carried out within the HQNL research group (quantum dot photon source). This avenue can be taken by another PhD student or by a dedicated post-doc.

### 7.2 Continuation of research

Now that the memory has been proven to be compatible with single-photon level inputs (Chapter 5) and can likely accept different potential qubit states without breaking the fidelity (Chapter 6), the next step would be to integrate this memory with a true single-photon source.

This is easier said than done, at QDs are grown within a large sample there is a large range of variance within the different dots. Therefore, finding a dot that produces a photon with a frequency that is resonant with the strongest tooth within the AFC created at various points in this thesis.

There is also a possibility of extending the storage time of this protocol by introducing a magnetic field to lift the degeneracy of the ground states already used in the protocol. This would map the collective excitation created by storing light in the memory into one of these longer-lived ground states. This would require more lasers and selection rules to map into the correct ground state. While this could push the storage time to new limits, the upper limit is still defined by the transit time of the atoms across the cross section of the lasers - this was calculated to be  $1.53\mu$ s in chapter 4. This magnetic field will also change the excited states of  $^{87}Rb$ , this could lead to a cleaner AFC structure with less overlap between the combs giving a larger memory efficiency but only if the magnetic field is well controlled.

This experiment will continue within the HQNL group as they move departments from Physics and Astronomy to the ORC; this will involve this warm vapour AFC experiment being transferred to a portable breadboard in a one laser AFC configuration; details on this can be seen in Appendix A. This breadboard approach will separate the laser sources (Signal, pump, and pump-back) on different breadboards to the memory. Each of these will have fibre inputs and outputs. This will allow the experiment to be transported from one lab to another and will allow for the easy introduction of a single-photon source.

# Appendix A

# **AppendixA**

### A.1 Hybrid Quantum Networks Lab

HQNL aims to integrate quantum memories with single-photon sources to create a full-functioning quantum network. Several avenues of research contribute to fully realising this goal. The first is the warm vapour quantum memory based on the AFC protocol in Rubidium-87 vapour. This is the research project on which this thesis is based. The project led by Dr Ori Mor is to create an AFC memory in the Rare-Earth Ion-Doped (REIDs) platform. Using a REIDS crystal, this is a quantum memory at cryogenic temperatures (3k). This protocol uses a 606nm signal laser to store single photon level inputs; the AFC is created using spectral hole burning rather than the pump and pump-back techniques used in this thesis. The next avenue of research for HQNL is the building of a quantum dot single photon source to be resonant with the warm Rb-87 vapour AFC memory. Therefore, this dot's aim is to have an output photon of 780nm. Dr Vanderli Laurindo Junior is carrying out this project.

### A.1.1 Founding of HQNL

HQNL was founded in March 2020 by Dr Patrick M Ledingham (PML). PML was a senior postdoc in the Ultrafast Quantum Optics group at Oxford University from 2014 to 2020, working on quantum memories in the warm vapour platform.

I joined the research group in October 2020 and began my research project with it. At the time of my arrival, the group consisted of myself, PML, and Oliver Green, a year-in-research MPhys student working on an Autler-Townes splitting quantum memory. During Oliver's time at HQNL, we shared a lab space and most of our equipment, running our project in tandem. As this was a newly founded research group, not to mention its founding during the Coronavirus pandemic, the lab space in

room 2020 of building 46 on Southampton University's Highfield campus was empty upon my arrival to the research group. See Fig A.1 for a picture of the Lab before my first day in HQNL. Therefore, most of my first year was spent building the infrastructure of the experiment from the ground up. This led to some sub-optimal design choices within the experiment, which led to a rather messy optical table and inefficient use of space both on and above said optical table. This can be seen in Fig A.2, which are pictures of my final experiment in the lab and the complete experimental setup in Fig 3.3.

Dr Ori Mor and Dr Vanderli Laurindo Junior joined the group in August 2022 and September 2022, respectively. While they had their own projects consuming their time and effort, they provided a great deal of mentorship and help in the construction and operation of my experiment, as well as insightful discussion on the results of my experiments.

Another MPhys student, Alice Christian-Edwards, joined the group during the 2022/2023 academic year. This project was based on making a quantum memory that had a backwards recalled signal pulse based on the Doppler Rephased Echo (DRE) protocol. Alice also worked in Lab2020 and shared my optical table and a large amount of equipment, as we both worked on the same platform, which required lasers of the same wavelength. While this lab share meant less time dedicated to the warm vapour AFC experiment, it allowed more time to analyse the results and broaden my understanding of the research topic.

As HQNL was a new research group, our early equipment consisted of newly bought and old equipment 'borrowed' from various places; for example, we had a few AOMs on loan from the ICL. The process of buying the needed equipment and the lead time associated with it led to a few too many occasions when progress in the experiment had to be halted.

### A.1.2 COVID-19

As mentioned, I joined HQNL and began this research project in October 2020 during the COVID-19 pandemic. This caused a non-traditional start to my PhD; for example, while still allowing access to the lab, the university's COVID policy limited the number of people in our lab space to 1. This made the task of building an experiment from scratch by oneself rather daunting. With only Microsoft Teams as a communication tool, the early stages of my PhD were slower than one should expect, and the fallout of this was felt throughout my entire PhD. These restrictions were lifted, and a regular lab schedule and experimental progression were achieved. However, the worry of another national lockdown removing our access to the lab led us to implement a remote control aspect to the experiment. However, the fear of



FIGURE A.1: Lab 2020, Dated October 2020

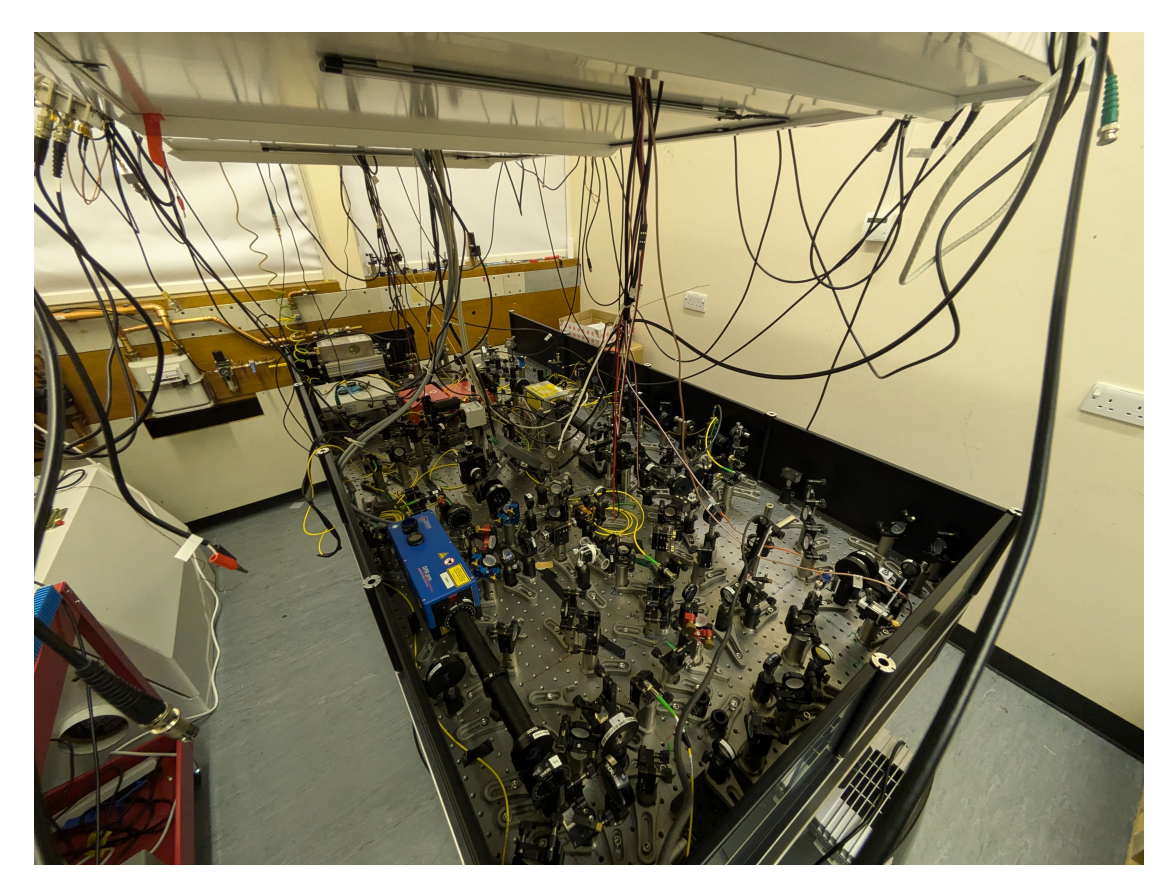


FIGURE A.2: Lab 2024, Dated October 2024

another national lockdown removing our access to the lab led to most parts of the experiment being remotely controlled from outside the building, except for the alignment of mirrors. The idea of motorised mirrors was proposed at some point; this would have allowed the whole experiment to be controlled remotely and increased the safety of operating the experiment from inside the room. Ultimately, this was too expensive of an avenue to implement into the setup. Luckily for HQNL, no such large-scale lockdown was ever reintroduced.

### A.1.3 Moving to the Opto-Electronics Research Centre

As of the end of 2024, HQNL will be moving to the ORC. This will lead to the dismantling and relocation of Lab 2020 and my entire experiment inside. This is when the experiment will be changed to a breadboard configuration, as mentioned in Chapter 7. As this happens during my nominal stage, the experiment no longer exists for me to retake data or perform extra experiments. As it currently stands, no new PhD students or Postdocs are employed to rebuild the experiment. Even if these positions are filled, it is unlikely that the experiment will be functional as this thesis is submitted.

### A.2 One Laser AFC

At the beginning of 2024, the pump-back laser (Toptica DFB) malfunctioned, halting the progress of this experiment. After lengthy troubleshooting, the laser was sent back to the manufacturer (Toptica Photonics)

While this laser was being serviced, a new experimental regime had to be introduced. The solution was to use one laser for both the pump and pump-back roles in the AFC experiment.

There are some benefits to this approach compared to the previous experiment. Using one laser for all the pumping means that the pumps have a consistent phase. Experimental simplicity also increases, with the overall experiment having a smaller footprint on the optical table as fewer optics are used.

### A.2.1 New Experimental Setup

To address both ground states, the new pumping laser needs to be modulated by 6.834GHz, which is the ground state separation of Rb87 (see Fig 3.1), as well as being modulated by 133MHz to create the AFC structure. Previously, this modulation was provided by an AWG; this device is unable to produce a modulation as large as

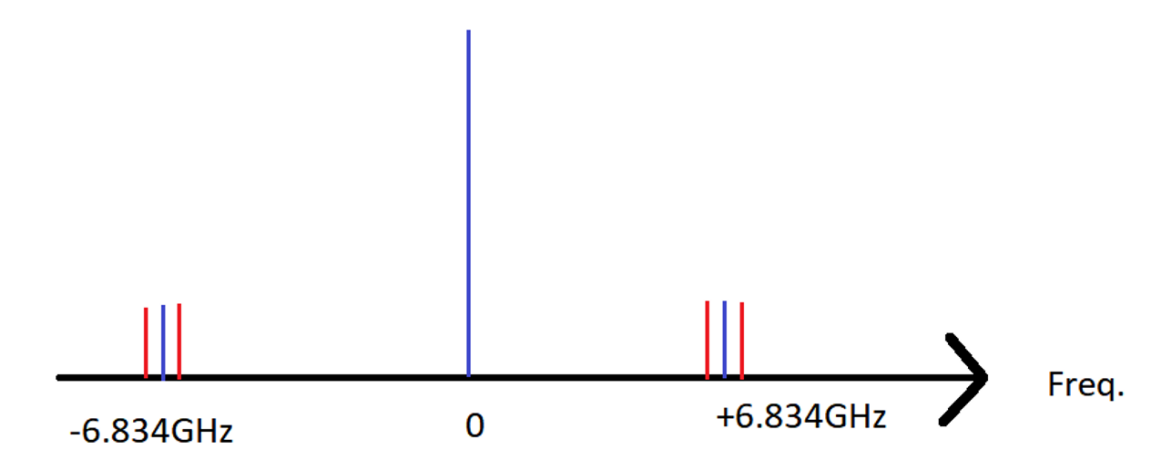


FIGURE A.3: Frequency modulation for one laser AFC

 $6.834 \mathrm{GHz}$ ; therefore, a Pciosynth local oscillator along with a phase EOM was used to create this frequency; the pump laser frequency is still resonant with the F = 1 ground state, and the modulation sidebands act as the pump-back resonant with the F = 2 ground state. The amplitude of this modulation can be controlled to change the power of the  $6.834 \mathrm{GHz}$  sidebands, optimising the AFC structure for the best AFC memory efficiency. The pump-back modulation (133MHZ) was created using the AWG in the same way mentioned in previous experiments. The combined frequency modulation profile can be seen in Fig A.3.

To create the AFC with one laser, these modulation frequencies must be combined before the phase EOM; this was done with a frequency mixer (zx05-153-s+). As this process was inefficient, the output from the mixer needed to be amplified with an RF amplifier (DR-AN-10-MO) so that strong enough sidebands could be created. This RF circuit can be seen in Fig A.4. The RF power was measured using a ZX47-40-S+ power meter.

The AFC structure created from this new one laser AFC approach can be seen in Fig A.5, the orange trace is the one laser AFC, and the blue trace is a previous 'two laser AFC' that was taken from an earlier experiment. It can be seen that the one-laser AFC would give a lower total efficiency due to the less well-defined teeth. These teeth have a larger width than the two-laser approach, and there is a larger background.

The main reason for this is that the seed laser for this 'one laser AFC' spectrum has a larger line width than the pump-back laser used previously in this thesis; therefore, the width of these AFC teeth reflects this larger line width.

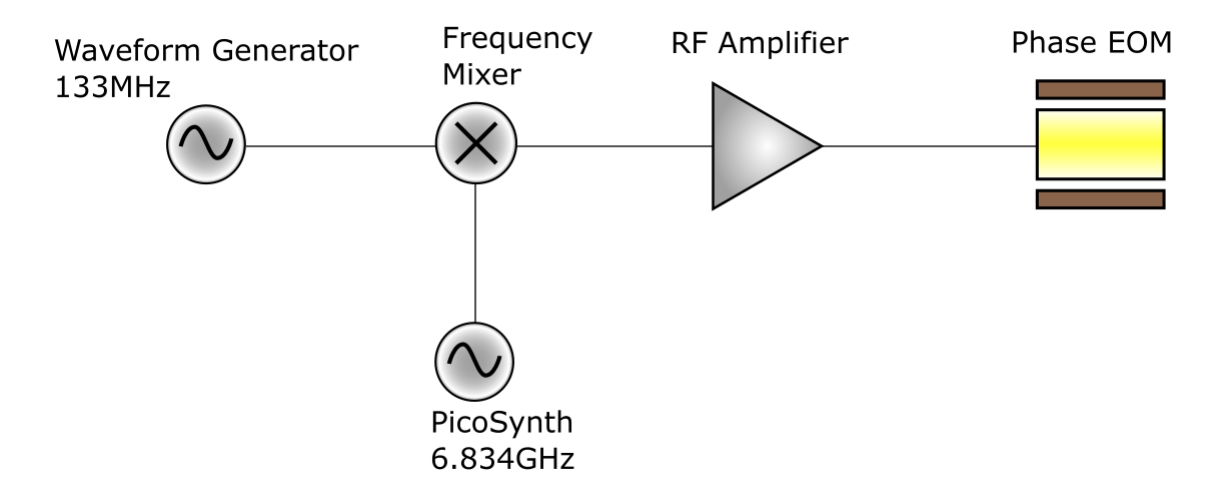


FIGURE A.4: RF mixing setup

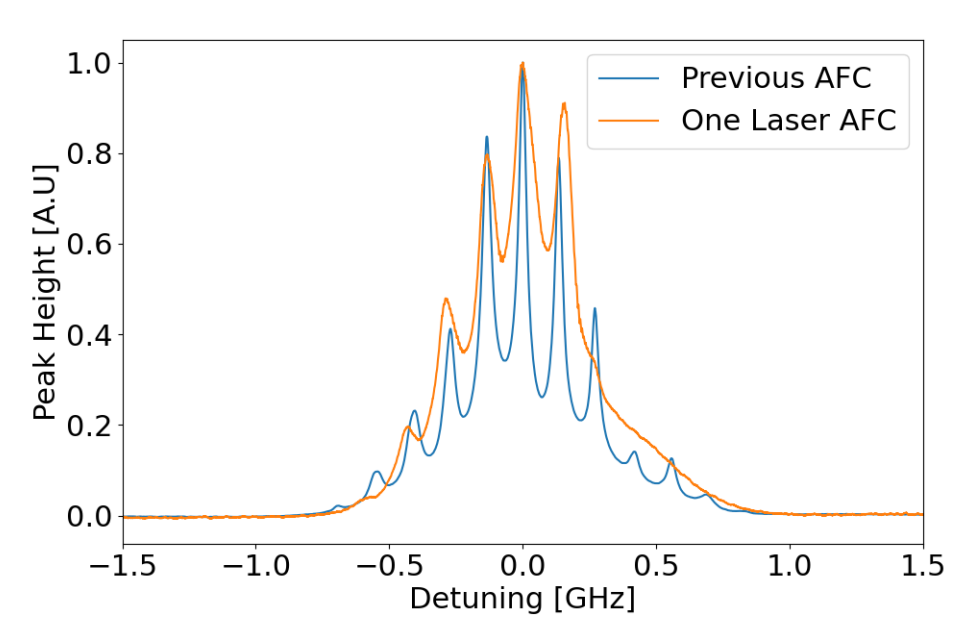


FIGURE A.5: One laser vs two laser AFC spectra comparison

### A.2.2 Results

Fig A.6 shows the storage and retrieval of an input pulse for the one laser AFC structure made in Fig A.5, with a read-in efficiency  $\eta_{read_in} = 49.01\%$  and total efficiency of  $\eta_{total} = 1.77\%$ . This is lower than the two laser efficiency as predicted.

Another issue with the seed laser used for the one laser AFC is that the current driver has imprecise control over the current and, therefore, the frequency of the laser, making it hard to account for drift and, therefore, making longer experimental integration times difficult to perform.

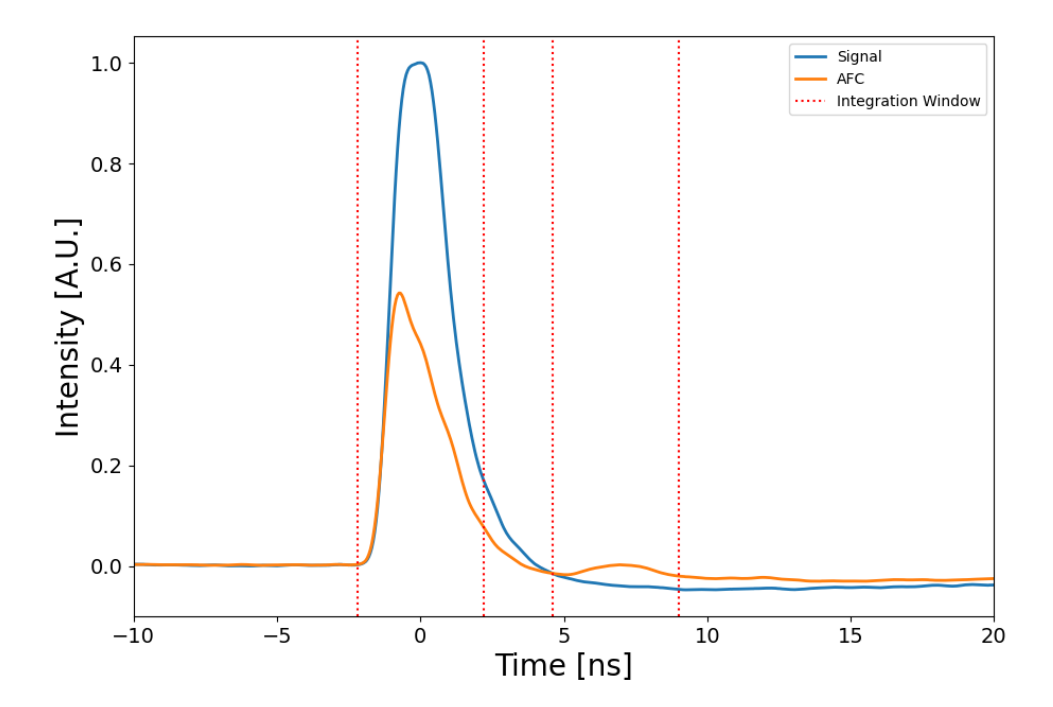


FIGURE A.6: One laser AFC storage

### A.2.3 Summary

The one-laser AFC approach in this configuration is less efficient than the previously demonstrated two-laser approach due to the nature of the seed laser used. Therefore, switching to the Toptica DFB laser should give an AFC of similar width to the two-laser AFC case while providing the benefits mentioned before of the one-laser AFC case. The future of this experiment is to use this laser to create the AFC on a breadboard configuration.

### A.3 Publications and contributions

### A.3.1 Publications

S.E. Thomas, S. Sagona-Stophel, Z. Schofield, I.A. Walmsley, and P.M. Ledingham. Single-photon-compatible telecommunications-band quantum memory in a hot atomic gas. *Phys. Rev. Appl.*, 19:L031005, Mar 2023

### A.3.1.1 Future publications

The work from this thesis will produce a paper of the same title: Single-Photon-Level Warm Rubidium AFC Quantum Memory Co-authored by Alice Christian-Edwards<sup>1,2</sup>, Vanderli Laurindo Jr<sup>1,2</sup>, Ori Mor<sup>1,2</sup>, P. M. Ledingham<sup>1,2</sup>

1. Department of Physics and Astronomy, University of Southampton, Southampton SO17 1BJ, UK 2. Optoelectronics Research Centre, University of Southampton, Southampton SO17 1BJ, UK

### A.3.2 Conference contributions

- YAO 2023 Barcelona Poster: 'Atomic Frequency Comb Memory in Warm Rubidium Vapour'
- Cleo 2023 Munich Poster: 'Atomic Frequency Comb Memory in Warm Rubidium Vapour'
- YAO 2024 Strasbourg Talk: 'Room temperature Quantum Memory for light using the Atomic Frequency Comb protocol'

# References

- [1] S.E. Thomas, S. Sagona-Stophel, Z. Schofield, I.A. Walmsley, and P.M. Ledingham. Single-photon-compatible telecommunications-band quantum memory in a hot atomic gas. *Phys. Rev. Appl.*, 19:L031005, Mar 2023.
- [2] Peter W. Shor. Fault-tolerant quantum computation, 1997.
- [3] Vicente Martin, Juan Pedro Brito, Carmen Escribano, Marco Menchetti, Catherine White, Andrew Lord, Felix Wissel, Matthias Gunkel, Paulette Gavignet, Naveena Genay, Olivier Le Moult, Carlos Abellán, Antonio Manzalini, Antonio Pastor-Perales, Victor López, and Diego López. Quantum technologies in the telecommunications industry. *EPJ Quantum Technology*, 8(1), July 2021.
- [4] I. M. Georgescu, S. Ashhab, and Franco Nori. Quantum simulation. *Rev. Mod. Phys.*, 86:153–185, Mar 2014.
- [5] C.L. Degen, F. Reinhard, and P. Cappellaro. Quantum sensing. *Reviews of Modern Physics*, 89(3), July 2017.
- [6] Valerio Scarani, Helle Bechmann-Pasquinucci, Nicolas J. Cerf, Miloslav Dušek, Norbert Lütkenhaus, and Momtchil Peev. The security of practical quantum key distribution. *Rev. Mod. Phys.*, 81:1301–1350, Sep 2009.
- [7] Raffaele et al. Santagati. Drug design on quantum computers. *Nature Physics*, 20(4):549–557, March 2024.
- [8] Karthik Srinivasan, Saipriya Satyajit, Bikash K. Behera, and Prasanta K. Panigrahi. Efficient quantum algorithm for solving travelling salesman problem: An ibm quantum experience, 2018.
- [9] P.W. Shor. Algorithms for quantum computation: discrete logarithms and factoring. In *Proceedings 35th Annual Symposium on Foundations of Computer Science*, pages 124–134, 1994.
- [10] Vittorio Giovannetti, Seth Lloyd, and Lorenzo Maccone. Quantum metrology. *Phys. Rev. Lett.*, 96:010401, Jan 2006.

- [11] Innovation Department for Science and Technology. National quantum strategy, 2023. https:
  - //www.gov.uk/government/publications/national-quantum-strategy [Accessed: 23/11/2024].
- [12] Charles H. Bennett and Gilles Brassard. Quantum cryptography: Public key distribution and coin tossing. *Theoretical Computer Science*, 560:7–11, December 1984.
- [13] Zurek W Wootters, W. A single quantum cannot be cloned. *Nature*, pages 802 803, 1982.
- [14] Koji Azuma, Sophia E. Economou, David Elkouss, Paul Hilaire, Liang Jiang, Hoi-Kwong Lo, and Ilan Tzitrin. Quantum repeaters: From quantum networks to the quantum internet. *Reviews of Modern Physics*, 95(4), December 2023.
- [15] Qiang Zhang, Feihu Xu, Yu-Ao Chen, Cheng-Zhi Peng, and Jian-Wei Pan. Large scale quantum key distribution: challenges and solutions. *Opt. Express*, 26(18):24260–24273, Sep 2018.
- [16] Ivan Capraro, Andrea Tomaello, Alberto Dall'Arche, Francesca Gerlin, Ruper Ursin, Giuseppe Vallone, and Paolo Villoresi. Impact of turbulence in long range quantum and classical communications. *Physical Review Letters*, 109(20), November 2012.
- [17] Mustafa Gündoğan, Jasminder S. Sidhu, Victoria Henderson, Luca Mazzarella, Janik Wolters, Daniel K. L. Oi, and Markus Krutzik. Proposal for space-borne quantum memories for global quantum networking. *npj Quantum Information*, 7(1), August 2021.
- [18] Yuexun Huang, Francisco Salces-Carcoba, Rana X. Adhikari, Amir H. Safavi-Naeini, and Liang Jiang. Vacuum beam guide for large scale quantum networks. *Phys. Rev. Lett.*, 133:020801, Jul 2024.
- [19] B.P. Abbott et al. Observation of gravitational waves from a binary black hole merger. *Phys. Rev. Lett.*, 116:061102, Feb 2016.
- [20] M. Pompili, S. L. N. Hermans, S. Baier, H. K. C. Beukers, P. C. Humphreys, R. N. Schouten, R. F. L. Vermeulen, M. J. Tiggelman, L. dos Santos Martins, B. Dirkse, S. Wehner, and R. Hanson. Realization of a multinode quantum network of remote solid-state qubits. *Science*, 372(6539):259–264, April 2021.
- [21] Jian-Long Liu, Xi-Yu Luo, Yong Yu, Chao-Yang Wang, Bin Wang, Yi Hu, Jun Li, Ming-Yang Zheng, Bo Yao, Zi Yan, Da Teng, Jin-Wei Jiang, Xiao-Bing Liu, Xiu-Ping Xie, Jun Zhang, Qing-He Mao, Xiao Jiang, Qiang Zhang, Xiao-Hui Bao, and Jian-Wei Pan. Creation of memory–memory entanglement in a metropolitan quantum network. *Nature*, 629(8012):579–585, May 2024.

- [22] Vittorio Giovannetti, Seth Lloyd, and Lorenzo Maccone. Advances in quantum metrology. *Nature Photonics*, 5(4):222–229, March 2011.
- [23] Michael A. Taylor and Warwick P. Bowen. Quantum metrology and its application in biology, 2015.
- [24] D. F. Walls and G. J. Milburn. Quantum Optics. Springer, 2nd edition, 2008.
- [25] SONGTAO HUANG TAXUE MA FANG LIU HIDEHIRO YONEZAWA YONG ZHANG CHUAN XU, LIDAN ZHANG and MIN XIAO. Sensing and tracking enhanced by quantum squeezing. *Photon. Res.* 7, A14-A26, 2019.
- [26] Lijun Xu Jianguo Ma, Xiangdong Ma. Optical ultrasound sensing for biomedical imaging. *Measurement*, 200, 2022.
- [27] David E. McClelland Ping K. Lam Roman Schnabel, Nergis Mavalvala. Quantum metrology for gravitational wave astronomy. *Nature Communications*, 1:121, November 2010.
- [28] Hamish Johnston. A quantum accelerometer is being built for navy submarines, 2014. https://physicsworld.com/a/a-quantum-accelerometer-is-being-built-for-navy-submarines/[Accessed: 04/10/2024].
- [29] Pierrick Cheiney, Brynle Barrett, Simon Templier, Olivier Jolly, Baptiste Battelier, Philippe Bouyer, Henri Porte, and Fabien Napolitano. Demonstration of a robust hybrid classical/quantum accelerometer. In 2019 IEEE International Symposium on Inertial Sensors and Systems (INERTIAL), pages 1–4, 2019.
- [30] Pierrick Cheiney, Lauriane Fouché, Simon Templier, Fabien Napolitano, Baptiste Battelier, Philippe Bouyer, and Brynle Barrett. Navigation-compatible hybrid quantum accelerometer using a kalman filter. *Phys. Rev. Appl.*, 10:034030, Sep 2018.
- [31] classiq. Interference in quantum computing, 2022. https://www.classiq.io/insights/interference-in-quantum-computing [Accessed: 27/05/2025].
- [32] David P. DiVincenzo. The physical implementation of quantum computation. *Fortschritte der Physik*, 48(9–11):771–783, September 2000.
- [33] A. K. Fedorov, N. Gisin, S. M. Beloussov, and A. I. Lvovsky. Quantum computing at the quantum advantage threshold: a down-to-business review, 2022.
- [34] Francesco Bernardini, Abhijit Chakraborty, and Carlos Ordóñez. Quantum computing with trapped ions: a beginner's guide, 2023.

- [35] IonQ. Atoms make better quantum computers., 2024. https://ionq.com/technology [Accessed: 20/11/2024].
- [36] Xiaoling Wu, Xinhui Liang, Yaoqi Tian, Fan Yang, Cheng Chen, Yong-Chun Liu, Meng Khoon Tey, and Li You. A concise review of rydberg atom based quantum computation and quantum simulation\*. *Chinese Physics B*, 30(2):020305, February 2021.
- [37] Levine H. Semeghini G. et al. Bluvstein, D. A quantum processor based on coherent transport of entangled atom arrays. *Nature*, 604:451–456, April 2022.
- [38] QuEra. Using neutral-atom arrays to build quantum computers, 2023. https://www.quera.com/neutral-atom-platform [Accessed: 20/11/2024].
- [39] He-Liang Huang, Dachao Wu, Daojin Fan, and Xiaobo Zhu. Superconducting quantum computing: a review. *Science China Information Sciences*, 63(8), July 2020.
- [40] Frank Arute et al. Quantum supremacy using a programmable superconducting processor. *Nature*, 574:505–510, 2019.
- [41] Google. Meet willow, our state-of-the-art quantum chip, 2024. https://blog.google/technology/research/google-willow-quantum-chip/[Accessed: 24/12/2024].
- [42] IBM. Ibm quantum computing, 2024. https://www.ibm.com/quantum [Accessed: 20/11/2024].
- [43] Intel. Quantum computing systems achieving quantum practicality, 2024. https://www.intel.com/content/www/us/en/research/quantum-computing. html?wapkw=quantum%20computing [Accessed: 20/11/2024].
- [44] IMEC. Physical qubits for quantum computing, 2024. https://www.imec-int.com/en/expertise/cmos-advanced/compute/quantum-computer [Accessed: 20/11/2024].
- [45] Sergei Slussarenko and Geoff J. Pryde. Photonic quantum information processing: A concise review. *Applied Physics Reviews*, 6(4), October 2019.
- [46] ORCA Computing. Technology, 2024. https://orcacomputing.com/technology/[Accessed: 23/11/2024].
- [47] PsiQuantum. A fast path to useful, error-corrected quantum computing, 2024. https://www.psiquantum.com/blueprint [Accessed: 24/12/2024].
- [48] Quandela. What is photonic qubit?, 2024. https://www.quandela.com/resources/quantum-computing-glossary/photonic-qubit/[Accessed: 24/12/2024].

- [49] Arun K. Majumdar. Optical Wireless Communications for Broadband Global Internet Connectivity. 2019.
- [50] Travis Humble. Quantum security for the physical layer. *IEEE Communications Magazine*, 51, 08 2013.
- [51] Wolfgang Tittel and Gregor Weihs. Photonic entanglement for fundamental tests and quantum communication. *Quantum Information and Computation*, 1, 08 2001.
- [52] J. Brendel, N. Gisin, W. Tittel, and H. Zbinden. Pulsed energy-time entangled twin-photon source for quantum communication. *Phys. Rev. Lett.*, 82:2594–2597, Mar 1999.
- [53] Frédéric Bouchard, Duncan England, Philip J. Bustard, Khabat Heshami, and Benjamin Sussman. Quantum communication with ultrafast time-bin qubits. *PRX Quantum*, 3:010332, Feb 2022.
- [54] Hsin-Pin Lo, Takuya Ikuta, Nobuyuki Matsuda, Toshimori Honjo, William J. Munro, and Hiroki Takesue. Quantum process tomography of a controlled-phase gate for time-bin qubits. *Phys. Rev. Appl.*, 13:034013, Mar 2020.
- [55] H. J. McGuinness, M. G. Raymer, C. J. McKinstrie, and S. Radic. Quantum frequency translation of single-photon states in a photonic crystal fiber. *Physical Review Letters*, 105(9), August 2010.
- [56] Nicholas A. Peters Ogaga D. Odele Daniel E. Leaird1 Andrew M. Weiner Hsuan-Hao Lu1, Joseph M. Lukens and Pavel Lougovski. Electro-optic frequency beam splitters and tritters for high-fidelity photonic quantum information processing. *Phys. Rev. Lett.*, 120, Jan 2018.
- [57] Glenn Solomon Andrew White Pascale Senellart. High-performance semiconductor quantum-dot single-photon sources. *Nature Nanotechnology*, 12:1026–1039, 2017.
- [58] Tetsuyuki Ochiai. Degenerate spontaneous parametric down-conversion in nonlinear metasurfaces, 2023.
- [59] Sungeun Oh and Thomas Jennewein. Polarization entanglement with highly non-degenerate photon pairs enhanced by effective walk-off compensation method, 2024.
- [60] W. H. Louisell, A. Yariv, and A. E. Siegman. Quantum fluctuations and noise in parametric processes. i. *Phys. Rev.*, 124:1646–1654, Dec 1961.
- [61] David C. Burnham and Donald L. Weinberg. Observation of simultaneity in parametric production of optical photon pairs. *Phys. Rev. Lett.*, 25:84–87, Jul 1970.

- [62] Yasuo Kitaoka Tomoya Sugita, Kiminori Mizuuchi and Kazuhisa Yamamoto. 31mgo:linbo3 waveguide by frequency doubling of an algaas laser diode. *Optics Letters*, 24(22), 1999.
- [63] Suman Karan, Shaurya Aarav, Homanga Bharadhwaj, Lavanya Taneja, Arinjoy De, Girish Kulkarni, Nilakantha Meher, and Anand K Jha. Phase matching in -barium borate crystals for spontaneous parametric down-conversion. *Journal of Optics*, 22(8):083501, June 2020.
- [64] Junaid S. Saravi S. et al. Afsharnia, M. Generation of infrared photon pairs by spontaneous four-wave mixing in a cs2-filled microstructured optical fiber. *Sci Rep* 14, 997, Jan 2024.
- [65] Qianni Zhang Kaiyi Wu and Andrew W. Poon. Integrated si3n4 microresonator-based quantum light sources with high brightness using a subtractive wafer-scale platform. *Opt. Express*, 29:24750–24764, 2021.
- [66] Marc Sorel Joseph C. Bayley Euan McBrearty Ross W. Millar Stefan Hild Martin Sinclair, Kevin Gallacher and Douglas J. Paul. 1.4 million q factor si3n4 micro-ring resonator at 780nm wavelength for chip-scale atomic systems. *Opt. Express* 28, (4010-4020), 2020.
- [67] P. Del'Haye, A. Schliesser, O. Arcizet, T. Wilken, R. Holzwarth, and T. J. Kippenberg. Optical frequency comb generation from a monolithic microresonator. *Nature*, 450(7173):1214–1217, December 2007.
- [68] F. Dell'Olio, T. Tatoli, C. Ciminelli, and M. Armenise. Recent advances in miniaturized optical gyroscopes. *Journal of the European Optical Society Rapid publications*, 9(0), 2014.
- [69] Ivan B. Djordjevic. *Quantum Information Processing, Quantum Computing, and Quantum Error Correction*. Academic Press, 2021.
- [70] Mark J. Holmes Yasuhiko Arakawa. Progress in quantum-dot single photon sources for quantum information technologies: A broad spectrum overview. *Appl. Phys. Rev.* 1, 7, June 2020.
- [71] Kelley Rivoire Sonia Buckley and Jelena Vučković. Engineered quantum dot single-photon sources. *Reports on Progress in Physics*,, 75:12, November 2012.
- [72] Wikipedia. Phonon, 2024. https://en.wikipedia.org/wiki/Phonon#:~:text=A%20phonon%20is%20the%20quantum,a%20normal%20mode%20of%20vibration. [Accessed: 16/12/2024].
- [73] Löbl M.C. Nguyen G.N. et al. Zhai, L. Low-noise gaas quantum dots for quantum photonics. *Nat Commun*, 11:4745, September 2020.

- [74] et al. Hélène Ollivier. Reproducibility of high-performance quantum dot single-photon sources. *ACS Photonics*, 7(4):1050–1059, March 2020.
- [75] Guo YP. Xu MC. et al Ding, X. High-efficiency single-photon source surpassing the loss-tolerance threshold for fault-tolerant quantum computing. *Nat. Photon*, (19):387 – 391, 2025.
- [76] Mikkelsen M.T. Müller R. et al Zahidy, M. Quantum key distribution using deterministic single-photon sources over a field-installed fibre link. *npj Quantum Inf*, 10(2), 2024.
- [77] J. Nunn, N. K. Langford, W. S. Kolthammer, T. F. M. Champion, M. R. Sprague, P. S. Michelberger, X.-M. Jin, D. G. England, and I. A. Walmsley. Enhancing multiphoton rates with quantum memories. *Physical Review Letters*, 110(13), March 2013.
- [78] Rodney Loudon. *The Quantum Theory of Light*. Oxford University Press, 3rd edition, 2000.
- [79] AFL. The speed of light: From nasa to fiber optics, 2022.

  https://www.aflhyperscale.com/articles/
  techsplainer-light-series-the-speed-of-light/[Accessed: 06/05/2025].
- [80] Khabat Heshami, Duncan G England, Peter C Humphreys, Philip J Bustard, Victor M Acosta, Joshua Nunn, and Benjamin J Sussman. Quantum memories: emerging applications and recent advances. *Journal of Modern Optics*, 63(20):2005–2028, 2016.
- [81] Khabat Heshami, Duncan G. England, Peter C. Humphreys, Philip J. Bustard, Victor M. Acosta, Joshua Nunn, and Benjamin J. Sussman. Quantum memories: emerging applications and recent advances. *Journal of Modern Optics*, 63(20):2005–2028, March 2016.
- [82] Jin M. Chen DL. et al. Ma, YZ. Elimination of noise in optically rephased photon echoes. *Nat Commun*, 12, July 2021.
- [83] D. J. Saunders, J. H. D. Munns, T. F. M. Champion, C. Qiu, K. T. Kaczmarek, E. Poem, P. M. Ledingham, I. A. Walmsley, and J. Nunn. Cavity-enhanced room-temperature broadband raman memory. *Phys. Rev. Lett.*, 116:090501, Mar 2016.
- [84] S. E. Thomas, T. M. Hird, J. H. D. Munns, B. Brecht, D. J. Saunders, J. Nunn, I. A. Walmsley, and P. M. Ledingham. Raman quantum memory with built-in suppression of four-wave-mixing noise. *Phys. Rev. A*, 100:033801, Sep 2019.
- [85] Richard Jozsa. Fidelity for mixed quantum states. *Journal of Modern Optics*, 41(12):2315–2323, 1994.

- [86] S. Massar and S. Popescu. Optimal extraction of information from finite quantum ensembles. *Phys. Rev. Lett.*, 74:1259–1263, Feb 1995.
- [87] Peter W. Shor. Scheme for reducing decoherence in quantum computer memory. *Phys. Rev. A*, 52:R2493–R2496, Oct 1995.
- [88] FiberLabs Inc. https://www.fiberlabs.com/glossary/optical-communication-band/, March, 2023 Date Accessed: 23/09/2024.
- [89] Mikael Afzelius, Christoph Simon, Hugues de Riedmatten, and Nicolas Gisin. Multimode quantum memory based on atomic frequency combs. *Physical Review A*, 79(5), May 2009.
- [90] B. Kraus, W. Tittel, N. Gisin, M. Nilsson, S. Kröll, and J. I. Cirac. Quantum memory for nonstationary light fields based on controlled reversible inhomogeneous broadening. *Phys. Rev. A*, 73:020302, Feb 2006.
- [91] Denis V. Vasilyev, Ivan V. Sokolov, and Eugene S. Polzik. Quantum memory for images: A quantum hologram. *Phys. Rev. A*, 77:020302, Feb 2008.
- [92] Zhan Zheng, Oxana Mishina, Nicolas Treps, and Claude Fabre. Atomic quantum memory for multimode frequency combs. *Phys. Rev. A*, 91:031802, Mar 2015.
- [93] Alexander I Lvovsky, Barry C Sanders, and Wolfgang Tittel. Optical quantum memory. *Nature Photonics*, 3(12):706–714, 2009.
- [94] Zhongwei Zhang a Jeremie Maire c Yangyu Guo a Ryoto Yanagisawa a Sebastian olz a d Masahiro Nomura a b, Roman Anufriev a. Review of thermal transport in phononic crystals. *Materials Today Physics*, 22:100613, January 2022.
- [95] ThorLabs. Vapor reference cells, 2025. ://www.thorlabs.com/newgrouppage9.cfm?objectgroup $_ID = 1470[Accessed: 07/05/2025]$ .
- [96] E. B. Alexandrov, M. V. Balabas, D. Budker, D. English, D. F. Kimball, C.-H. Li, and V. V. Yashchuk. Light-induced desorption of alkali-metal atoms from paraffin coating. *Phys. Rev. A*, 66:042903, Oct 2002.
- [97] T. F. M. Champion D. G. England J. Nunn X.-M. Jin W. S. Kolthammer A. Abdolvand P. St. J. Russell I. A. Walmsley M. R. Sprague, P. S. Michelberger. Broadband single-photon-level memory in a hollow-core photonic crystal fibre. *Nature Photonics*, 8(287–291), 2014.
- [98] Oliver Slattery Lijun Ma and Xiao Tang. Optical quantum memory based on electromagnetically induced transparency. *J. Opt. 19*, 043001, 2017.

- [99] Barry C. Sanders Alexander I. Lvovsky and Wolfgang Tittel. Optical quantum memory. *Nature Photon*, 3:706–714, 2009.
- [100] Ya-Fen Hsiao, Pin-Ju Tsai, Hung-Shiue Chen, Sheng-Xiang Lin, Chih-Chiao Hung, Chih-Hsi Lee, Yi-Hsin Chen, Yong-Fan Chen, Ite A. Yu, and Ying-Cheng Chen. Highly efficient coherent optical memory based on electromagnetically induced transparency. *Phys. Rev. Lett.*, 120:183602, May 2018.
- [101] I-Chung Wang Shengwang Du Yong-Fan Chen Ying-Cheng Chen Yi-Hsin Chen, Meng-Jung Lee and Ite A. Yu. Coherent optical memory with high storage efficiency and large fractional delay. 2012.
- [102] Anindya Rastogi, Erhan Saglamyurek, Taras Hrushevskyi, Scott Hubele, and Lindsay J. LeBlanc. Discerning quantum memories based on electromagnetically-induced-transparency and autler-townes-splitting protocols. *Phys. Rev. A*, 100:012314, Jul 2019.
- [103] Christian Hubrich Georg Heinze and Thomas Halfmann. Stopped light and image storage by electromagnetically induced transparency up to the regime of one minute. 2013.
- [104] Sheng Zhang, Jixuan Shi, Zhaibin Cui, Ye Wang, Yukai Wu, Luming Duan, and Yunfei Pu. Realization of a programmable multipurpose photonic quantum memory with over-thousand qubit manipulations. *Physical Review X*, 14(2), April 2024.
- [105] S. H. Autler and C. H. Townes. Stark effect in rapidly varying fields. *Phys. Rev.*, 100:703–722, Oct 1955.
- [106] Logan Cooke Anindya Rastogi Lindsay J. LeBlanc Erhan Saglamyurek, Taras Hrushevskyi. Single-photon-level light storage in cold atoms using the autler-townes splitting protocol. 2019.
- [107] Anindya Rastogi, Erhan Saglamyurek, Taras Hrushevskyi, Scott Hubele, and Lindsay J. LeBlanc. Discerning quantum memories based on electromagnetically-induced-transparency and autler-townes-splitting protocols. *Phys. Rev. A*, 100:012314, Jul 2019.
- [108] Peiyu Yang Zhifei Yu L. Q. Chen Chun-Hua Yuan Weiping Zhang Jinxian Guo, Xiaotian Feng. High-performance raman quantum memory with optimal control in room temperature atoms. *Nature Communications* 10, 148, 2019.
- [109] Ran Finkelstein, Eilon Poem, Ohad Michel, Ohr Lahad, and Ofer Firstenberg. Fast, noise-free memory for photon synchronization at room temperature. *Science Advances*, 4(1), January 2018.
- [110] Nicolas Sangouard, Christoph Simon, Mikael Afzelius, and Nicolas Gisin. Analysis of a quantum memory for photons based on controlled reversible inhomogeneous broadening. *Phys. Rev. A*, 75:032327, Mar 2007.

- [111] S. A. Moiseev and S. Kröll. Complete reconstruction of the quantum state of a single-photon wave packet absorbed by a doppler-broadened transition. *Phys. Rev. Lett.*, 87:173601, Oct 2001.
- [112] B M Sparkes, J Bernu, M Hosseini, J Geng, Q Glorieux, P A Altin, P K Lam, N P Robins, and B C Buchler. Gradient echo memory in an ultra-high optical depth cold atomic ensemble. *New Journal of Physics*, 15(8):085027, August 2013.
- [113] Antonio Ortu, Jelena V Rakonjac, Adrian Holzäpfel, Alessandro Seri, Samuele Grandi, Margherita Mazzera, Hugues de Riedmatten, and Mikael Afzelius. Multimode capacity of atomic-frequency comb quantum memories. *Quantum Science and Technology*, 7(3):035024, June 2022.
- [114] Alessandro Seri, Dario Lago-Rivera, Andreas Lenhard, Giacomo Corrielli, Roberto Osellame, Margherita Mazzera, and Hugues de Riedmatten. Quantum storage of frequency-multiplexed heralded single photons. *Phys. Rev. Lett.*, 123:080502, Aug 2019.
- [115] Rong Wang Dun-Mao Du Xiao-Jun Zhang Zhi-Hui Kang Yun Jiang Jin-Hui Wu Hai-Hua Wang, Yun-Fei Fan and Jin-Yue Gao. Three-channel all-optical routing in a pr3+:y2sio5 crystal. *Opt. Express*, 17:12197–12202, 2009.
- [116] ThorLabs. Vapor reference cells, 2024.

  https://www.thorlabs.com/NewGroupPage9\_PF.cfm?ObjectGroup\_ID=1470
  [Accessed: 12/12/2024].
- [117] Krzysztof T Kaczmarek1 Alexey Tiranov1-Nicolas Gisin1 Adrian Holzäpfel1, Jean Etesse1 and Mikael Afzelius. Optical storage for 0.53 s in a solid-state atomic frequency comb memory using dynamical decoupling. *New J. Phys.*, 22(063009), June 2020.
- [118] Abbes Amira Ruba Kharsa, Ahmed Bouridane. Advances in quantum machine learning and deep learning for image classification: A survey. *Science Direct*, 560, 2023.
- [119] Alessandro Seri, Andreas Lenhard, Daniel Rieländer, Mustafa Gündoğan, Patrick M. Ledingham, Margherita Mazzera, and Hugues de Riedmatten. Quantum correlations between single telecom photons and a multimode on-demand solid-state quantum memory. *Physical Review X*, 7(2), May 2017.
- [120] A. Ishizawa H. Omi T. Inaba X. Xu-R. Kaji S. Adachi S. Yasui, M. Hiraishi and T. Tawara. Creation of a high-resolution atomic frequency comb and optimization of the pulse sequence for high-efficiency quantum memory in 167er:y2sio5. *Opt. Continuum* 1, (1896-1908), 2022.
- [121] H. Ludvigsen and E. Bødtker. New method for self-homodyne laser linewidth measurements with a short delay fiber. *Optics Communications*, 110:595–598, 1994.

- [122] Hugues de Riedmatten, Mikael Afzelius, Matthias U. Staudt, Christoph Simon, and Nicolas Gisin. A solid-state light–matter interface at the single-photon level. *Nature*, 456(7223):773–777, December 2008.
- [123] Sebastian P. Horvath, Mohammed K. Alqedra, Adam Kinos, Andreas Walther, Jan Marcus Dahlström, Stefan Kröll, and Lars Rippe. Noise-free on-demand atomic frequency comb quantum memory. *Phys. Rev. Res.*, 3:023099, May 2021.
- [124] Ioana Craiciu, Mi Lei, Jake Rochman, Jonathan M. Kindem, John G. Bartholomew, Evan Miyazono, Tian Zhong, Neil Sinclair, and Andrei Faraon. Nanophotonic quantum storage at telecommunication wavelength. *Phys. Rev. Appl.*, 12:024062, Aug 2019.
- [125] Zong-Quan Zhou Chuan-Feng Li Guang-Can Guo Yu Ma, You-Zhi Ma. One-hour coherent optical storage in an atomic frequency comb memory. *Nature Communications*, 12(2381), 2021.
- [126] Jelena V. Rakonjac, Dario Lago-Rivera, Alessandro Seri, Margherita Mazzera, Samuele Grandi, and Hugues de Riedmatten. Entanglement between a telecom photon and an on-demand multimode solid-state quantum memory. *Phys. Rev. Lett.*, 127:210502, Nov 2021.
- [127] Jonathan Hänni, Alberto E. Rodríguez-Moldes, Félicien Appas, Soeren Wengerowsky, Dario Lago-Rivera, Markus Teller, Samuele Grandi, and Hugues de Riedmatten. Heralded entanglement of on-demand spin-wave solid-state quantum memories for multiplexed quantum network links, 2025.
- [128] N Timoney-C Laplane N Gisin P Jobez, I Usmani and M Afzelius. Cavity-enhanced storage in an optical spin-wave memory. *New J. Phys*, 16, 2014.
- [129] Stefano Duranti, Sören Wengerowsky, Leo Feldmann, Alessandro Seri, Bernardo Casabone, and Hugues de Riedmatten. Efficient cavity-assisted storage of photonic qubits in a solid-state quantum memory. *Optics Express*, 32(15):26884, July 2024.
- [130] Antonio Ortu, Adrian Holzäpfel, Jean Etesse, and Mikael Afzelius. Storage of photonic time-bin qubits for up to 20ms in a rare-earth doped crystal. *npj Quantum Information*, 8(1), March 2022.
- [131] Neil Sinclair, Erhan Saglamyurek, Hassan Mallahzadeh, Joshua A. Slater, Mathew George, Raimund Ricken, Morgan P. Hedges, Daniel Oblak, Christoph Simon, Wolfgang Sohler, and Wolfgang Tittel. Spectral multiplexing for scalable quantum photonics using an atomic frequency comb quantum memory and feed-forward control. *Physical Review Letters*, 113(5), July 2014.
- [132] G. P. Teja, Christoph Simon, and Sandeep K. Goyal. Photonic quantum memory using an intra-atomic frequency comb. *Phys. Rev. A*, 99:052314, May 2019.

- [133] Jing B. Zhang XY. et al. Wei, SH. Quantum storage of 1650 modes of single photons at telecom wavelength. *npj Quantum Inf*, 10:19, 2024.
- [134] D. Main, T. M. Hird, S. Gao, I. A. Walmsley, and P. M. Ledingham. Room temperature atomic frequency comb storage for light. *Optics Letters*, 46(12):2960, June 2021.
- [135] Rubidium. https://en.wikipedia.org/wiki/Rubidium.
- [136] Junying Zhang Lijiang Zhao Jiancheng Fang aotian Chi, Wei Quan. Advances in anti-relaxation coatings of alkali-metal vapor cell. *Applied Surface Science*, 501, 2020.
- [137] Frédéric Moynier Emily A. Pringle. Rubidium isotopic composition of the earth, meteorites, and the moon: Evidence for the origin of volatile loss during planetary accretion. *Earth and Planetary Science Letters*, 473:62–70, 2017.
- [138] Harry Levine, Alexander Keesling, Giulia Semeghini, Ahmed Omran, Tout T. Wang, Sepehr Ebadi, Hannes Bernien, Markus Greiner, Vladan Vuletić, Hannes Pichler, and Mikhail D. Lukin. Parallel implementation of high-fidelity multiqubit gates with neutral atoms. *Phys. Rev. Lett.*, 123:170503, Oct 2019.
- [139] Grégoire Pichard, Desiree Lim, Étienne Bloch, Julien Vaneecloo, Lilian Bourachot, Gert-Jan Both, Guillaume Mériaux, Sylvain Dutartre, Richard Hostein, Julien Paris, Bruno Ximenez, Adrien Signoles, Antoine Browaeys, Thierry Lahaye, and Davide Dreon. Rearrangement of individual atoms in a 2000-site optical-tweezer array at cryogenic temperatures. *Physical Review Applied*, 22(2), August 2024.
- [140] Kyle W. Martin, Gretchen Phelps, Nathan D. Lemke, Matthew S. Bigelow, Benjamin Stuhl, Michael Wojcik, Michael Holt, Ian Coddington, Michael W. Bishop, and John H. Burke. Compact optical atomic clock based on a two-photon transition in rubidium. *Phys. Rev. Appl.*, 9:014019, Jan 2018.
- [141] Daniel M. Farkas, Evan A. Salim, and Jaime Ramirez-Serrano. Production of rubidium bose-einstein condensates at a 1 hz rate, 2014.
- [142] Daniel A. Steck. Rubidium 87 d line data. Physics, Materials Science, 2008.
- [143] Junmin Wang Baodong Yang, Yi Liu. Double resonance optical pumping-polarization spectroscopy of an excited state transition. *Optics Communications*, 474:126102, 2020.
- [144] ThorLabs. Single mode fc/apc fiber optic patch cables, 2024. https://www.thorlabs.com/newgrouppage9.cfm?objectgroup\_id=334&pn=P3-780A-FC-1 [Accessed: 22/10/2024].
- [145] Daniel A. Steck. Rubidium 85 d line data. Physics, Materials Science, 2003.
- [146] Torrey Glenn. CHEMISTRY 101A GENERAL COLLEGE CHEMISTRY. LibreTexts, 2024.
- [147] L. Allen and J. H. Eberly. *Optical Resonance and Two-Level Atoms*. Dover Publications, New York, 1975.

- [148] Robert C. Hilborn. Einstein coefficients, cross sections, f values, dipole moments, and all that, 2002.
- [149] D. Main, T. M. Hird, S. Gao, E. Oguz, D. J. Saunders, I. A. Walmsley, and P. M. Ledingham. Preparing narrow velocity distributions for quantum memories in room-temperature alkali-metal vapors. *Physical Review A*, 103(4):043105, April 2021.
- [150] D. M. Homan, W. G. Graham, R. E. Continetti, and T. P. Softley. A simplified calculation of power-broadened linewidths, with application to resonance ionization mass spectrometry. *Spectrochimica Acta Part B: Atomic Spectroscopy*, 48(9):1227–1239, 1993.
- [151] Guglielmo Panelli, Shaun C. Burd, Erik J. Porter, and Mark Kasevich. Doppler-free three-photon spectroscopy on narrow-line optical transitions, 2024.
- [152] K. T. Kaczmarek, P. M. Ledingham, B. Brecht, S. E. Thomas, G. S. Thekkadath, O. Lazo-Arjona, J. H. D. Munns, E. Poem, A. Feizpour, D. J. Saunders, J. Nunn, and I. A. Walmsley. High-speed noise-free optical quantum memory. *Physical Review A*, 97(4), April 2018.
- [153] Benjamin Maaß, Norman Vincenz Ewald, Avijit Barua, Stephan Reitzenstein, and Janik Wolters. Room-temperature ladder-type optical memory compatible with single photons from semiconductor quantum dots. *Phys. Rev. Appl.*, 22:044050, Oct 2024.
- [154] Mustafa Gündoğan, Patrick M. Ledingham, Kutlu Kutluer, Margherita Mazzera, and Hugues de Riedmatten. Solid state spin-wave quantum memory for time-bin qubits. *Phys. Rev. Lett.*, 114:230501, Jun 2015.
- [155] S. E. Thomas, L. Wagner, R. Joos, R. Sittig, C. Nawrath, P. Burdekin, T. Huber-Loyola, S. Sagona-Stophel, S. Höfling, M. Jetter, P. Michler, I. A. Walmsley, S. L. Portalupi, and P. M. Ledingham. Deterministic storage and retrieval of telecom quantum dot photons interfaced with an atomic quantum memory, 2023.
- [156] Martin B Nicolle. Engineering quantum light-matter interactions in solid-state platforms.
- [157] David Halliday, Robert Resnick, and Jearl Walker. *Fundamentals of Physics*. Wiley, Hoboken, NJ, 10th edition, 2013. Electric Current and Direct-Current Circuits.
- [158] Amnon Yariv and Pochi Yeh. *Photonics: Optical Electronics in Modern Communications*. Oxford University Press, 6th edition, 2006.
- [159] Jean Etesse Mikael Afzelius Antonio Ortu, Adrian Holzäpfel. Storage of photonic time-bin qubits for up to 20ms in a rare-earth doped crystal. *npj Quantum Information* 8, 29, 2022.

- [160] Mustafa Gündoğan, Patrick M. Ledingham, Attaallah Almasi, Matteo Cristiani, and Hugues de Riedmatten. Quantum storage of a photonic polarization qubit in a solid. *Physical Review Letters*, 108(19), May 2012.
- [161] Excelitas. Single Photon Counting Module 4 Channel Array. SPCM-AQ4C Rev. 2020-04.
- [162] Christopher J. Foot. Atomic physics. *Oxford University Press*, 2005. ISBN: 978-0198509246.